Development of active silicon nitride nanophotonic platform with emerging materials

Yueyang Chen

A dissertation

submitted in partial fulfillment of the

requirements for the degree of

Doctor of Philosophy

University of Washington

2021

Reading Committee:

Arka Majumdar, Chair

Karl F. Böhringer

Mo Li

Program Authorized to Offer Degree:

Electrical Engineering

University of Washington

Abstract

Development of active silicon nitride nanophotonic platform with emerging materials

Yueyang Chen

Chair of the Supervisory Committee:
Arka Majumdar
Department of Electrical and Computer Engineering

The field of integrated photonics has grown rapidly in the past few decades, with numerous applications in data communication, quantum technology and biomedical sensing. Among various emerging platforms for photonic integration, silicon nitride (SiN) has recently become an excellent candidate thanks to its low optical loss over a broad transparent window, together with the CMOS compatibility. However, most SiN photonic components demonstrated so far are passive devices for guiding photons. Further development of active components, including photon sources and nonlinear photonics components, is required for both classical and quantum applications.

One promising direction is to heterogeneously integrate novel optoelectronics materials onto the SiN platform. In this thesis, I present my work on the hybrid SiN photonics platform with two emerging materials: solution-processed colloidal quantum dots (QDs) and transition metal dichalcogenides (TMD) monolayer. I focus on the fundamental study of light-matter interaction

between these quantum-confined materials with the integrated SiN photonic cavities. For colloidal QDs, I demonstrate deterministic positioning of these emitters on SiN photonic crystal nanobeam cavity and observe the Purcell enhancement and saturable photoluminescence. For monolayer TMD, I demonstrate the strong coupling between the two-dimensional excitons with a SiN metasurface. Apart from the light-matter interaction, I also explore tunable SiN integrated cavities and demonstrate the large thermal tuning of a polymer embedded SiN nanobeam cavity, together with the active tuning of a heterogenous photonic molecule. The work presented paves the way for future development of cavity-enhanced light sources, ultra-low-power optical switch, and quantum photonic simulators on the SiN platform.

TABLE OF CONTENTS

LIST OF FIGURES

LIST OF TABLES

ACKNOWLEDGEMENTS

I would like to express my gratitude to my advisor Prof. Arka Majumdar, who is a genuine mentor and passionate scientist. I am so grateful for his guidance and support over the past five years. In my first couple years, he knew about every detail of my projects and always offered hands-on guidance whenever I was stuck. Later, he gave me the chance to pursue some of my own ideas, and both two phases combined make my five years fun and productive. Arka also encouraged me to present at conferences and take two internship opportunities that are really helpful for my future career. More importantly, besides the scientific ideas that I learned from him, I am deeply inspired by his confident and optimistic attitude towards research and everyday life, which I believe would have a continuous influence on me even after graduate school.

I would like also to thank the faculties and staff members who helped me along the way. I would like to thank my thesis committee: Prof. Karl Böhringer, Prof. Mo Li and Prof. Fu Dan. I am very grateful for all your time and advice. I would like to thank Prof. M.P. Anantram and Profs. Lih Lin for their classes on devices and photonics, from which I learned useful knowledge for my research projects. I would also like to thank all the staff members in the Washington Nanofabrication Facility for their support on the device fabrication for my projects.

The Nano Optoelectronic Integrated System Engineering (NOISE) lab has been a great part of my life during the past five years. Dr. Taylor Fryett is the first PhD student in our lab, who taught me everything about the experiments. Thank you for setting up a great role model, and just by shadowing your experiments, I learned how to work smartly along with the persistence. I worked closely with Dr. Albert Ryou, our brilliant post-doc, for my first paper. Thank you for teaching me

optics, and I learned scientific thinking by working with you side-by-side. I would like to thank James Whitehead for helping me a ton with fabrication, coding, and also getting my first car in summer 2018! I would like to thank Abhi Saxena's constant explanations of various quantum optics concepts, and we had great fun working together in lab and office. Though I haven't worked closely with Dr. Alan Zhan and Dr. Shane Colburn on any specific projects, I could always get valuable advice from you regarding research and life. I enjoyed the chats with Alan on research and basketball: it would be cool if Seattle hosts an NBA team again in the near future! I would also thank Shane for his patient answers to all the topics that I consulted him about. All of your advice indeed help me handle the situations. In my final year, I got the chance to work with David Sharp, Chris Munley and Arnab Manna, and wish you all the best on your PhD journey. I also enjoyed a lot from the chats with Dr. Jiajiu Zheng and Elyas Bayati on the topics regarding graduation and job searching. I shared the office with David Rosser, from whom I always learned new perspectives on various topics. I also enjoyed the chats with Roger Fang, Luocheng Huang, Maksym Zhelyeznyakov, Zheyi Han, Rui Chen and Dr. Quentin Tanguy. I had a great time with our visiting scholars: Dr. Peipeng Xu, Dr. Vishal Vashishtha, and Dr. Yun Gao. I'd also like to thank Dr. Shreyas Shah and Dr. Chang-Hua Liu, previous postdocs in the NOISE lab, for their suggestions on my research and career. I would like to thank Chuchuan Hong and Dan Guo for their accompany on the basketball court and movie theaters in my first two years. At that time I also got the chance to work with three very talented undergraduate students: Zane Matthew Peycke, Jiaming Li and Jacob Waelder. Wish you all the best in your future career!

I would also like to thank my collaborators. Prof. Mo Li's group moved to UW in my third year and I had a great connection with every group member. I would like to thank Bingzhao Li for the great time we spent in gym and basketball court, and also for the mutual encouragement during

our PhD journey. Wish your dream comes true soon! I also enjoyed a lot from the discussion with Ruoming Peng, Changming Wu, Seokhyeong Lee, Dr. Che Chen, Dr. Qiyu Liu, Dr. Huan Li and Dr. Zhao Han. I would like to also thank my collaborators on multiple projects: Dr. Max Friedfeld, Dr. Michael Enright, Florence Dou, Yunping Huang and Prof. Brandi Cossairt for the colloidal quantum dot project; Kevin Smith and Prof. David Masiello for the coupled cavities project; Shengnan Miao, Dr. Tianmeng Wang, Prof. Sufei Shi, Dr. Ding Zhong, Dr. Colin Chow and Prof. Xiaodong Xu for the exciton-polariton project; Dr. Chen Zou, Prof. Lih Lin, Theodore Cohen, Prof. Daniel Gamelin, Erin Jedlicka, Dr. Jian Wang and Prof. David Ginger for the perovskite project; Dr. Anupam Pant and Prof. Peter Pauzauskie for the laser refrigeration project. Thank you all my collaborators! Working with you taught me numerous new lessons, spanning from advanced chemical synthesis to theoretical physics.

I would also like to thank all the friends who supported me in the past five years. I would like to express my special thanks to Yefu Chen, Fan Yang and Jinbo Pan for the great time we had together, starting from that hiking at Lake 22 trail in summer 2017. I wish Yefu all the best in his quest towards his PhD degree at University of Texas, Austin, and all the best to Fan and Jinbo in their professional careers! I would also like to thank Jiyue Zheng, Sikai Liu and Xiaohong Zhang for their constant encouragement during my PhD. Finally, I would like to thank Yutong Xie, for her support and accompany in the past eight years. I am so blessed to have you in my life. Last but not least, I would like to thank my parents for their support along the way.

DEDICATION

To my parents and Yutong

Chapter 1 Introduction

1.1 Overview

Photonic integrated circuits (PIC), taking advantage of their compact size and scalable fabrication technology, have recently seen an outpouring of diverse applications, ranging from optical communication, quantum information science, and optical sensing [1–3]. Among the emerging platforms for integrated photonics, silicon nitride has recently attracted strong attention [4–6]. Silicon nitride (SiN), a CMOS compatible material, is optically transparent over a broad frequency window, spanning from the visible to the mid-infrared wavelength range. Recently, the booming AR/VR and optical sensing industry also creates a large demand for compact optical devices working at the visible wavelength range, where SiN photonics provides a promising candidate. Large-scale phased arrays and on-chip spectrometers at visible wavelength range have already been demonstrated on the SiN platform [7,8]. Besides the broad transparent window, SiN has a moderate refractive index (n = 2), resulting in a higher fabrication tolerance and lower waveguide scattering loss compared to other high index PIC platforms (Silicon, or InP). SiN waveguides with ultra-low loss of 0.2dB/cm and ring resonators with quality factor up to millions have been demonstrated [4,6]. Last but not least, the absence of two-photon absorption and free-carrier absorption make SiN photonics an ideal platform to handle high laser power [7].

In spite of the above-mentioned advantages of SiN photonics, most SiN PICs demonstrated so far are passive devices. Further integration with active components (lasers/ modulators/ detectors) is required to extend the functionality of the platform. However, the development of active SiN devices remains challenging. For example, the light source on SiN platform is a critical component for both classical and quantum applications, because SiN is an inefficient light-emitting material.

Another critical active component is the low-power phase modulator, which is required for reconfigurable switching networks [9] and on-chip dynamic phased-array [10]. Unfortunately, efficient tuning of SiN devices remains difficult: as a centrosymmetric material with a large bandgap, SiN has a low thermo-optic coefficient ($\Delta n \sim 10^{-5}/°C$) and lacks both free-carrier dispersion and second-order nonlinearity.

To address the above issues, hybrid integration of new materials with active properties is desirable for SiN photonics. Efforts have been devoted to the development of hybrid silicon nitride lasers and modulators via wafer-bonding or transfer printing techniques. For example, Park et. al demonstrated heterogeneous integration of III-V lasers on SiN platform [11]. Churaev et al. wafer bonded Lithium niobate with SiN for high-speed modulation [12]. Such an approach is indeed promising and has sparked industrial start-ups such as Nexus Photonics. The drawbacks of the wafer-bonding process are, however, its high cost and stringent fabrication requirement for both the SiN and the heterogeneous material.

Alternatively, some recent emerging materials, for example, solution-processed materials [13] and two-dimensional materials [14] show promising optoelectronic properties. Compared to traditional III-V semiconductors, they are much easier to integrate with the SiN platform. Solution-processed materials, including colloidal quantum dots (QDs) and nanoplatelets (NPLs), are efficient light emitters supporting a broad and tailorable spectral range. They are widely applied in today's display industry. In the meantime, ongoing research continues to improve the chemical synthesis of colloidal materials with ultra-high purity as well as complex heterostructures with engineered quantum confinement of electrons and holes. Moreover, solution processed materials can be easily integrated with any substrate via spin-coating, making them an excellent candidate for integrating with on-chip photonic devices. Two-dimensional (2D) materials also recently emerged as

promising optoelectronic materials. These materials possess different band gaps leading to the ability to emit/modulate/detect photons over a wide range of wavelengths. Among various novel 2D materials, transition metal dichalcogenides (TMD) are particularly promising. Studies found that when exfoliated down to a single layer thickness, the TMD band-structure transits from indirect to direct bandgap [15]. As a result, the monolayer becomes a light-emitting material. Various light sources based on monolayer TMD have been demonstrated, including LED [16], laser [15] and single-photon source [18]. TMDs can also host excitons with large binding energies at room temperature [34].

Previous studies have shown the promise of integrating both the solution-processed material and TMD monolayer with SiN photonics [17,19]. Since these material systems are still at the early-stage of integrated with SiN photonics, one fundamental research direction is to understand the light-matter interaction between the material and integrated photonics platform. One of the key achievements during the past decade in integrated photonics has been the success of the improved design and fabrication of optical resonators [20]. Photons could be stored inside these resonators for a long lifetime and with strong spatial confinement, leading to enhanced light-matter coupling. Ultra-low threshold laser [21], high-efficient modulator [22], and single-photon nonlinear switches [23] have been demonstrated by enhancing the light-matter interaction inside integrated cavities. In this thesis, we focus on coupling the solution-processed material and monolayer TMD to integrated SiN photonic cavities. The main idea is to understand the light-matter coupling of these novel materials and explore both the weak and strong coupling regimes [20]. We study two distinct types of nano-resonators: (i) low-mode volume resonators with three-dimensional confinement of light, and (ii) resonators supporting delocalized resonant modes with light tightly confined in only one dimension. An example of the first type, also called zero-dimensional (0D)

cavities are photonic crystal defect mode cavities, such as linear three-hole (L3) defect cavities [23] or nanobeam resonators [24]. The second type, also known as two-dimensional (2D) cavities include distributed Bragg reflector (DBR) cavities [25], or guided mode resonators/ nonlocal metasurfaces [26,27]. 0D cavities can provide ultra-small sub-wavelength mode volume and thus can provide large Purcell enhancement in the weak coupling regime. However, tuning these cavities are difficult, and one needs to resort to gas tuning [28,29], or thermal tuning [30,31]. Both of these mechanisms provide a very limited tuning range. The resonance wavelength of 2D cavities can be easily tuned by collecting light at different angles, due to the dispersive nature of these cavities. Hence, this type of 2D cavity is often preferred to study strong coupling. We believe our fundamental study paves the way for the future development of functional devices, such as nano-laser, quantum light source, and low-power optical switches on the hybrid SiN platform. A brief introduction of the materials and the photonic cavity structures could be found in the following sections.

1.2 Colloidal Quantum Dots

Colloidal quantum dots are semiconductor nanocrystals with diameters of <10nm, the quantum confinement results in discrete energy states (Figure 1.1). Owing to their robust synthesis and straightforward deposition to most substrates, colloidal QDs have generated intense interest as a novel class of light-emitting materials, of which the emission wavelength is tunable based on the size of the quantum dot. Typically, the colloidal QDs are synthesized with a core-shell structure to stabilize their dispersion in solvents. Colloidal synthesis can produce ultra-high purity nanocrystalline materials, i.e., materials with an extremely low background of unintentional dopants, as compared to epitaxial grow, as well as complex heterostructures with engineered quantum confinement of electrons and holes. All these together results in high quantum efficiency

and bright emission. Commercial LED devices based on colloidal QDs have been widely applied in the display industry. Recently, colloidal QDs also attracts interest for applications such as lasing and single-photon source. For the lasing application, colloidal QDs offer benefits including low optical-gain threshold and high-temperature stability. Furthermore, by coupling the colloidal QDs to an integrated nanophotonic cavity, the spontaneous emission coupling factor, also known as the β factor could be enhanced via the Purcell effect, resulting in a reduction of the lasing threshold. The β factor is defined as

$$\beta = \frac{\Gamma_{cav}}{\Gamma_{cav} + \Gamma_{other} + \Gamma_{nr}}, \quad (1.1)$$

Here, Γ_{cav} is the radiative decay rate into the cavity mode, Γ_{other} is the decay rate into other optical modes, and Γ_{nr} is the nonradiative decay rate. Purcell enhancement could increase Γ_{cav}, resulting in a higher β factor. With more radiative coupling channeled into the laser modes, the lasing threshold would subsequently be reduced.

For the quantum light-source application, single-photon emission has been measured from a single colloidal quantum dot. An electrically triggered single-photon source has also been demonstrated [24]. The current challenge lies in the poor single-photon indistinguishability of the challenges for colloidal quantum dots. Colloidal QDs typically suffer from huge dephasing rates ($\gamma^* \approx 10^5\gamma$, γ^* being the pure dephasing rate and γ being the QD dipole decay rate) at room temperature, which makes the emitted single photons highly distinguishable. Exciton-phonon interactions in these dots cause randomization of the phase of wavefunctions, which results in loss of quantum coherence and leads to dephasing [23]. Apart from this, charge noise arising from fluctuations in the environment leads to small DC shifts in the emitter transition energy contributing to further decoherence [26]. With both effects combined, the indistinguishability of

colloidal QDs is limited. For typical quantum emitters with a large dephasing rate, the indistinguishability I of emitted photons is given by [27]

$$I = \frac{\gamma}{\gamma+\gamma^*}, \quad (1.2)$$

where γ is the radiative decay rate and γ^* is the pure dephasing rate of the quantum emitter. Hence for colloidal QDs, where $\gamma^* \approx 10^5\gamma$ the indistinguishability I turns out to be $\sim 10^{-5}$, making it impossible to use the bare emitter as a useful indistinguishable single-photon source.

Further improvement of indistinguishability of emitted single photons is expected from progress in synthesis techniques and new materials like perovskite QDs. Recently, perovskite QDs with optical coherence times (T_2) of up to 80 ps were demonstrated [28]. With their radiative lifetime (T_1) being 210 ps, the bare emitter indistinguishability I from these perovskite QDs approaches $I \sim \frac{T_2}{2T_1} \approx 0.19$. This signifies two to three orders of magnitude improvements over the standard colloidal QDs, which fundamentally suffer from slow photon release from dark exciton states. These results pave the way for the future development of indistinguishable solution-processed quantum emitters that have fast emission, wide spectral tunability, and scalable production.

Besides the progress in material synthesis, to develop a bright single-photon source with high indistinguishability, integration with nanophotonic cavities becomes indispensable. Coupling a single-photon emitter with a high-quality factor and small mode volume photonic cavity could enhance the spontaneous emission rate via Purcell enhancement [29]. The enhanced spontaneous emission rate would then lead to brighter emission and higher indistinguishability (larger than $\frac{T_2}{2T_1}$).

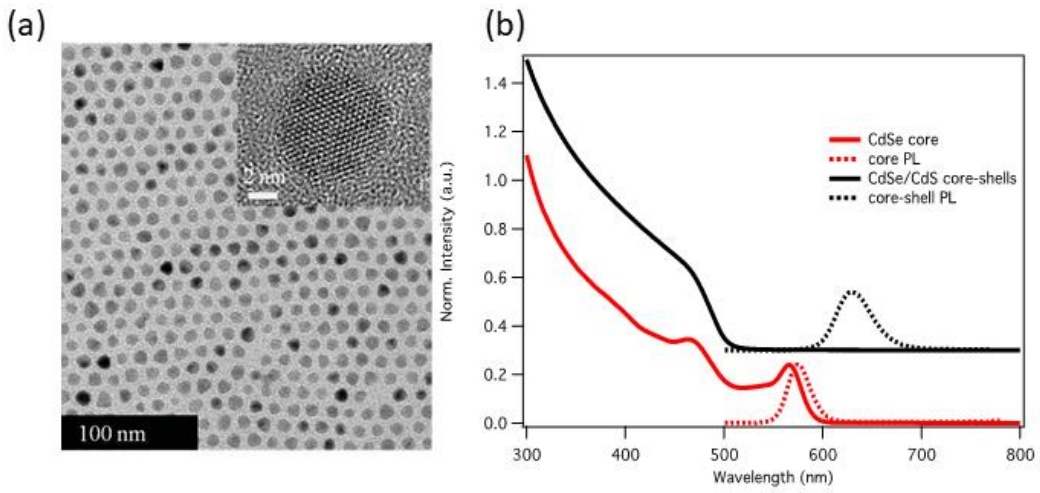

Figure 1.1. Colloidal QDs. (a) TEM image of colloidal quantum dot [30]. (b) PL and absorption spectrum of CdSe/CdS core-shell QDs [31]. Figure a reprinted with permission from Ref. [30]. Copyright (2015) John Wiley and Sons. Figure b reprinted with permission from Ref. [31]. Copyright (2018) American Chemical Society.

1.3 TMD monolayer

Monolayer transition-metal dichalcogenides (TMDs) have generated active research interest in recent years due to their strong light−matter interaction and unique optoelectronic properties. Thanks to the quantum confinement and reduced dielectric screening in the atomic layer, excitons with large binding energy can form in monolayer TMD at room temperature, exhibiting strong excitonic absorption and photoluminescence (Figure 1.2). The strong excitonic response could be further enhanced by coupling the TMD monolayer to an optical cavity. In the weak coupling regime, low-threshold nano-lasers and cavity-enhanced light-emitting diodes have been demonstrated using the TMD monolayer [17,32]. In the strong coupling regime, TMD exciton−polaritons (EPs) have also been observed at room temperature [33]. Exciton-polaritons, the hybrid light−matter quasi-particles, inherit the low effective mass from their photonic

component and large nonlinear interaction strength from their excitonic component, making them a promising platform to study Bose−Einstein condensate, with a far-reaching impact on quantum simulation with interacting photons.

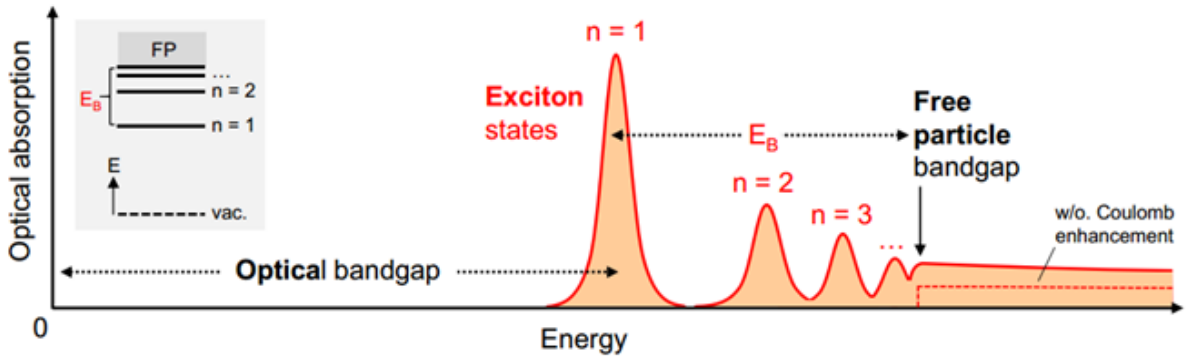

Figure 1.2. Excitonic absorption of TMD monolayer [34]. Reprinted with permission from Ref. [34]. Copyright (2018). American Physical Society.

1.4 Photonic crystal nanobeam cavity

We focus on the photonic crystal (PhC) nanobeam cavity in this thesis. PhC nanobeam cavities [35] have recently emerged as a powerful alternative to slab-based L3 PhC cavities [17]. Compared to L3 PhC cavity, nanobeam provides better coupling with the waveguide structure, together with a smaller footprint. Moreover, it is difficult to open up a complete bandgap in two-dimension in a SiN slab due to the moderate refractive index, thus L3 cavity on SiN tends to have a lower quality factor compared to the nanobeam cavity. The structure of the nanobeam is shown in Figure 3. In the x-direction, periodic-pattern holes function as mirrors to form a cavity in the middle. In the y and z direction, total internal reflection confined the photons in small mode volume. To achieve a high-quality factor, the period of the holes is tapered from the mirror section to the center. We designed the parameter as follows for the cavity at 630nm: we assigned 10 elliptical holes for the

tapering region and optimized the design parameters until we found a suitably high Q-factor (Q ~ 10^5) resonance centered at 630 nm. In the final design, the nanobeam has a thickness t = 220 nm and a width w = 553 nm. The Bragg region consists of 40 elliptical holes placed at a periodicity of a = 189 nm. The elliptical holes have a major and a minor diameter of 242 nm and 99 nm, respectively. In the tapering region, the periodicity and the major diameter of the hole is linearly reduced to 179 nm and 112 nm, while the minor diameter is fixed. The cavity length is 72 nm. The resulting electromagnetic field has a mode volume of ~2.5 $\left(\frac{\lambda}{n}\right)^3$.

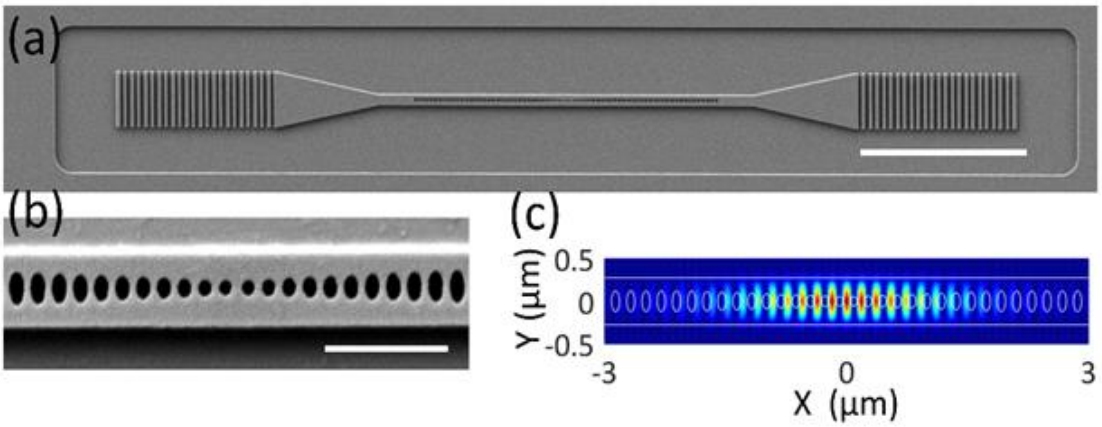

Figure 1.3. Photonic crystal nanobeam cavity. (a) SEM of the silicon nitride cavity, where the nanobeam is unsuspended and sitting on the silicon oxide [31]; scale bar: 10 μm. (b) Zoom-in on the cavity region; scale-bar: 1 μm. (c) Simulated cavity mode profile via FDTD [31]. Figure reprinted with permission from Ref. [31]. Copyright (2018) American Chemical Society.

1.5 Guided-mode resonance

Besides the nanobeam cavity, we also investigated the guided-mode resonance (GMR) in this thesis. The GMR is first studied by Fan et al. in 2D PhC structures [36]. Such periodic 2D photonic lattice supports many optical Bloch modes propagating inside the slab. These modes can be

classified into two classes, namely, in-plane guided modes and guided-mode resonance (GMR). The GMRs couple with the radiation continuum and, in the meantime, confine part of their electromagnetic energy inside the slab. When a light beam shines on the photonic lattice, the interference between the slab mode and the GMR modes results in a Fano line shape in the reflection spectrum. These Fano resonances have various angle-dependent dispersive spectra, which favor the study of the strong light-matter hybridization and potential polariton dispersion engineering. In our design, the 2D square lattice, also called a non-local metasurface, has a period of 459nm and a hole diameter of 120nm (Figure 1.4a). The metasurface has a thickness of 130nm and it sits on a 1 μm thermal oxide layer grown on 500 μm silicon substrate. Figure 1.4b shows the angle-dependent reflection spectrum along the k_x direction for p-polarized incident light. There are two different GMRs in the spectrum (M1 and M2). One has a linear dispersion (M1) and starts at higher energy and rapidly goes to lower energy when it comes to higher momentum. The other has a parabolic shape (M2): the mode starts at lower energy and goes to higher energy. The two modes come close to each other at $k_x = 0.6\ \mu m^{-1}$, and an anti-crossing behavior appears due to the coupling between two photonic modes.

We would like to point out that our metasurface structure, indeed, is a cavity that stores photons and achieves field enhancement inside the slab in the vertical direction, although it does not have confinement along the in-plane directions. Figure 1.4b is the Rigorous Coupled Wave analysis (RCWA) simulation result of the electrical field distribution of a single metasurface unit cell under a perpendicularly injected light beam. Note that the amplitude of the source is set to be unity. From the color bar, it is clear that there is an amplitude enhancement of the optical field inside the slab.

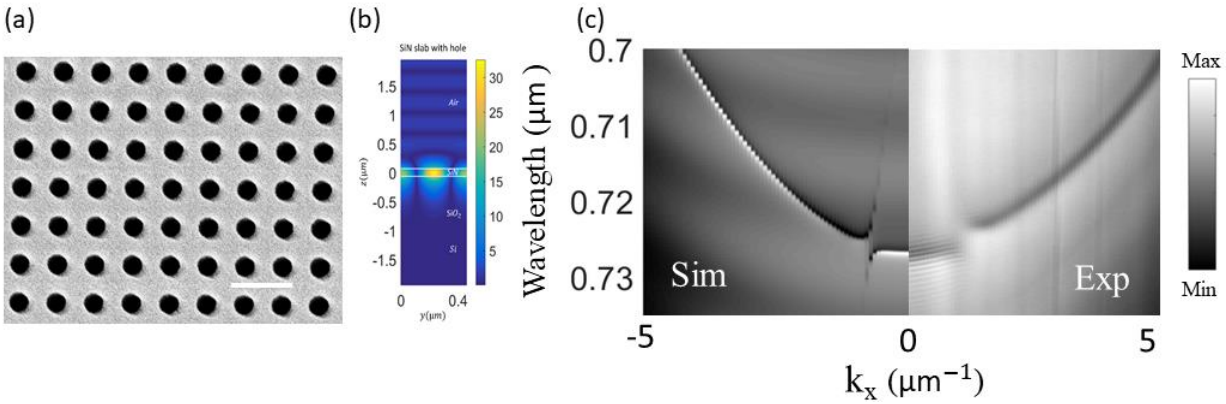

Figure 1.4. Guided-mode resonance. (a) SEM of the SiN metasurface [37]. (b) Simulated cavity mode profile in the vertical direction [37] (c) Simulated vs Experimental results [37]. Figure reprinted with permission from Ref. [37]. Copyright (2020) American Chemical Society.

1.6 Thesis Outline

In Chapter 2, we study the light-matter interaction of solution-processed material on silicon nitride nanophotonic devices. One outstanding challenge of coupling the colloidal QDs with nanophotonic cavity is the random positioning nature of the nanoparticles. To address this issue, we developed a deterministic positioning mechanism: by lithographically defining a window on top of an encapsulated cavity that is covered with a polymer resist, and spin coating the QD solution, we can precisely control the placement of the QDs, which subsequently couple to the cavity. We show rudimentary control of the number of QDs coupled to the cavity by modifying the size of the window. Furthermore, we demonstrate Purcell enhancement and saturable photoluminescence in this QD-cavity platform. We then deterministically position QDs on a photonic molecule and observe QD-coupled cavity super-modes. Furthermore, we extend the platform to the perovskite QD platform for its superior optoelectronic properties. Our results pave the way for precisely controlling the number of QDs coupled to a cavity by engineering the window

size, the QD dimension, and the solution chemistry and will allow advanced studies in cavity-enhanced single-photon emission, ultralow-power nonlinear optics, and quantum many-body simulations with interacting photons.

Apart from the deterministic positioning mechanism, the tunability of photonic crystal cavity is also required for a scalable QD-cavity platform. In Chapter 3, we experimentally demonstrate a polymer-embedded thermally tunable silicon nitride nanobeam cavity with a tuning efficiency of 44 pm/°C and 0.13nm/mW in the visible wavelength range. The large tuning efficiency comes from the high thermal-optics coefficient of the su8 polymer and our 'air-mode' cavity design, where a large portion of cavity field is distributed inside the polymer region. Furthermore, we demonstrate the design, fabrication, and analysis of a tunable heterogeneous photonic molecule consisting of a ring resonator strongly coupled to a nanobeam photonic crystal cavity. Leveraging the disparity in mode volume between these two strongly coupled cavities, we combine theory and experiment to establish the ability to actively tune the mode volume of the resulting supermodes over a full order of magnitude. As the mode volume determines the strength of light-matter interactions, this work illustrates the potential for strongly coupled cavities with dissimilar mode volumes in applications requiring designer photonic properties and tunable light-matter coupling, such as photonics-based quantum simulation.

In Chapter 4, we study the light-matter interaction of monolayer TMDC monolayer on SiN nanophotonic platform. We demonstrate a 2D exciton-polariton system by strongly coupling atomically thin tungsten diselenide (WSe_2) monolayer to a silicon nitride (SiN) metasurface. Via energy-momentum spectroscopy of the WSe_2-metasurface system, we observe the characteristic anti-crossing of the polariton dispersion both in the reflection and photoluminescence spectrum. A Rabi splitting of 18 meV was observed which matched well with our numerical simulation.

Moreover, we show that the Rabi splitting, the polariton dispersion and the far-field emission pattern could be tailored with subwavelength-scale engineering of the optical meta-atoms. Our platform thus opens the door for the future development of novel, exotic exciton-polariton devices by advanced meta-optical engineering.

Chapter 2 Solution-processed material on silicon nitride platform

2.1 Introduction

Hybrid photonic integrated circuits, comprised of nanophotonic structures and active media, have found a wide range of applications from low-power optoelectronic devices [17,38–41] to quantum networks [42,43]. A key driver behind their success has been the improved engineering of the electromagnetic environment with nanoscale optical resonators, which have led to enhanced light-matter coupling and demonstrations of quantum optical effects in both the weak and the strong coupling regimes [42–44]. As a result, it has now become feasible to fabricate a robust array of high quality (Q)-factor cavities on the same chip, opening a possible route to building multi-functional optical interconnects [45,46] as well as scalable, on-chip quantum simulators [47,48].

While state-of-the-art fabrication methods can yield hundreds of cavities with sub-wavelength precision, large-scale control over the positioning of multiple active media remains elusive. Extensive work has been carried out with self-assembled semiconductor quantum dots (QDs) to overcome their random positioning and inhomogeneous broadening, including seeding nucleation centers for site-controlled growth [49], but there has been no report of multiple deterministically coupled QD-cavity systems on the same chip. Beyond semiconductor QDs, several studies looked at deterministic creation of nanodots and single emitters using monolayer materials [50–52], albeit with limited success.

A promising candidate for active media in hybrid photonic integrated circuits is solution-processed colloidal quantum dots (QDs) [53]. Owing to their robust synthesis and straightforward application onto most substrates, colloidal QDs have generated intense interest as a novel class of light emitting materials [54–56]. Optically pumped lasers and electrically triggered single photon

sources based on colloidal QDs have recently been demonstrated [30,57–62]. Low threshold nano-lasers and low power nonlinear optical devices have also been reported by coupling the QDs to nanocavities [38,63–65]. The simple drop-cast and spin-coat methods that were employed to place the QDs on the cavities, however, are probabilistic in nature, where the only control that the experimenter has is the QD density in the solution.

Recently, advanced nano-patterning technology has yielded an innovative solution to deterministic positioning of colloidal QDs [66,67]. The general approach is to lithographically define windows in a resist layer prior to depositing the QDs. During the deposition, depending on the QD size and the chemical properties of the colloidal thin film, the QDs enter and occupy the windows, thus dramatically increasing the selective placement probability. Furthermore, the resist can be removed with a post-deposition lift-off process, taking away the QDs that have been deposited outside the windows. Combining this patterning technique with nanophotonic cavities, however, is challenging. Conventional photonic crystal (PhC) cavities operating in the visible wavelength range are suspended membranes [68,69], which makes them extremely fragile during the patterning process. For instance, during sonication, an important step in the state-of-the-art QD patterning procedure [67], suspended PhC cavities can easily break off. The suspended nature of most PhC cavities working at visible wavelength comes from the limited refractive index of their dielectric material. For example, silicon nitride (SiN), a CMOS compatible material with optical transparency at visible wavelength, has a relatively low refractive index (n~2). As a result, the suspended membrane is deemed necessary since the surrounding air (n~1) provides the largest possible refractive index contrast, a general route to obtain high Q-factor and low volume PhC cavities [69]. A recently demonstrated encapsulated SiN nanobeam cavity, however, offers an alternative and much more robust design [70]. The SiN nanobeam cavity maintains a high Q-factor

and a low mode-volume even when it is sitting on an oxide substrate and cladded with a polymer resist (n~1.45), substantially increasing its mechanical stability under the QD patterning process.

In this chapter, we experimentally demonstrate deterministic positioning of solution-processed colloidal CdSe/CdS QDs on SiN nanobeam cavities. The schematic of the devices is shown in Figure 2.1. The cavities follow the previously reported encapsulated design with elliptical holes [70] and Poly-methyl methacrylate (PMMA) resist cladding. After lithographically opening up fixed-sized windows in the resist, we spin-coat the chip with a uniform film of the colloidal solution, which yields an array of coupled QD-cavities. While the traditional lift-off process could be applied to remove the QDs deposited outside the window, the evanescent coupling nature and the encapsulated cavity design allow one to achieve deterministic positioning simply by making the resist thick enough. For a cavity without a window (Cavity I), we observe no coupling with the QDs, as the thick resist prevents any coupling between the cavity and the QD layer. For cavities with windows (Cavity II and III), we observe coupling with QDs and qualitatively control the coupling by varying the size of the window. We further verify the coupling by observing Purcell enhancement and saturable photoluminescence. We also demonstrate coupling between the QDs and a pair of coupled nanobeam cavities, called a photonic molecule. Finally, we extend this platform to perovskite QDs with novel optoelectronic properties. Our work paves the way to creating a large array of coupled cavities with each cavity containing a specified number of QDs, with potential applications in nonlinear optics, multi-functional optical devices, and on-chip, solid-state quantum simulators.

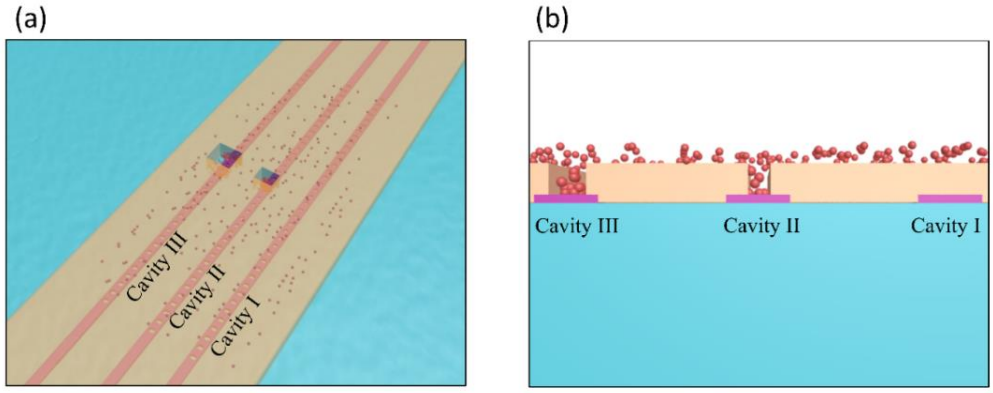

Figure 2.1. Schematics of the deterministic positioning mechanism. (a) Multiple SiN nanobeam cavities (Cavity I, II, III) could be integrated on the same chip. These cavities maintain high-Q operation even under thick organic resist cladding. To deterministically position QDs, we selectively open up windows on certain areas on the chip. This is followed by spin-coating QDs where the QDs fill into the windows to interact with the cavities. For Cavity I, we expect to observe no coupling with the QDs, as the thick resist will prevent any coupling between the cavity and the QD layer. For cavities with windows (Cavity II and III), we expect to observe coupling with QDs and qualitatively control the number of coupled QDs by varying the size of the window. (b) The cross section of the Cavity I, II, and III showing how the QDs enter the windows (Cavity II, III) and couple to the cavity fields.

2.2 Design and fabrication of SiN nanobeam cavity

We first calculated the band structure of the unit cell (using MIT Photonic Bands) and optimized the whole cavity structure with finite difference time domain simulation (Lumerical FDTD Solutions). Specifically, we created the cavity by linearly tapering the major axis diameter of the holes and the period about the cavity center. The simulated Q factor reaches (Q ~10^5) resonance centered at 630 nm. The resulting electromagnetic field has a mode volume of ~2.5 $\left(\frac{\lambda}{n}\right)^3$.

We then fabricated the cavity using 220 nm thick SiN membrane grown via LPCVD on 4 μm of thermal oxide on silicon. The samples were obtained from commercial vendor Rogue Valley Microdevices. We spun roughly 400 nm of Zeon ZEP520A, which was coated with a thin layer of Pt/Au that served as a charging layer. The resist was then patterned using a JEOL JBX6300FX electron-beam lithography system with an accelerating voltage of 100 kV. The pattern was transferred to the SiN using a RIE etch in CHF_3/O_2. Figures 2.2 a, b show the scanning electron micrographs (SEMs) of the fabricated SiN cavities on thermal oxide just after etching. Figure 2.2c shows the simulated profile of the mode confined in the cavity. To encapsulate the cavities, we spun ~ 1 μm PMMA at 3 krpm speed and then baked the chip to remove any remaining solvent.

We then measured the transmission spectra of the cavities using a supercontinuum light source (Fianium WhiteLase Micro). The supercontinuum light was focused on one of the two grating couplers, and the transmitted light collected from the other was analyzed with a spectrometer (Princeton Instruments PIXIS CCD with an IsoPlane SCT-320 Imaging Spectrograph). The grating couplers are designed to provide high efficiency only when they are coated with resist. The use of the grating couplers to measure the cavity transmission and to collect the coupled PL of the QDs in the following experiments is beneficial for on-chip light sources to be integrated with other on-chip photonic components [71]. The cavity transmission spectrum is shown in Figure 2.2d. We observed a cavity resonance at 630 nm with Q-factor ~ 6600, extracted via a Lorentzian fit to the measured data. We note that the experimental Q-factor is significantly smaller than our simulation result, which we attribute to fabrication imperfections due to the small feature size for visible wavelength operation.

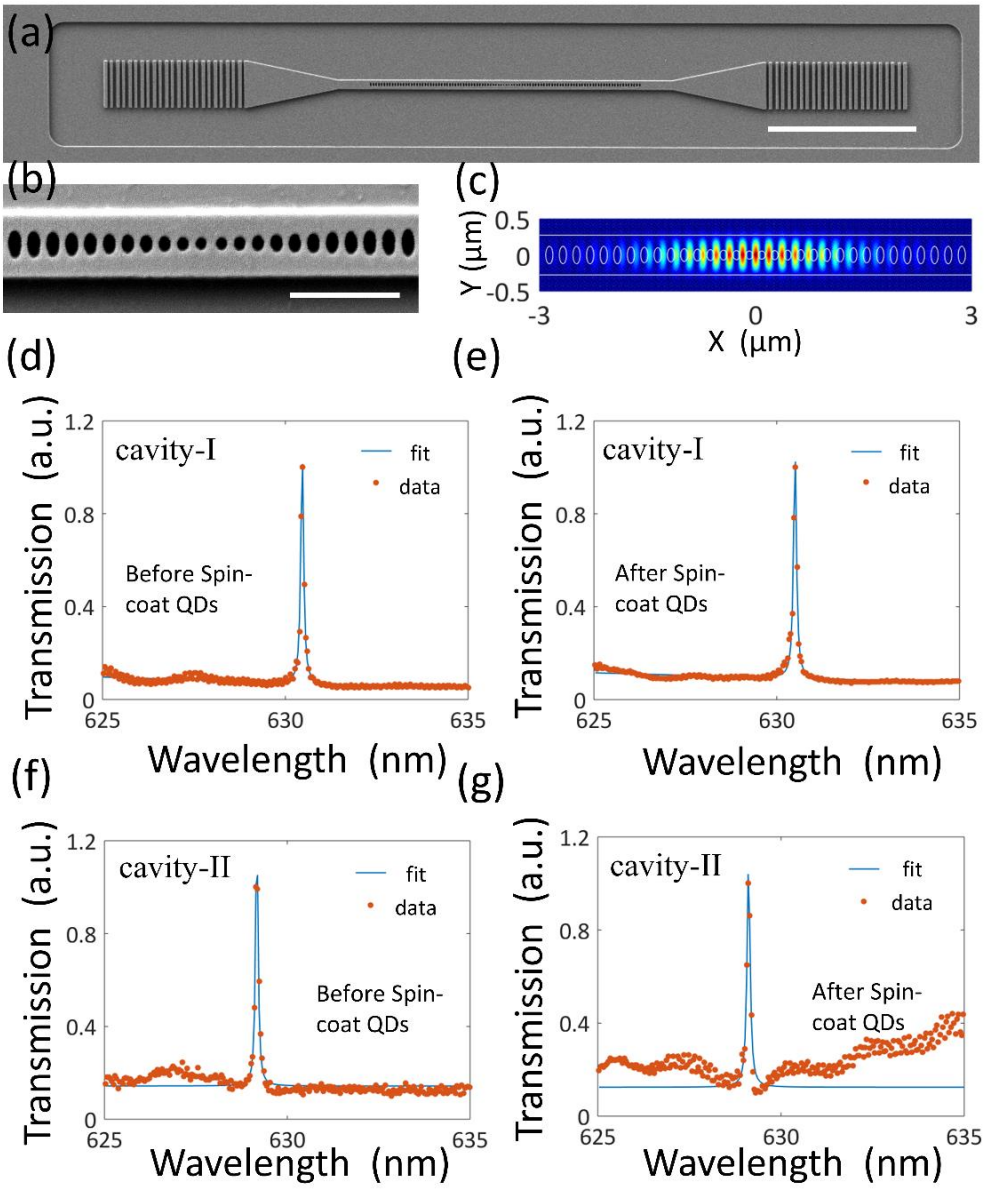

Figure 2.2. Cavity transmission characterization. (a) SEM of the silicon nitride cavity, where the nanobeam is unsuspended and sitting on the silicon oxide; scale bar: 10 μm. (b) Zoom-in on the cavity region; scale-bar: 1 μm. (c) Simulated cavity mode profile via FDTD (d) Transmission spectrum of the cavity without a PMMA window (Cavity I) before spin-coating colloidal QDs (Q~6900) and (e) after spin-coating colloidal QDs (Q~6600) (f) Transmission spectrum of the cavity with a PMMA window (Cavity-II) before spin-coating colloidal QDs (Q~7600) and (g) after spin-coating colloidal QDs (Q~6200). The results indicate that Cavity I can still retain high-Q operation under organic polymer cladding. Due to the limited QD absorption, the spin-coating of QDs does not dramatically degrade the Q-factor of Cavity II.

2.3 Deterministic positioning of the QDs

We first performed an overlay process using electron-beam lithography to define small square-shaped windows with different side lengths (1.5 μm, 750 nm, 500 nm, and 300 nm) in the PMMA resist that had been placed on top of the chip containing multiple nanocavities. The locations of the windows were chosen to coincide with those of the antinodes of the cavity modes. We also left some cavities inaccessible to the QDs without any PMMA window.

Following this setup, we dissolved 10 nM QD in 10:1 hexane and octane, filtered through a 450 nm Polyvinylidene Fluoride (PVDF) filter, and then spun coat the QD solution to get a uniform thin film on top of the device. From ellipsometry measurements, the QD thin film had a thickness of 80 nm and refractive index of ~ 1.5. We note that while pure CdSe has a refractive index of ~ 2.3, the whole thin film has a lower index due to the presence of organic ligands and solution residues.

We first compared the device performance before and after the solution deposition. For cavities without PMMA windows, the Q-factor remained the same both before and after the QD deposition, indicating that the QDs did not couple to the cavities. Figure 2.2d and 2.2e are the transmission measurement results before and after solution deposition. For cavities with PMMA windows, the spectrum before the electron beam exposure and solution deposition is shown in Figure 2.2f, with the Q-factor of 7600. The cavity resonance disappeared after the electron beam exposure and before the solution deposition, since the change of the refractive index in the window region (filled with air) dramatically perturbed the mode and degraded the Q-factor. We confirm this via FDTD simulation. In the FDTD simulation, a cavity with Q-factor of $\sim 10^5$ dropped to 1200 when a $1.5\mu m \times 1.5\mu m$ window is opened up in its PMMA. However, after the QD deposition as shown in Figure 2.2g, the cavity recovered to an experimentally verified Q-factor of 6200.

Having confirmed the robustness of the cavity resonance in the presence of PMMA windows, we performed the photoluminescence (PL) measurement. Figure 2.3a shows the SEM of the device with an overlaid schematic of a $1.5\mu m$ PMMA window. The experiment is performed as follows: A continuous wave (CW) green diode laser ($\lambda \sim 532$ nm) was used to pump the center of the cavity where the PMMA window was located. The laser was focused to a 1-μm-diameter beam spot by an objective lens with NA= 0.65. We also used a 550 nm low-pass filter to block the pumping light in the collection path. We first confirmed the QD-cavity coupling by pumping the QDs and observing PL coming out of the grating couplers with a CCD camera (Figure 2.3b). For more detailed analysis of the light, we used a spectrometer. The compact size of our device (tens of micrometers) allows us to pump at the center and collect from the grating couplers in our home-built confocal microscope, a routine procedure in both biology and optics experiments [71,72]. Since the PL signal coming from the window location was much brighter than that coming from the grating couplers, we used a pinhole to collect the light only from the grating coupler when we were studying the cavity signal (Figure 2.3c). The cavity mode at 629 nm matched with our transmission measurement. We note that another mode at 612 nm appeared in the PL measurement compared to just a single mode observed for the cavity before the QDs were applied. We attribute this to the slight refractive index difference of the QDs with PMMA. The higher refractive index of the QDs breaks the z-directional symmetry of the cavity, and through numerical simulation, we confirmed it was indeed a new TM mode [70]. However, as shown in Figure 2.3c, for a cavity with no PMMA window, when we collected PL signal from the grating, we only observe scattered background signal and no cavity signal. We were able to observe coupling down to the smallest window (300 nm side length) on the chip, indicating our deterministic positioning mechanism is robust. Further improvement of the viscosity of the solution should allow the QDs to get into even

smaller windows. In addition to tuning the spatial position for controllable coupling, we also achieved spectral control of the PL coupled to the cavity by fabricating cavities with linear change of Bragg period on the same chip. Figure 2.4a shows the PL coupled with cavities with different resonance, covering the whole PL emission spectral region of the QDs.

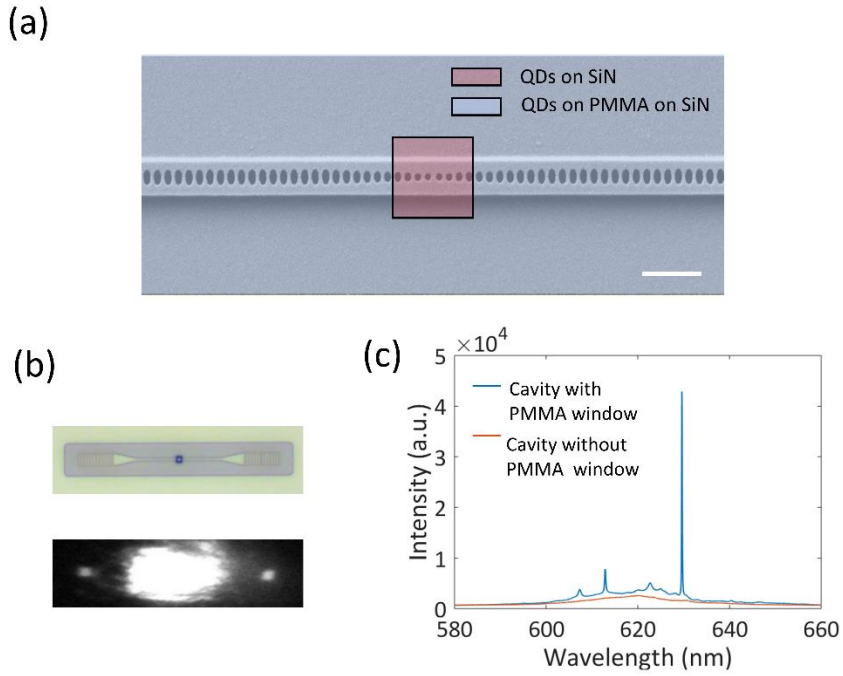

Figure 2.3. PL characterization of the coupled QD-cavity system. (a) SEM of the Cavity II; scale bar: 1.5μm. A schematic of the outline of the opened window is superimposed with the SEM. (b) An optical microscope image showing the opening on the cavity. The image of the cavity captured in the PL measurement setup after pumping the Cavity II. The lighting up of the grating couplers indicates the coupling between the QDs and cavity. (c) PL spectrum: For a cavity with a PMMA window, the cavity signal (resonances at 629nm and 612nm) is clearly observed against the PL background. A new TM mode at 612nm appears compared with the transmission measurement, originating from the slightly higher refractive index of the QDs breaking the z-directional symmetry of the cavity. For a cavity without a PMMA window, no cavity coupling is observed, as expected.

2.4 Purcell enhancement and Saturable Photoluminescence

We further confirmed the cavity enhancement by performing lifetime measurements (Figure 8b). Figure 2.4b shows the comparison of the QDs on the same chip with and without the cavity. We fit the data with a stretched exponential decay model [73]:

$$\mathrm{I(t)} = I_0 + Ae^{-(t/\gamma_0)^{\beta}}, \text{(2.1)}$$

The average lifetime is given by:

$$\gamma_{avg} = \frac{\gamma_0}{\beta}\Gamma\left(\frac{1}{\beta}\right), \text{(2.2)}$$

The Purcell enhancement factor is given by:

$$F_{max} = 1 + \frac{3\lambda^3}{4\pi^2 n^2}\frac{Q_{np}}{V}\psi(r), \text{(2.3)}$$

Here, $\Gamma\left(\frac{1}{\beta}\right)$ represents the gamma function with $\frac{1}{\beta}$ as the input parameter; λ is the cavity resonance wavelength; Q_{np} is the Q-factor of the quantum dot emission linewidth; n is the refractive index of the cavity dielectric; V is the cavity mode volume; and $\psi(r)$ is the ratio of the mode intensity at the emitter's location over the maximum. We note that we are using the Q-factor of the emitter but not the cavity since we are in the "bad" emitter regime, where the linewidth of the emitter is much larger than that of the cavity [74]. For our device, the linewidth of the QD emission was 23 nm, giving a Q-factor of 27; the numerically estimated mode volume is $2.5\left(\frac{\lambda}{n}\right)^3$; $\psi(r)$ is 0.35 as the QD interacts only with the evanescent field of the cavity; the refractive index of SiN is 2. With these values, the theoretically calculated Purcell factor is 1.4. We extracted a lifetime of 4.8 ns for the PL emission and 3.8 ns for the cavity coupled PL emission, indicating a Purcell factor of 1.26. The slight discrepancy between the measured Purcell enhancement and the theory is attributed to the fact that some of the QDs were not located at the field maximum on the surface. We note that due to our higher mode volume compared to those of suspended cavities, our

Purcell enhancement factor was smaller than the largest value (4.2) reported in a dielectric resonator [63]. However, by further optimization, a lower mode-volume resonator can be realized [75]. For example, by exploring a nanobeam design with a slot structure [76], one could dramatically reduce the mode volume while maintaining a high Q-factor, and thus a much higher enhancement factor.

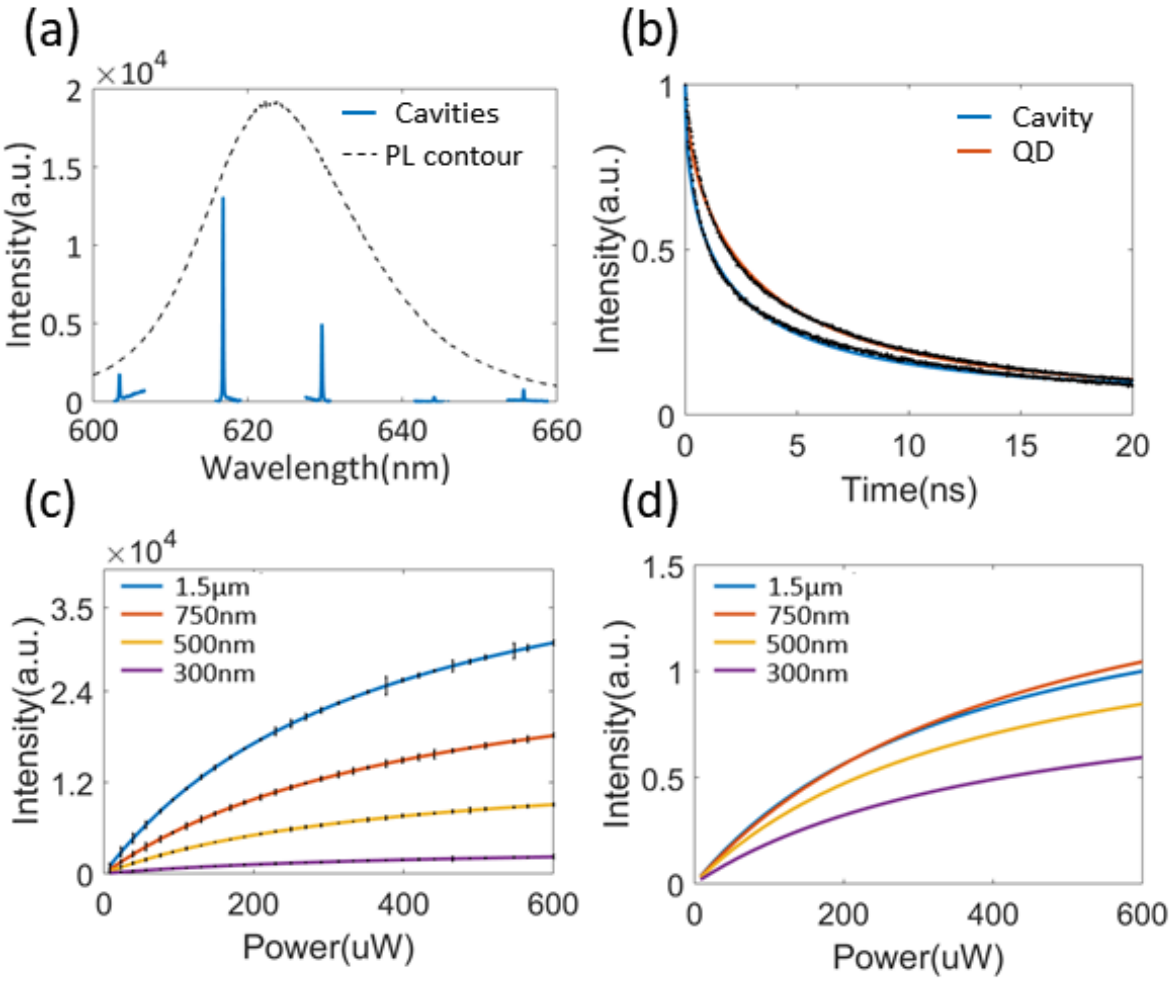

Figure 2.4. Spectral and spatial control of the QD-cavity coupling. (a) We show the cavity-coupled PL over the whole resonance spectrum by positioning QDs on cavities with scaling geometry. The black dotted curve shows the contour of the PL. (b) Lifetime measurement: The solid red and blue curves are the fits to the time-resolved PL signal from the QDs on substrate and the QDs coupled

with the cavity, respectively. The black dots are the raw experimental data. A Purcell factor of 1.26 is measured. (c) Power series for cavities with PMMA windows with different sizes: 1.5μm × 1.5μm, 750nm×750nm, 500nm×500nm, 300nm×300nm. As the size of the window grows, the cavity signal in PL increases since more QDs are interacting with the cavity (d) Power series for cavity-coupled PL normalized by the mode area of the cavity inside the window region.

To further explore the possibility of controlling the number of QDs coupled to the cavities, we performed power series measurements of samples with different window sizes (Figure 2.4c). The difference in the photoluminescence intensity was observed: cavities with larger windows had brighter emission in general. To get a more quantitative understanding of how the size of the window affected the number of QDs coupling with the cavity, we normalized the emission intensity according to the cavity mode area exposed by the windows (Figure 2.4d). From the FDTD simulation, the mode areas for the $1.5\,\mu m$, $760\,nm$, $500\,nm$, and $300\,nm$ windows are $0.23\mu m^2$, $0.13\mu m^2$, $0.08\mu m^2$, and $0.03\ \mu m^2$, respectively. We saw that the intensity curves for the 1550 nm and 750 nm windows almost overlapped on top of each other after the normalization. For the device with 500 nm and 300 nm windows, however, the intensities were lower than those with the larger window cavities, with the intensity for the 300 nm window even lower than that for 500 nm window. We attribute this observation to the fact that as the windows become smaller, the QDs are no longer able to enter the cavities efficiently due to the surface tension of the solution. However, further surface modification and solution with lower viscosity could potentially allow more QDs to enter the windows. For all the window sizes examined, we observed that the photoluminescence saturated when pumped with increasing laser power. We fit the data and extracted saturation power to be ~400 μW. We did not observe any significant difference in the

saturation power for different window sizes, since the intensity of the pumping light on each QD was essentially the same in all four cases.

While the simple nature of our patterning technology has been instrumental in demonstrating our novel, straightforward procedure for achieving determining positioning of the emitters, to push the limit further to few/single QDs, we need to explore more advanced synthesis of colloidal quantum dots. We estimate the current number of QDs coupled with the cavities and outline one possible approach towards few/single dot coupling with the cavity by using giant QDs [77,78]. Recently, a series of works involving the Langmuir-Blodgett deposition, a thin-film resist, and the resist lift-off has reported successful deterministic positioning of a single colloidal QD [67]. This technique appears highly promising as a route to obtaining single emitters and may be combined with the encapsulated cavity design reported here to yield deterministic positioning and coupling of single QDs to multiple cavities.

2.5 Deterministic positioning of QDs on a photonic molecule

One promising application of our deterministic positioning method is performing quantum many-body simulations [79] using QDs coupled to a cavity array. The simplest array, made up of just a pair of coupled cavities, is called a photonic molecule [80]. It has been shown in several theoretical studies that QDs coupled to a photonic molecule may form the basis for studying exotic phases of matter [81] and other cavity quantum electrodynamics phenomena such as unconventional photon blockade [80,82]. However, both scalability and deterministic positioning are difficult to achieve with conventional self-assembled semiconductor QDs coupled with suspended coupled nanobeam cavities. Besides, the mode symmetric nature of the coupled cavity super-modes also precludes the reflection measurement of photonic crystals by directly pumping and collecting a laser signal at

the center of the cavity [83]. Here we fabricate the photonic molecule with grating couplers for each cavity for transmission measurements and deterministically position the QDs to couple with the cavity super modes. Figure 2.5a shows the SEM of the fabricated device. Each cavity has a pair of grating couplers that allows measuring transmission from each cavity independently. We fabricated two coupled cavities with different gaps between them: 1.5 μm, 400 nm, and 200 nm (Figure 2.5b). Figure 2.5c shows the transmission spectrum measured via the grating for Cavity 1. For cavities 1.5 μm apart, we observed only one cavity in transmission, indicating there is no coupling between two cavities. For cavities 400 nm and 200 nm apart, we observed two coupled super-modes. As the distance becomes smaller for the two cavities, the coupling strength becomes stronger, resulting in larger spectral separation of two modes.

We then opened up 750nm PMMA windows on cavity 2 and spin-coated it with the QD solution. We adjusted the collimation of the pumping beam so that both cavities are illuminated, and we collected PL from gratings for both cavities. The results are shown in Figure 2.5d. For 1.5 μm apart cavities, we only observed the cavity signal from the grating for cavity 2, since the gap was too large for the two cavities to couple. For cavities 400 nm and 200 nm apart, we successfully observed coupling between the QDs and the super-modes at both gratings for cavity 1 and cavity 2. This approach can be readily scaled up to an array of multiple coupled QD-cavities.

While the simple nature of our patterning technology has been instrumental in demonstrating a novel, straightforward procedure for achieving determining positioning of the emitters, to push the limit further to few/single QDs, we need to explore more advanced synthesis of colloidal quantum dots. Recently, a series of works involving the Langmuir-Blodgett deposition, a thin-film resist, and the resist lift-off has reported successful deterministic positioning of a single colloidal QD [67]. This technique appears highly promising as a route to obtaining single emitters and may

be combined with the encapsulated cavity design reported here to yield deterministic positioning and coupling of single QDs to multiple cavities.

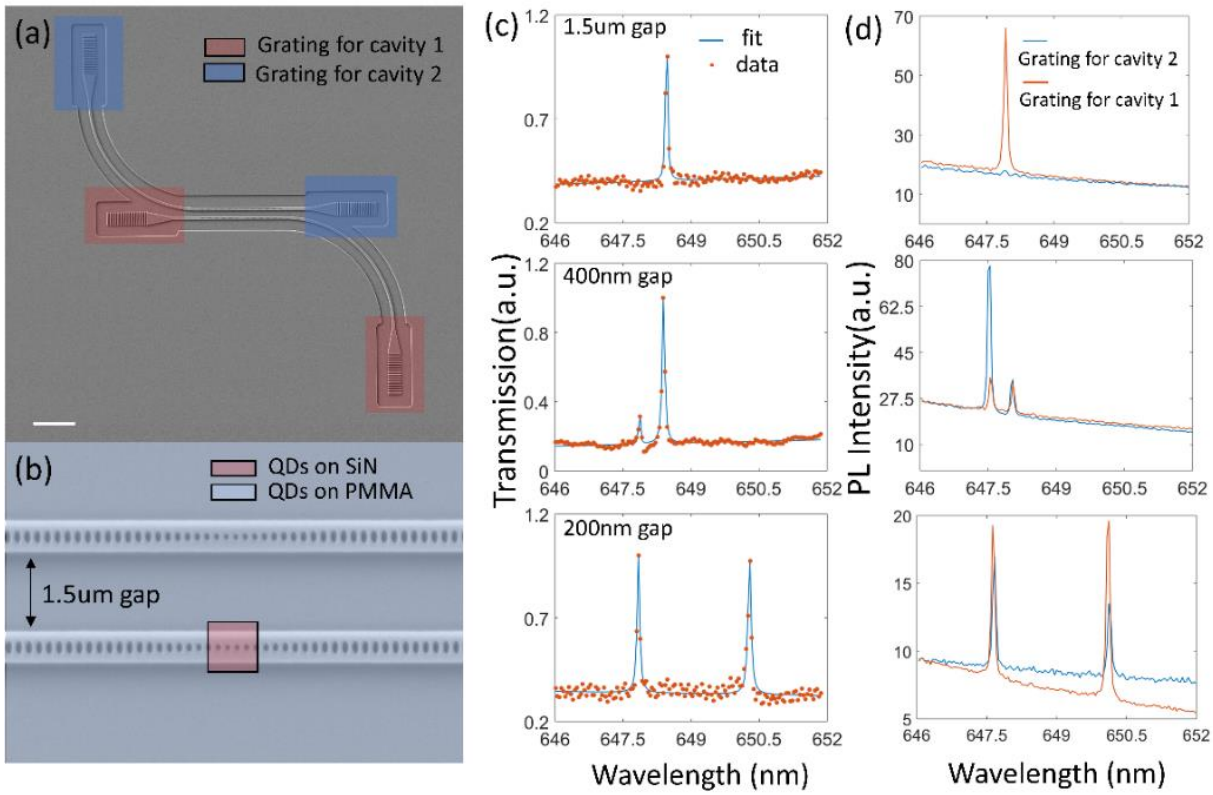

Figure 2.5. Deterministic positioning of QDs on a photonic molecule. (a) SEM image of the photonic molecule. Each cavity has a pair of grating couplers for collecting and extracting the QDs' PL; scale bar: 10μm. (b) Schematic of the outline of the opened window superimposed with the SEM of the device. (c)Transmission measurement of the device with different separation gaps before spin-coating QDs. For cavities 1.5μm apart, we saw only one cavity resonance in transmission, indicating no coupling between the two cavities. For cavities 400nm and 200nm apart, as the distance becomes smaller for the two cavities, the coupling strength becomes stronger, resulting in larger spectral separation of the two supermodes. (d) PL characterization: For cavities 1.5um apart, we observed the cavity signal from the grating for cavity 2, since the PL signal was only coupled with cavity 1 and the two cavities were not coupled with each other. For cavities 400nm and 200nm apart, we successfully observed the coupling between the QDs and the super-modes at both gratings for cavity 1 and cavity 2.

Another way to push the limit further to few/single QDs would be fabricating windows with smaller side-length (~50 nm) and synthesizing giant QDs [77] (~50nm diameter). In the horizontal plane (x-y plane) of our device, currently advanced EBL patterning technology is readily able to pattern sub-50nm structures, which would make sure that the hole size is suitable for only one QD. In the lateral direction (z plane), depending on the concentration of QDs we are spin-coating, there might be multi-layer of QDs presenting on top of the cavity. However, as the QDs are evanescently coupled with the cavity mode, the exponential decay of the $|E|^2$ should be faster compared with the size of the giant QDs. As shown in Figure 2.6, the first QD is experiencing three times larger energy density than the second one. And the rest are experiencing negligible cavity field. If we assume there is no gap between the two QDs, in the worst case, there would be only two QDs effectively seeing the cavity field. There would also be passivating organic ligand between the QDs so that the gap between QDs could be even larger [84]. Special chemical treatment could be further adapted to the surface of QDs to let them repel each other and increase the between-dots separation [85,86]. Also, the thickness of the slab could be adjusted to make the field more confined in the slab so that the field decay much faster, but it requires more design since there is always a tradeoff between the absolute energy density at the QD1's position and the ratio between QD1 and QD2.

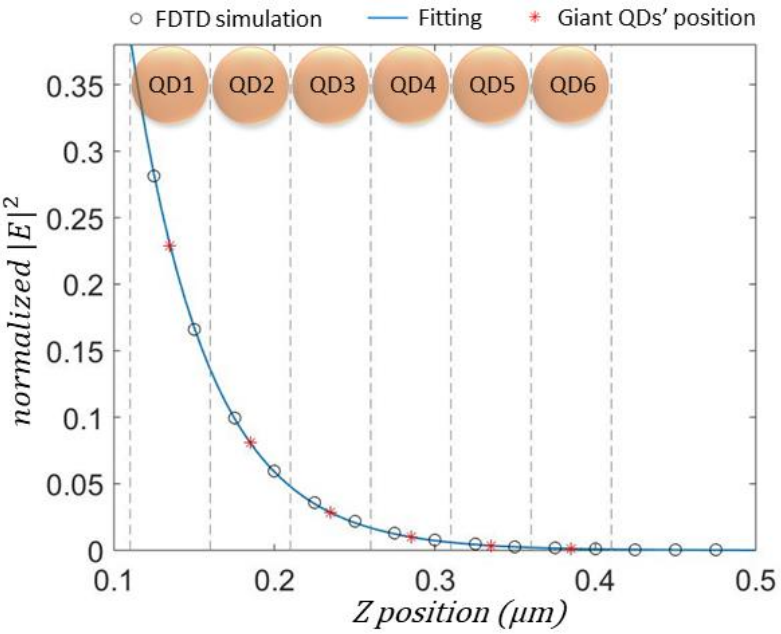

Figure 2.6. The black dots are the FDTD simulation $|E|^2$values of the evanescent field distribution. The blue curve is the fitting of the evanescent field. The red star points are the position of the giant QDs, assuming there is not gap between them.

2.6 Extension to other solution-processed material

Recently, perovskite nanocrystals emerge as another novel light-emitting material with excellent optoelectronic properties [53,54]. Lead halide perovskites exhibit several favorable properties for light-emitting devices, including high photoluminescence (PL) quantum yield attributed to the low densities of defects [55,56], which reduce the nonradiative loss via carrier trapping. The large stokes shift in the emission of these perovskites also reduces the carrier loss to detrimental reabsorption. Combined with the large exciton binding energy, indeed, there have been many demonstrations of perovskite light-emitting devices such as LED and lasers capable of operating at room temperature [57,58].

Here we demonstrated the coupling of perovskite nanocrystals to the encapsulated silicon nitride nanobeam photonic crystal cavity at room temperature. As determined from the time-resolved photoluminescence decay measurements, we observed enhanced spontaneous emission from the perovskite nanocrystals by a factor of 1.4, consistent with simulation. In addition, by varying the concentration of the perovskite nanocrystal in the PMMA layer, the effective index of the layer can be modified, allowing us to use it as a method to tune the cavity mode resonance. Our results show that solution-processable perovskite nanocrystal could prove to be promising for applications such as on-chip light sources, optoelectronic devices and photonic integrated circuits.

The $CsPbBr_3$ Perovskite nanocrystals were dispersed in toluene and were synthesized following the procedures described in ref [93]. The perovskite nanocrystal solution was then mixed with PMMA formulated in anisole (MicroChem 950PMMA A4). We prepared solutions of perovskite nanocrystals with different concentrations. We injected a varying amount of anisole (Aldrich, anhydrous 99.7%) – 0 ml, 5 ml and 10 ml – to a fixed 10 ml of PMMA solution before mixing with about 0.1 ml of perovskite nanocrystal solution. With increasing volume of anisole, the solution becomes more dilute and the concentration of perovskite nanocrystals in PMMA is reduced. In order to couple the perovskite to the cavity, the solution was then spin-coated on the nanobeam sample at 4000 rpm for 1 minute, which effectively places the nanocrystals on the cavity and at the same time encapsulating the nanobeam. Taking the thickness of the PMMA layer to be the length from the surface of the substrate to the top of the PMMA layer, the thickness is expected to be about 400 nm according to the manufacturer data sheet.

Optical experiments on the samples were carried out in a confocal microscopy system at room temperature. For the time-averaged measurements, a continuous wave He-Cd laser excitation at 442 nm was focused (100× objective lens, NA = 0.90) onto the sample. The emission spectra were

measured with a Horiba HR Evo spectrometer with a focal length of 800 mm together with a 300 lines/mm grating and liquid nitrogen cooled Si CCD detector. For time-resolved decay measurements, a Ti: Sapphire femtosecond-pulsed laser with ~100 fs pulses at 80 MHz was used. The emission of the laser was frequency-doubled to output 400 nm pulses. The emission from the sample was detected with an avalanche photon detector (Micro Photon Devices) connected to a single photon counting module (PicoHarp 300). The overall temporal resolution of the time-resolved setup was measured to be about 22 ps.

Figure 2.7a shows a series of spectra corresponding to PMMA layers with decreasing perovskite nanocrystal concentration. The PL emission of the $CsPbBr_3$ perovskite nanocrystals is centered at 520 nm. The spectra also show the narrow cavity mode resonances at longer wavelengths relative to the perovskite nanocrystal emission as indicated by the arrows above the peaks. The background PL in the spectra can be attributed to emission from the perovskite nanocrystals which are not coupled to the cavity as well as the scattered light off the nanobeam.

To further study the coupling between the perovskite nanocrystal with the encapsulated nanobeam, we spun-coat the PMMA mixed with perovskite solution with different concentrations. As the perovskite nanocrystal in the PMMA layer decreases, we found that cavity mode resonance becomes increasingly blue-shifted. We attribute the blue-shift of the mode resonance to the change in the effective index of the encapsulating PMMA. Decreasing concentration of $CsPbBr_3$ (index~2.6) in PMMA (index~1.5) will result in the overall decrease in the effective index of the encapsulating layer of the nanobeam, and blue-shifting the cavity mode. In fact, the simulated mode resonance wavelength exhibits a monotonic decreasing trend with the reduction of the

effective index of the PMMA layer as shown in Figure 2.7b, consistent with experimental observation.

By peak fitting, we could extract the mode wavelength, λ_{cav} and the linewidth at full-width half-maximum ($\Delta\lambda_{FWHM}$) to determine the experimental $Q = \lambda_{cav}/\Delta\lambda_{FWHM}$ of the cavity modes. The calculated Q-factors for the spectra increase from ~900 to ~1500 with decreasing perovskite concentration. From the simulations, the Q-factor increases with the decrease of the effective index of the PMMA layer, again, consistent with the experiments. The decrease of the effective index of the PMMA layer raises the index contrast between the layer and the nanobeam, thus the higher Q-factor.

We note that the change in the Q-factor with the effective index of the PMMA is not always monotonic as we have found from simulations that the Q-factor could be higher at intermediate index values between 1.5 and 1.8 with 30 or 40 holes in the Bragg region. The dilution of PMMA with additional anisole could also reduce the thickness of the PMMA layer which has a small but nonnegligible reduction on the cavity mode wavelength. Therefore, with the appropriate design of the nanobeam PhC cavity, the effective index and the thickness of the PMMA layer allows for additional degrees of control to tune not only the cavity resonant wavelength but also the Q-factor. It is worth highlighting that all the measurements were performed on the same cavity. Aside from the changing Q-factor as a consequence of the varying effective index of the PMMA layer, the cavity showed no significant degradation despite having undergone multiple rounds of sonication with acetone and spin coating of the PMMA layer, proving that the nanobeam PhC cavity is structurally robust. This tuning method of the mode resonance via the effective index around the cavity environment could be useful for the coupling of other colloidal quantum emitters to cavities, possibly with other types of capping layer besides PMMA.

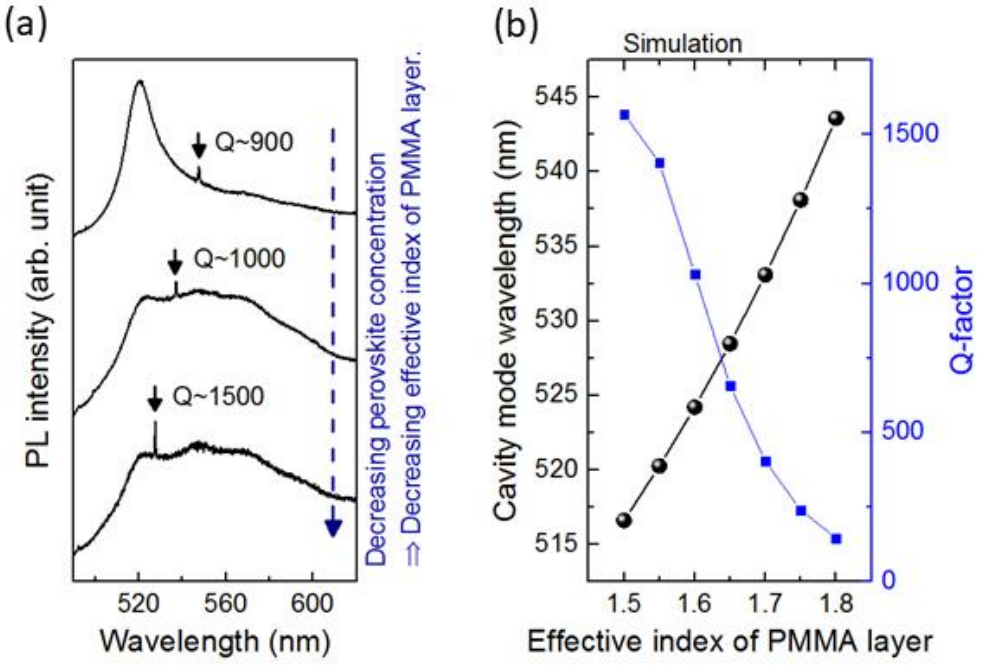

Figure 2.7. Tuning of cavity mode resonance. (a) A series of spectra corresponding to the decreasing perovskite concentration in the direction of the dashed arrow. The spectra show the broad perovskite PL emission peak center at 520 nm and the narrow cavity mode resonances as indicated by the arrows along with the respective Q-factors. The mode resonant wavelength decreases with the decreasing concentration of perovskites in the PMMA layer. (b) The simulated cavity mode resonant wavelength (black spheres) decreases with the decrease of the effective index of the PMMA layer, while the Q-factor (blue squares) shows the opposite trend.

To verify the spontaneous emission enhancement of the perovskite nanocrystal coupled with the cavity, we measured the time-resolved PL decay of the perovskite emission. The PL decay curves of the perovskite emission from the coupled and uncoupled cases are presented in Figure 2.8. The perovskite nanocrystal PL exhibits a multiexponential decay due to a distribution of the nanocrystal parameters such as size and nonradiative decay rate. Assuming that the perovskite nanocrystals ensemble consists of 3 main subpopulations, each with a characteristic decay behavior, the decay curves were most accurately fitted with a three exponential decay function:

$I(t) = I_0 + A_1 e^{-[(t-t_o)/t_1]} + A_2 e^{-[(t-t_o)/t_2]} + A_3 e^{-[(t-t_o)/t_3]}$ where $I(t)$ is the PL intensity at time *t*, I_0 is the background intensity, t_o is the temporal offset relative to 0 when the decay begins and t_i (A_i) with $i = 1, 2, 3$ being the three decay time constant (amplitude). We take the shortest decay time t_1 as the representation radiative lifetime since the fractions of the amplitude, $A_i/(A_1 + A_2 + A_3)$ are close to 1 in both the coupled and uncoupled cases, implying that the subpopulation of the nanocrystal with characteristic decay time t_1 is dominant. The t_1 times are extracted to be 0.65 ns and 0.46 ns respectively for the coupled and uncoupled cases, consistent with previous report [94]. Taking the ratio of t_1 of the uncoupled case to that of the coupled case, we obtained a Purcell factor of ~1.4, indicating the enhancement of spontaneous emission.

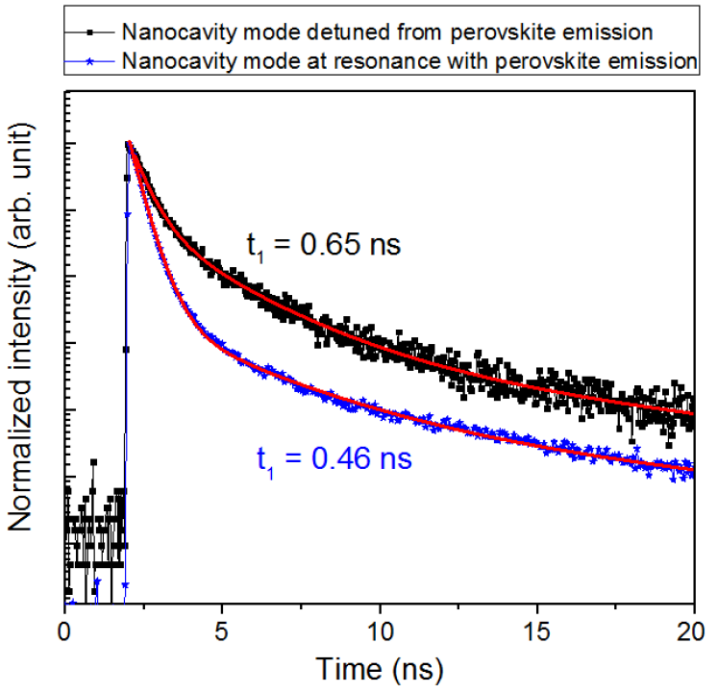

Figure 2.8: Plot comparing the PL decay of the perovskite nanocrystals in two different cases: one which is coupled to the cavity (blue) and the other uncoupled (black) with the respective t_1 decay time as labelled.

To estimate the theoretical Purcell enhancement based on the FDTD simulations, we employ the following equation for the Purcell factor [95]: $F_p = 1 + \frac{3\lambda_{cav}^3}{4\pi^2 n^2}\frac{Q_e}{V_{mode}}|E|_{local}^2$ where λ_{cav} is the mode resonant wavelength, n is the refractive index of SiN, Q_e is the Q-factor of the emitter and V_{mode} being the mode volume. In consideration of the local density of states, one would also need to factor in the local electric field intensity expressed as $|E|_{local}^2 = |E(\boldsymbol{r})|^2/|E(\boldsymbol{r})|_{max}^2$ where $\boldsymbol{r}$ is the position of the emitter. We note that this model of Purcell factor is appropriate for our experiments since the emitter emission linewidth is larger than that of the cavity mode linewidth. In this case, the Purcell factor depends on the Q-factor of the emitter and not that of the cavity. By performing multiple peak fit to the spectra of the uncoupled case, the full-width at half-maximum linewidth of the perovskite nanocrystal emission was found to be 20 nm and thus giving a Q-factor of about 26. From the FDTD simulations, V_{mode} was found to be ~$3.7(\lambda/n)^3$. Assuming that the emitter is located at the center of the nanobeam cavity on the surface gives $|E|_{local}^2 = 0.37$. The resulting Purcell factor is obtained to be 1.38 consistent with experimental results.

Chapter 3 Tunable silicon nitride cavities

3.1 Introduction

Apart from the deterministic positioning mechanism demonstrated in Chapter 2, the tunability of photonic crystal nanobeam cavity is necessary for a scalable QD-cavity platform. Unfortunately, efficient tuning of SiN devices remains difficult: as a centro-symmetric material with a large bandgap, SiN has a low thermo-optic coefficient (~ 10^{-5}/°C) and lacks both free-carrier dispersion and second order nonlinearity.

In this chapter, we experimentally demonstrate an SU-8 polymer-embedded SiN nanobeam cavity with a high tuning efficiency of 44 pm/°C and 0.13 nm/mW in the near-visible wavelength range. The key to this high tunability is the large thermo-optic (TO) coefficient (~ 10^{-4}/°C) [96] and low thermal conductivity of the polymer. The SU-8 polymer is chosen because of the high TO coefficient [97,98], ultralow absorption in the near-visible wavelength range [100] and its compatibility with the photonics crystal structures as shown previously [98,99]. The ease of spin-coating SU-8 on a SiN substrate also makes the integration process straightforward, and several experiments have already demonstrated such integration [100]. We also demonstrate the active tuning of a heterogenous photonic molecule comprised of a nanobeam coupled with a ring resonator. Leveraging the different tuning efficiency between the nanobeam and the ring, we experimentally showed the strong coupling between the two cavities by the anti-crossing signature. Furthermore, we predict the tuning of the hybridized mode volume by fitting the experimental result with a theoretical framework.

3.2 Tunable polymer-SiN nanobeam cavity

3.2.1 Simulation

The schematic of the device is shown in Figure 3.1. The SiN nanobeam sits on a silicon oxide substrate, with the SU-8 polymer cladding and filling the patterned holes. The polymer-SiN nanobeam cavity is designed to have an 'air-mode' [101–104], in which a large portion of the electromagnetic field is confined inside the low index material, which, in our case, is the polymer. A gold heater is fabricated next to the patterned holes; passing a current heats up the polymer and subsequently tunes the cavity resonance.

We first design the polymer-SiN air-mode nanobeam cavity. Due to the relatively low refractive index contrast of SiN (n = 2) to SU-8 polymer (n = 1.574) and silicon dioxide (n = 1.45), it is nontrivial to design a high Q photonic crystal cavity on this platform [71]. Compared to the traditional suspended SiN nanobeam cavity, our on-substrate nanobeam cavity also increases the mechanical robustness of the cavity and eliminates the risk of the structure breaking during the fabrication. In our design, the SiN unit cell has a Bragg period $a = 225\ nm$ and a width of $w = 500\ nm$, comprising an elliptical hole with the long axis equal to 290 nm and the short axis equal to 116 nm. A SU-8 cladding layer filling the holes with a thickness of 500 nm is incorporated in the band structure calculation, performed via MIT photonics bands (MPB) [105] (Figure 3.2a). There are two bands below the light cone. We focus on the upper band (shown in red), known as the 'air band', where a large portion of the electromagnetic field is distributed inside the SU-8 regime, as shown in the cross-section diagram in Figure 3.2b.

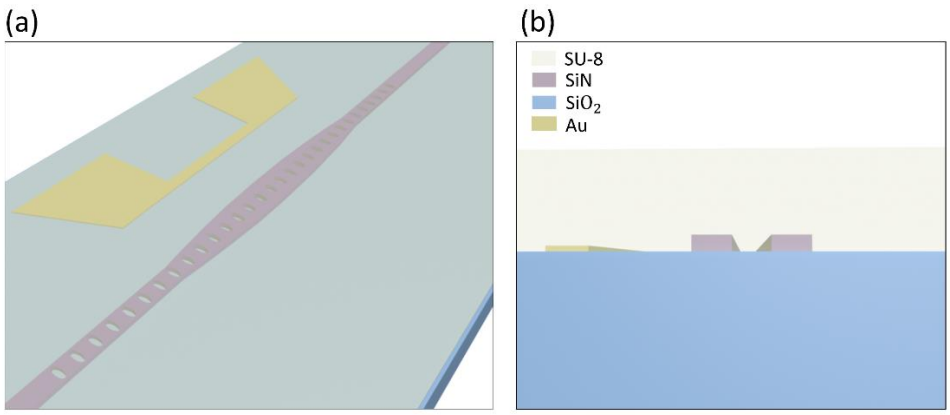

Figure 3.1. Schematic of the polymer-embedded SiN resonator, with an electrical heater placed nearby.

We then define the high-Q air-mode by tapering the waveguide width from the Bragg region (500 nm) to the center (699 nm) following the relation: $w(x) = w_{center} + x^2(w_{end} - w_{center})/x_{max}{}^2$ [97], where x increases from zero (at the center of the nanobeam) to the end of the taper region. The number of periods in the Bragg region (taper region) is 20 (30), with the period fixed at 225 nm. Figure 3.2c shows the cavity mode profile calculated via FDTD simulation. The cavity has anti-nodes inside the holes, which is filled by the polymer. The cavity mode has a wavelength of ~730 nm with a Q-factor of ~10^5. The mode volume is calculated as $20(\frac{\lambda}{n_{su-8}})^3$. We note that the mode volume is larger than conventional photonic crystal , but it is still significantly smaller than other on-chip silicon nitride resonators [107,108].

We simulate the TO tuning of the device using FDTD method. The tuning of the effective mode index of the nanobeam cavity could be expressed in the first order as

$$\frac{dn_{eff}}{dT}(\lambda) = \Gamma_{SiN}(\lambda)\,\frac{dn_{SiN}}{dT}(\lambda) + \Gamma_{SU-8}(\lambda)\,\frac{dn_{su-8}}{dT}(\lambda), \quad (3.1)$$

where $\frac{dn_{eff}}{dT}$is the effective TO coefficient, and $\Gamma_{SiN}(\lambda)$ and $\Gamma_{Su-8}(\lambda)$ represent the confinement factor of the cavity field inside the SiN and the SU-8 polymer region, respectively. We calculate the confinement factor (defined as $\frac{\int_{\text{region}} \varepsilon E^2 dV}{\int_{\text{mode}} \varepsilon E^2 dV}$) in SU-8, silicon nitride and silicon oxide as 47%, 41% and 12% from the cavity mode profile via FDTD simulation. $\frac{dn_{SiN}}{dT}$ and $\frac{dn_{SU-8}}{dT}$ are the TO coefficient of SiN ($\sim 2.45 \times 10^{-5}/°C$ [108]) and SU-8 polymer, respectively. The TO coefficient of uncured SU-8 is documented in the range from $-1.8 \times 10^{-4}/°C$ to $-3.5 \times 10^{-4}/°C$ [97,98], depending on the condition of fabrication.

Since the electromagnetic field possesses the highest confinement factor in the polymer region and SU-8 has a much higher (and negative) TO coefficient compared to SiN, we expect to observe a blue shift of the cavity resonance when we apply heat. As shown in Figure 3.2d, the cavity blue shifts by 6 nm (2.9nm) across a 100°C temperature increase, when the TO coefficient of the SU-8 is assumed as $-3.5 \times 10^{-4}/°C$ ($-1.8 \times 10^{-4}/°C$), corresponding to a tuning efficiency of 60 pm/°C (29 pm/°C). On the other hand, a bare SiN cavity with a dielectric mode is tuned by 0.9 nm across a 100 °C temperature increase, corresponding to a tuning efficiency of only 9 pm/°C. We also simulate an electrical heater using finite element method to identify the optimum distance of the heater from the cavity. A close proximity will give rise to strong absorptive losses from the metal, whereas if the heater is placed too far away, the cavity will not be heated. From the simulations, we found a good trade-off when the heater is 1.5 μm away from the nanobeam structure. As shown in Figure 3.2e, when the heater temperature is 250 °C, the temperature at the nanobeam reaches 100°C.

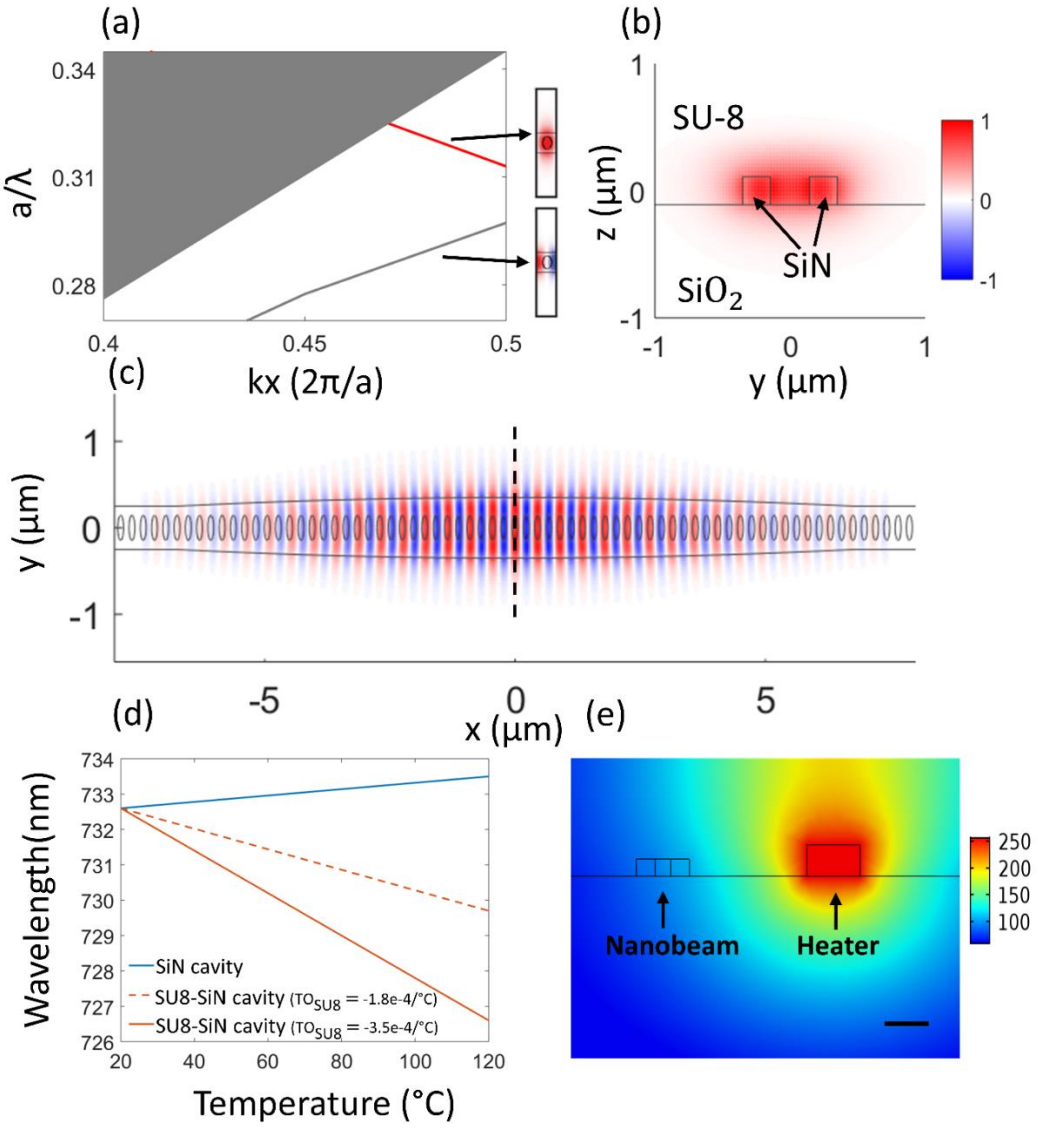

Figure 3.2. Device design. (a) Band structure of the unit cell. (b) Electric field distribution of the wave-guide cross-section for the air-band. (c) FDTD simulation of the cavity field distribution. (d) Comparison of the simulated tuning efficiency of a bare silicon nitride nanobeam cavity and the SU8-SiN nanobeam cavity. The blue line shows the tuning of a bare SiN cavity. The red dash line shows the tuning of a SU-8-SiN cavity assuming the TO coefficient of SU-8 as $-1.8 \times 10^{-4}/°C$. The red solid line shows the tuning of the SU-8-SiN cavity assuming the TO coefficient of SU-8 as $-3.5 \times 10^{-4}/°C$. (e) Thermal simulation shows that the side heater could efficiently heat up the cavity region. Scale bar: 500nm

3.2.2 Experiment

We then experimentally validated our theory. We fabricated the cavity using a 220-nm thick SiN membrane grown via LPCVD on 4 μm of thermal oxide on silicon. The samples were obtained from commercial vendor Rogue Valley Microelectronics. We spun roughly 400 nm of Zeon ZEP520A, which was coated with a thin layer of Pt/Au that served as a charging layer. The resist was then patterned using a JEOL JBX6300FX electron-beam lithography system with an accelerating voltage of 100 kV. The pattern was transferred to the SiN using a RIE etch in CHF_3/O_2 chemistry. The heating electrode with 500-nm width and 20-μm length is defined via electron-beam overlay and evaporation followed by a lift-off process. Figure 3.3a shows a scanning electron micrograph (SEM) of the fabricated SiN cavities on thermal oxide just after etching. Grating couplers are fabricated on both sides of the nanocavity for the transmission measurement. Figure 3.3b shows the parabolic tapering of the width of the nanobeam waveguide to confine the mode in the air. After the device is fabricated, we spun coat SU-8 on top of the cavity. We used SU-8-2000.5 from microChem because of its small viscosity needed to fill the holes. A similar experiment with a silicon photonic crystal cavity has been reported before showing that the holes can be filled with SU-8 [97]. After the spin-coating, we baked the chip at 95°C for 1min to further remove the solvent.

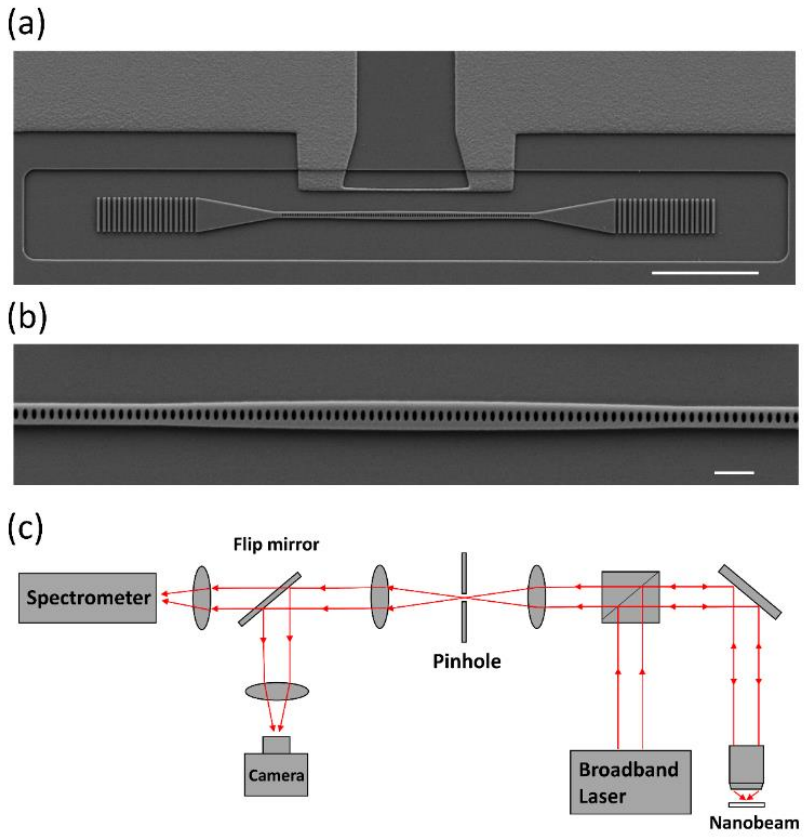

Figure 3.3. Fabrication and optical setup. (a) SEM image of the device shows the nanobeam cavity, grating couplers and metal heater. Scale bar: 10μm (b) Zoom-in image of the nanobeam: The width of the nanobeam waveguide is parabolically tapered to achieve a high Q-factor air-mode. Scale bar: 1 μm. (c) A confocal microscopy setup for the transmission measurement of the nanobeam cavity.

The cavities are characterized via measuring the transmission using a confocal microscopy setup (Figure 3.3c). A super continuum light source (Fianium WhiteLase Micro) is focused on the grating coupler through the objective lens, and a moveable pinhole is used to pick up the signal only coming out from the other grating and then send it to a spectrometer. The spectrometer is equipped with a Princeton Instruments PIXIS CCD with an IsoPlane SCT-320 Imaging Spectrograph. The cavity at room temperature has a Q-factor ~ 6500, and resonance wavelength

at 731 nm. The smaller Q-factor compared to our simulation result is attributed to fabrication imperfections due to small feature sizes at near-visible wavelength operation.

We first characterize the thermal tuning by heating up the whole chip in a hot plate. As shown in Figure 3.4a, between 20°C to 70°C, we tuned the cavity from 731.3 nm to 728.9 nm, corresponding to a tuning efficiency of 44 pm/°C. We fit the TO coefficient of the SU-8 by the experimentally achieved tuning efficiency in FDTD simulation and extract the value to be $-2.5 \times 10^{-4}/℃$, which lies in the range of the documented values [97,98]. Then we used the electrical heater to tune the cavity, as shown in Figure 3.4b. By applying 12.5 mW power to the side heater, we tuned the resonance by 1.625 nm, corresponding to a tuning efficiency of 0.13 nm/mW. We applied a train of square pulses (Power_High = 9.4 mW, Power_Low = 6.2 mW, Period = 1 s, Duty cycle = 30 %) to the metal heater in a continuous three-hour experiment, while the nanobeam cavity is irradiated by a super-continuum laser source for the cavity transmission measurement. We observed a consistent tuning of the cavity resonance between 729.6nm and 729nm on the spectrometer, which confirmed that the thermal tuning of polymer-SiN cavity is reversible and robust. We didn't observe any degradation of our device after 56 days after fabrication, which was confirmed by the consistent cavity quality factor that we measured.

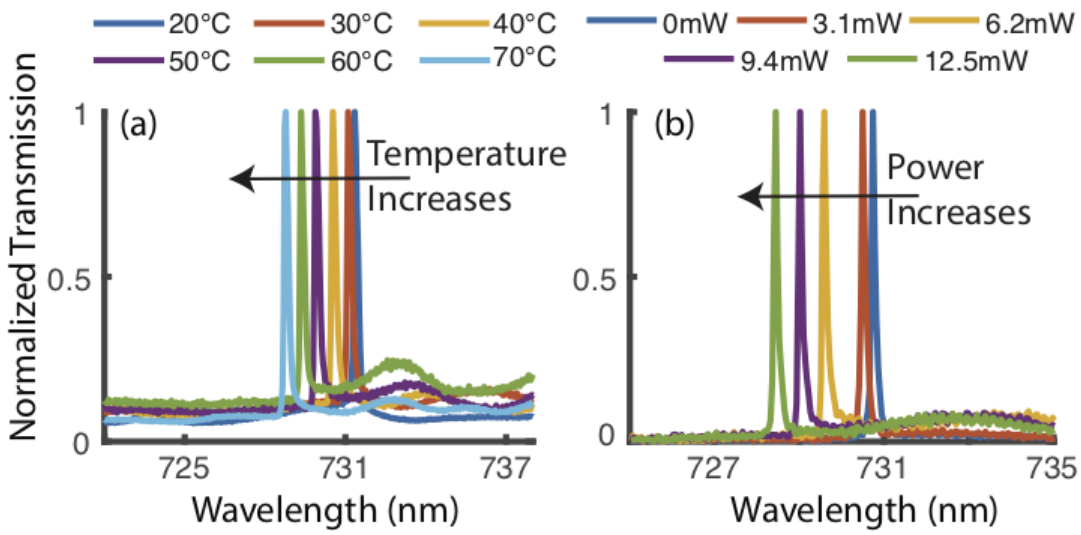

Figure 3.4. Tuning performance. (a) Hot plate tuning: The cavity is tuned from 731.3 nm to 728.9 nm by a temperature rising of 50 °C, corresponding to a tuning efficiency of 44 pm/°C, matching well with the theory. (b) Electrical heating: By applying 12.5mW power to the side heater, the resonance is tuned by 1.625 nm, corresponding to a tuning efficiency of 0.13 nm/mW.

To further analyze the thermal tuning performance of our device, we adapted the Lumped Element Circuit Model of the TO devices [109]. For a thermal-tunable optical resonator, the TO detuning corresponding to π phase shift is derived as [21]

$$\Delta\lambda = \frac{\pi\lambda_0}{Q}, \quad (3.2)$$

where, λ_0 is the cavity resonance wavelength and Q is the quality factor. For our device, the power required for π phase shift is calculated as

$$P_\pi = \frac{\Delta\lambda}{0.13nm/mW} = \frac{\pi\times730nm}{0.13nm/mW\times6500} = 2.7\ \text{mW}, \quad (3.3)$$

We compared the tuning energy efficiency (nm/mW) and P_π with other thermally tunable SiN nano-photonic devices (Table 3.1) and found that our device has the highest tuning efficiency and lowest P_π.

In summary, we experimentally demonstrate a thermally tunable polymer-embedded SiN nanobeam cavity with a tuning efficiency of 44 pm/°C and 0.13 nm/mW in the near-visible wavelength range. The large tuning efficiency comes from the high TO coefficient of the SU-8 polymer and our air-mode cavity design, where a large portion of cavity field is confined inside the polymer. Further higher TO polymer can be used such as Polyurethane (PUR) [110]. Our tunable cavity can potentially have applications in the development of reconfigurable optical device and cavity quantum electrodynamics experiments on the SiN platform.

Table 3.1. Tuning performance for various SiN nanophotonic devices

Device	Energy (nm/mW)	Power P_π (mW)
SiN ring [112]	8.2×10^{-4}	7.7
SiN MZI [113]	NA	30
SU-8-SiN cavity (This work)	0.13	2.7

3.3 Tunable Heterogeneous Photonic molecule

3.3.1 Introduction

Coupled optical microcavities serve as a basic building block for many integrated photonic systems and technologies. Similar to the way in which bound electronic states of individual atoms couple to form those of a molecule, confined photonic excitations of two or more optical cavities can electromagnetically interact to form so-called "photonic molecules". Electronic excitations in molecules are described through hybridization of the orbitals of the constituent atoms and, by analogy, the electromagnetic supermodes of photonic molecules can be constructed by blending the resonances of the individual cavities. While single cavities are instrumental to a diverse set of applications ranging from single-photon generation and strong light-matter coupling to sensing and cavity-controlled chemistry, systems of two or more cavities have shown promise in a number of applications, including low-threshold lasing [113], cavity optomechanics [114], nonclassical light generation [115], quantum simulation [116], and biochemical sensing [117].

Critical to the advantages of photonic molecules over individual cavities is the ability to engineer designer super-modes with properties that differ from those of the constituent components. Of particular interest are coupled cavity structures whose optical properties evolve with tunable parameters such as cavity-cavity separation and detuning. In recent years, the active tuning of such photonic molecules has been demonstrated in several experiments [118,119], but all have thus far focused on coupled structures composed of near-identical individual cavities. While these devices are useful for many applications, homogeneity of the constituent cavities limits the dynamic range of the resulting super-mode properties such as the mode volume, important both for the scaling of light-matter coupling as well as Purcell enhancement.

In contrast, a heterogeneous photonic molecule composed of two distinctly different cavities allows for a richer set of emergent properties with a wider scope of applications, such as improved single photon indistinguishability of quantum emitters [120]. However, lack of a theoretical framework analogous to molecular orbital theory that is capable of elucidating the dependencies of the composite system upon single cavity parameters makes design and analysis of coupled optical cavities difficult. Absent such a formalism, prediction of super-mode field profiles and other downstream properties such as hybridized resonant frequencies and mode volumes must be left to numerical simulation. The latter can be costly for all but the simplest coupled cavities and impossible for many heterogeneous systems, providing impetus for theoretical advances in understanding cavity mode hybridization.

We demonstrated thermally tunable hybridization of optical cavity modes in a heterogeneous photonic molecule composed of a ring resonator and a nanobeam photonic crystal (PhC) cavity. This is achieved by embedding the coupled structure in a high thermo-optic coefficient polymer that preferentially blue-shifts the nanobeam resonance relative to the ring due to the “air-mode” design of the PhC cavity. To better understand the resulting super-modes of this heterogenous optical system, we also introduce a theoretical framework which provides rigorous underpinnings to the more familiar coupled mode theory for hybridized cavity systems and, for the first time, write analytic expressions for the super-mode field profiles and mode volumes. Using this formalism, we demonstrate the ability to extract crucial system parameters such as the bare resonant frequencies and couplings as a function of temperature. Lastly, we use this theory to predict the evolution of the resonant frequencies, field profiles, and hybridized mode volumes of the two super-modes, revealing a temperature-dependent progression which spans a full order of magnitude and results in the coalescence of the two mode volumes near zero detuning.

3.3.2 Experiment

Figure 3.5a displays a scanning-electron-microscope (SEM) image of the heterogeneous coupled-cavity system fabricated on a 220-nm-thick silicon-nitride film, grown on thermal oxide on a silicon substrate. The pattern is defined by e-beam lithography and reactive ion etching. The nanobeam cavity is designed such that a significant portion of the cavity field is concentrated in SU-8 polymer, which both forms a cladding for the entire device and fills the holes of the PhC (Figure 3.5b). In contrast, the ring-resonator mode is predominantly confined within the silicon nitride. Due to the relatively high thermo-optic coefficient of the polymer (approximately $-10^{-4}/^{\circ}C$), which is nearly an order of magnitude larger than that of silicon nitride, heating the entire device leads to a blue shift of the nanobeam-cavity mode relative to that of the ring. As a result, changing the temperature allows for reversible control of the detuning between ring and nanobeam modes. The detuning between the ring and nanobeam modes can therefore be reversibly controlled by changing the temperature. To investigate the effect of ring–nanobeam-mode detuning, the transmission spectrum is measured through the nanobeam PhC cavity for a range of temperatures spanning 33.5°C - 73.5 °C. The spectra are measured using a supercontinuum laser that is coupled to the system via an on-chip grating. The transmitted light is collected through the opposite grating and is sent to the spectrometer. While the gratings already provide a spatial separation to improve the signal-to-noise ratio, a pinhole is used in the confocal microscopy setup to collect light only from the output grating. The temperature of the entire chip is controlled using a hot plate.

Figure 3.5c displays the resulting transmission spectra (gray circles) for a subset of temperatures, Additional spectrums are shown in Figure 3.6. As the cavity modes of the ring and nanobeam are coupled, it is difficult to distinguish how much of the energy separation between transmission peaks at each temperature is due to detuning versus mode splitting resulting from coupling.

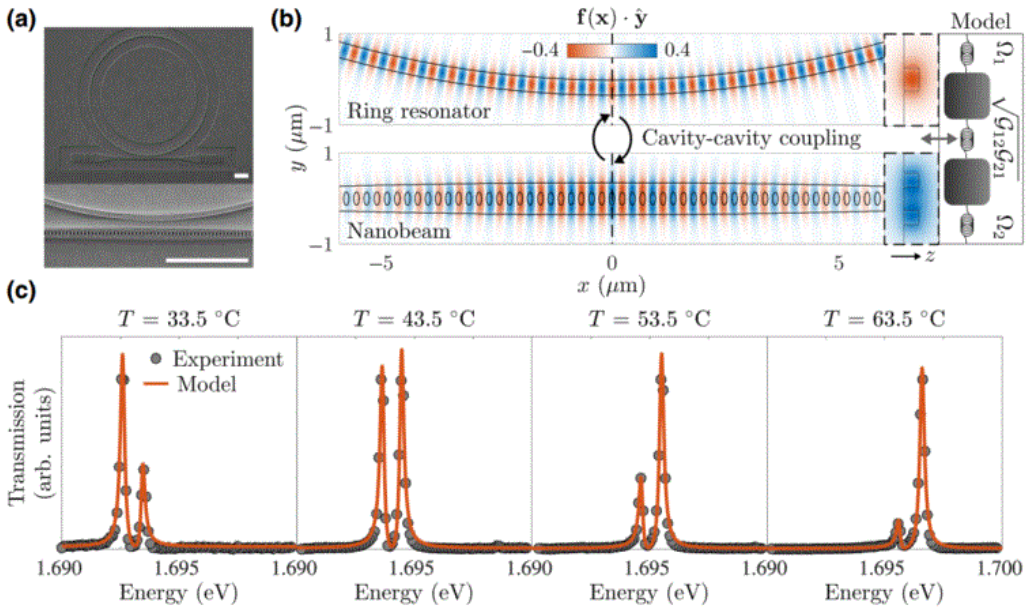

Figure 3.5. Heterogenous photonic molecule. (a) SEM image of the SU-8 cladded, coupled ring resonator-nanobeam device. Scale bars are 5 μm in length. (b) y-component of the electric fields for the nanobeam cavity mode (bottom) and the ring resonator mode (top) most spectrally near. The system is mathematically described with a coupled oscillator model derived from first-principles, parameterized by effective frequencies Ω_i distinct from the bare resonant frequencies ω_i. The coupled modes interact according to an effective coupling strength $\sqrt{\Lambda_{12}\Lambda_{21}}$. (c) Transmission spectra collected for four equally-spaced temperatures (gray circles). Simultaneous least-squares fits to the model are displayed as red lines, indicating terrific agreement with experiment.

Understanding the impact of these individual contributions and analysis of emergent properties requires a theoretical formalism capable of describing the super-modes of the couple ring-nanobeam structure. Coupled mode theory provides one such approach, but typically relies on several phenomenological rates which simplify modeling, often at the expense of over-simplifying the underlying physics. Furthermore, coupled mode theory does not provide a means to predict

super-mode properties of interest for heterogeneous photonic molecules, such as hybridized mode volumes. To amend these deficiencies, we develop a first principles theory that provides analytic understanding of the super-mode resonant frequencies, field profiles, and volumes based only upon knowledge of the individual, uncoupled cavities. The theory is outlined below and used to interpret the measured transmission spectra of the coupled ring resonator-nanobeam device.

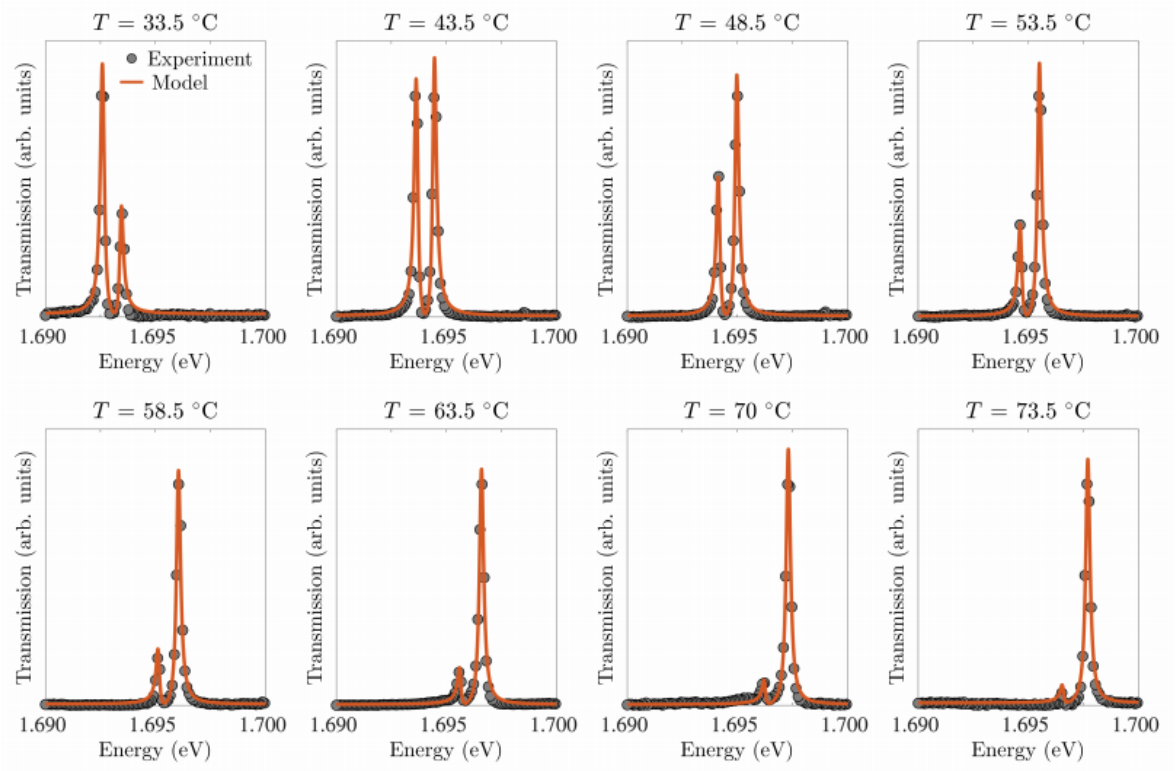

Figure 3.6. Transmission Spectrum at different temperatures.

3.3.3 Theoretical Model

The resonant photonic modes of an optical cavity are given by the independent harmonic solutions of the wave equation

$$\nabla \times \nabla \times \mathbf{A}(\mathbf{x}, t) + \frac{\varepsilon(\mathbf{x})}{c^2} \ddot{\mathbf{A}}(\mathbf{x}, t) = \mathbf{0}, \quad (3.4)$$

where $\mathbf{A}$ is the vector potential related to the cavity fields by the usual relations $\mathbf{E} = -\dot{\mathbf{A}}/c$ and $\mathbf{B} = \nabla \times \mathbf{A}$. As is typical for cavity quantum electrodynamics calculations, we work entirely in the generalized Coulomb gauge defined by $\nabla \cdot \varepsilon(\mathbf{x})\mathbf{A}(\mathbf{x}) = 0$ which leads to $\phi(\mathbf{x}) = 0$ for systems without free charge [121,122], such as the coupled ring-nanobeam device under study. While optical cavities may alternatively be described at the level of the fields themselves, the vector potential accommodates a more natural basis for both a Lagrangian formulation of the cavity dynamics as well as canonical quantization.

Given $\varepsilon(\mathbf{x})$, it is in principle straightforward to numerically solve for the modes of the two-cavity structure in Figure 3.5. Such an approach, however, offers limited predictivity and insight into the interaction between the individual ring resonator and nanobeam modes. In addition, the vastly different length scales of the ring resonator and nanobeam cavity make electromagnetic simulations of the coupled structures computationally challenging, rendering a purely numerical exploration of parameter space infeasible. A more flexible strategy is to numerically solve for the modes of the individual, uncoupled cavities. With the aid of analytics, these individual modes may then be appropriately mixed to form super-modes dependent on basic system parameters such as the spectral detuning and physical separation between the cavities.

Considering just a single cavity mode of both the ring resonator and nanobeam, the vector potential for the double cavity structure can be expanded as

$$\mathbf{A}(\mathbf{x}, t) = \sum_{i=1,2} \frac{\sqrt{4\pi}c}{V_i} q_i(t)\mathbf{f}_i(\mathbf{x}), \quad (3.5)$$

Here, $i = 1,2$ corresponds to the ring and nanobeam, respectively, while $\mathbf{f}_i(\mathbf{x})$ is a mode function of the ith cavity [103] and $q_i(t)$ a time-dependent amplitude [103]. The mode functions are normalized such that the mode volume is given by $V_i = \int d^3x\, \varepsilon_i(\mathbf{x})|\mathbf{E}_i(\mathbf{x})|^2/$

$\max[\varepsilon_i(\mathbf{x})|\mathbf{E}_i(\mathbf{x})|^2] = \int d^3x\, \varepsilon_i(\mathbf{x})|\mathbf{f}_i(\mathbf{x})|^2$. The mode expansion in Equation 3.5 is approximate and, in general, requires additional terms to ensure Gauss's law is obeyed [124,125]. However, these contributions only become physically relevant at inter-cavity separations small enough such that the evanescent field of one cavity "spills" into the dielectric medium composing the nearby second cavity, and therefore can be ignored for ring–nanobeam-resonator studied.

The resonant super-mode frequencies are most easily computed through diagonalization of the equations of motion for the generalized coordinates q_i. This is straightforward using standard techniques of Lagrangian mechanics, but an equivalent route involves directly integrating Equation 3.5. Regardless of the approach, the coupled equations of motion resulting from the expansion are

$$\frac{d^2}{dt^2}\begin{bmatrix} q_1 \\ q_2 \end{bmatrix} = \begin{bmatrix} \Omega_1^2 & \Lambda_{12} \\ \Lambda_{21} & \Omega_2^2 \end{bmatrix}\begin{bmatrix} q_1 \\ q_2 \end{bmatrix}, \quad (3.6)$$

where $\Omega_i^2 = (\bar{\omega}_i^2 - \bar{g}_E\bar{g}_M)/(1 - \bar{g}_E^2/\bar{\omega}_1\bar{\omega}_2)$ and $\Lambda_{ij} = \sqrt{\bar{\omega}_j\bar{V}_i/\bar{\omega}_i\bar{V}_j}\left(\bar{\omega}_i\bar{g}_M - \bar{\omega}_j\bar{g}_E\right)/(1 - \bar{g}_E^2/\bar{\omega}_1\bar{\omega}_2)$ define effective resonant frequencies and couplings parameterizing the oscillator model describing the interaction between the ring and nanobeam cavity modes.

These coupled equations of motion differ in form from those often assumed in application of coupled mode theory to multiple cavity systems [126]. In particular, the diagonal elements of the above coefficient matrix are distinct from the bare resonance frequencies ω_i. This is a consequence of the absence of a weak coupling approximation, resulting in coupling-induced resonance shifts [127] which scale as higher-order products of the three distinct coupling parameters corresponding to the electric (g_E) and magnetic (g_M) inter-cavity couplings, and lastly the polarization-induced intra-cavity self-interaction (Σ_i). The three parameters are defined by:

$$g_E = \sqrt{\omega_1\omega_2/V_1V_2}\int d^3x\, \varepsilon(\mathbf{x})\mathbf{f}_1(\mathbf{x})\cdot\mathbf{f}_2(\mathbf{x}), \quad (3.7)$$

$$g_M = \sqrt{1/\omega_1\omega_2V_1V_2}\int d^3x\, [\omega_1^2\varepsilon_1(\mathbf{x}) + \omega_2^2\varepsilon_2(\mathbf{x})]\mathbf{f}_1(\mathbf{x})\cdot\mathbf{f}_2(\mathbf{x}), \quad (3.8)$$

$$\Sigma_i = \sqrt{1/V_1V_2}\int d^3x\, [\varepsilon(\mathbf{x}) - \varepsilon_i(\mathbf{x})]|\mathbf{f}_i(\mathbf{x})|^2, \quad (3.9)$$

The intra-cavity self-interaction (Σ_i) does not explicitly appear in Equation 3.6, as all inter-cavity couplings, resonant frequencies (ω_i), and mode volumes (V_i) are replaced by renormalized counterparts (indicated by a bar) [103].

While coupled mode theory often reduces cavity-mode interactions to a single coupling parameter independent of the detuning, we note that this is not technically correct, and more rigorous first-principles treatments relying on tight-binding methods [121,122] have revealed three distinct coupling parameters in agreement with those defined above. However, as shown in Equation 3.6, these three parameters may be combined, along with the resonant frequencies, to form effective coupled oscillator equations which account for these subtleties. Notably, all parameters may be computed given only the dielectric function composing the individual cavities along with associated field mode profiles.

3.3.4 Fit to experimental data

Aided by the effective oscillator equations displayed in Equation 3.6, the transmission spectrum is computed through standard input-output methods [123,130], yielding

$$\mathcal{T}(\omega) = \left|\frac{\kappa}{\omega-\Omega_1+i\kappa+\frac{\Lambda_{12}\Lambda_{21}/4\Omega_1\Omega_2}{\omega-\Omega_2}}\right|^2, \quad (3.10)$$

Simultaneous least-squares fits are performed to transmission spectra at the eight experimentally probed temperatures shown in Figure 3.5c and Figure 3.6. To minimize the number of free

parameters, Σ_1, Σ_2, V_1 and V_2 are calculated using the theory, supplemented by numerically calculated single cavity field profiles. Similarly, g_E and g_M are constrained to within $\pm 1\%$ of their theoretical values, while the waveguide-induced dissipation rate κ is estimated from electromagnetic simulation of the nanobeam.

The remaining free parameters, all displayed in the top row of Table 3.2, are extracted through a simultaneous least-squares fit to all measured transmission spectra. Among them is the resonant frequency of both the ring resonator and nanobeam at room temperature T_0 and associated intrinsic dissipation rates, the latter of which may be introduced via input-output theory in the standard way by generalizing Ω_1 and Ω_2 to be complex-valued [131]. We find that the temperature dependence of the resonant wavelength of each cavity is well-approximated as linear. All other parameters are assumed to depend negligibly upon temperature and are treated as constant. Even with these simplifying approximations, agreement between experiment (circles) and theory (solid lines) are excellent, as evident in Fig 3.5c.

Table 3.2. Parameter estimates

$\hbar\omega_1(T_0)$	$\hbar\omega_2(T_0)$	$d\lambda_1/dT$	$d\lambda_2/dT$	$\hbar\gamma_1$	$\hbar\gamma_2$	
1.6922 eV	1.6918 eV	-39 pm/°nC	-50 pm/°nC	0.16 meV	0.23 meV	
V_1	V_2	κ	$\hbar g_E$	$\hbar g_M$	Σ_1	Σ_2
5.0 μm^3	0.49 μm^3	9.7 μeV	-16.4 meV	-15.6 meV	1.1×10^{-5}	8.5×10^{-5}

Figure 3.7a displays the full set of transmission measurements (circles) and fits (curves) for all eight probed temperatures, while Figure 3.7b shows the super-mode resonant frequencies ($\omega_\pm$) as

a function of energy detuning $\hbar\omega_2 - \hbar\omega_1$. For each temperature measured, resonant frequencies are estimated from the peaks in transmission spectra and are shown as black circles. Theory curves (red and blue) are computed through diagonalization of the effective oscillator model in Equation 3.6 which we parameterize according to Table 3.2. Because both ring and nanobeam modes blue-shift with increasing temperature, plotted curves and points are shifted with respect to the average resonant energy $\bar{\omega} = (\omega_+ + \omega_-)/2$ for both panels.

The resonant frequencies undergo a clear anticrossing as the system nears zero detuning around $T = 40$ °C, with upper and lower cavity polariton energies differing by roughly 0.8 meV. Because the coupled oscillator model is parameterized by the effective frequencies Ω_1 and Ω_2, and not the bare cavity resonances ω_1 and ω_2, the anticrossing occurs where the former, and not the latter, are co-resonant. Thus, the anticrossing in Figure 3.6 is slightly shifted from zero detuning. In addition, the super-mode resonances $\omega_\pm$ tend towards the effective frequencies (dotted lines) at large positive and negative values of the detuning.

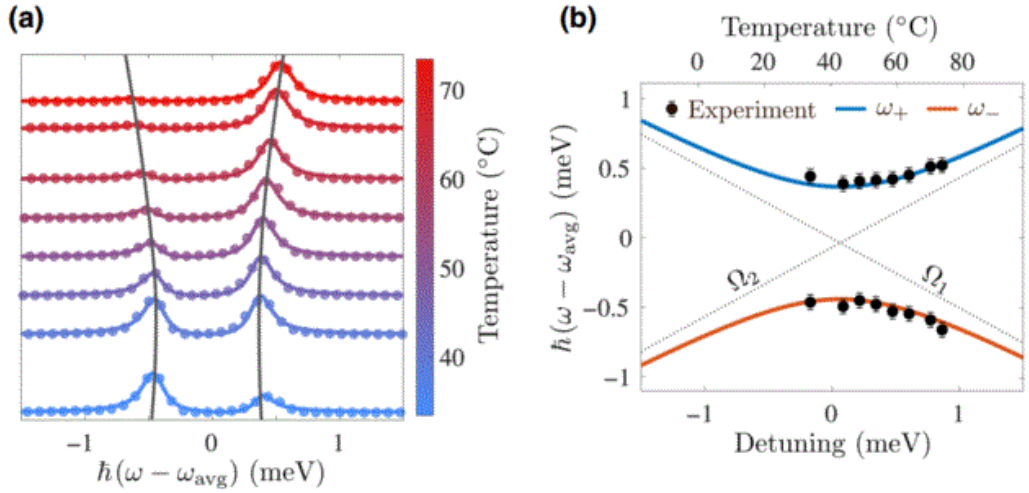

Figure 3.7. Fitting to experimental data. (a) Anticrossing resulting from strong coupling between the ring-resonator and nanobeam-cavity modes. Experimental data are shown as circles, while

colored solid lines display the resulting least-squares fit to Eq. (3.10). The gray lines overlie the theoretical values of ω±, extrapolated via parameter values obtained from the fits. (b) The evolution of the supermode resonant frequencies as a function of the detuning. The black points correspond to experimentally measured peak transmission energies, while the error bars indicate the uncertainty in the peak energy due to the finite density of the transmission energies measured. The solid curves display the theoretical supermode energies computed from Eq. (3.6), parametrized through simultaneous fits to transmission measurements.

Strong coupling is confirmed quantitatively through comparison of the computed effective coupling strength with the dissipation rates reported in Table 3.2. In particular, we find that $\left|\hbar\sqrt{\Lambda_{12}\Lambda_{21}/4\Omega_1\Omega_2}\right| \approx 0.40$ meV, nearly double the dominant intrinsic dissipation rate $\hbar\gamma_1 = 0.23$ meV.

3.3.5 Analysis of supermode properties

Hybridization is further investigated through inspection of the super-mode profiles

$$\begin{aligned}\mathbf{f}_{\mp}(\mathbf{x}) &= \frac{1}{A(\theta)}\left[\left(\frac{\Lambda_{12}}{\Lambda_{21}}\right)^{1/4}\sqrt{\frac{V_2}{V_1}}\mathbf{f}_1(\mathbf{x})\cos\theta - \left(\frac{\Lambda_{21}}{\Lambda_{12}}\right)^{1/4}\sqrt{\frac{V_1}{V_2}}\mathbf{f}_2(\mathbf{x})\sin\theta\right] \\ \mathbf{f}_{\pm}(\mathbf{x}) &= \frac{1}{B(\theta)}\left[\left(\frac{\Lambda_{21}}{\Lambda_{12}}\right)^{1/4}\sqrt{\frac{V_1}{V_2}}\mathbf{f}_2(\mathbf{x})\cos\theta + \left(\frac{\Lambda_{12}}{\Lambda_{21}}\right)^{1/4}\sqrt{\frac{V_2}{V_1}}\mathbf{f}_1(\mathbf{x})\sin\theta\right]\end{aligned}, \quad (3.11)$$

and their associated mode volumes

$$\begin{aligned}V_{\mp} &= V_1\left[\frac{V_2}{V_1}\sqrt{\frac{\Lambda_{12}}{\Lambda_{21}}}\frac{1+\Sigma_1}{A(\theta)^2}\right]\cos^2\theta + V_2\left[\frac{V_1}{V_2}\sqrt{\frac{\Lambda_{21}}{\Lambda_{12}}}\frac{1+\Sigma_2}{A(\theta)^2}\right]\sin^2\theta - \sqrt{V_1V_2}\left[\frac{g_E/\sqrt{\omega_1\omega_2}}{A(\theta)^2}\right]\sin 2\theta \\ V_{\pm} &= V_2\left[\frac{V_1}{V_2}\sqrt{\frac{\Lambda_{21}}{\Lambda_{12}}}\frac{1+\Sigma_2}{B(\theta)^2}\right]\cos^2\theta + V_1\left[\frac{V_2}{V_1}\sqrt{\frac{\Lambda_{12}}{\Lambda_{21}}}\frac{1+\Sigma_1}{B(\theta)^2}\right]\sin^2\theta + \sqrt{V_1V_2}\left[\frac{g_E/\sqrt{\omega_1\omega_2}}{B(\theta)^2}\right]\sin 2\theta\end{aligned}, \quad (3.12)$$

where $A(\theta)$ and $B(\theta)$ are normalization factors [103], $\theta = (1/2)\tan^{-1}\left(2\sqrt{\Lambda_{12}\Lambda_{21}}/[\Omega_2^2 - \Omega_1^2]\right)$ is the mixing angle, and the upper (lower) subscript corresponds to the case $\theta > 0$ ($\theta < 0$). The mixing angle has two distinct regimes; when the detuning is much larger than the effective coupling strength ($\theta \to 0$), the above mode functions reduce to those of the bare ring resonator and

nanobeam cavity. In contrast, for small detuning relative to the coupling ($\theta \to \pm\pi/4$) the mode functions become a superposition of $\mathbf{f}_1(\mathbf{x})$ and $\mathbf{f}_2(\mathbf{x})$.

Figure 3.8a shows the evolution of the y component of the upper- (top) and lower- (bottom) cavity-polariton field profiles across the experimentally measured temperature range. Because the limits of this range constrain the mixing angle to $-\pi/8 \lesssim \theta \lesssim \pi/6$, neither $\mathbf{f}_+(\mathbf{x})$ nor $\mathbf{f}_-(\mathbf{x})$ entirely localize to one of the constituent cavities at any probed temperature. For all mode profiles shown, a significant portion of the field is contributed by the mode function of the nanobeam $\mathbf{f}_2(\mathbf{x})$. We note, however, that there is no fundamental reason that the device could not be heated past the maximum temperature studied here (73 °C), or alternatively cooled to below room temperature.

Notably, the super-mode profiles are not equal superpositions of $\mathbf{f}_1(\mathbf{x})$ and $\mathbf{f}_2(\mathbf{x})$ near zero detuning ($T = 40$ °C). This may be understood by considering the large mismatch in mode volume between the ring resonator and nanobeam modes ($V_1/V_2 \sim 10$). According to Equation 3.11, the nanobeam contribution to both $\mathbf{f}_+(\mathbf{x})$ and $\mathbf{f}_-(\mathbf{x})$ scales like $(V_1/V_2)^{1/4}$, while that of the ring resonator scales like $(V_2/V_1)^{1/4}$. As a result, both super-modes are predominantly localized to the nanobeam. Due to this effect, the mode volume of each super-mode is thermally tunable over a large range of values.

Figure 3.8b shows theoretical predictions for the hybridized mode volumes as a function of temperature-controlled detuning, calculated using Equation 3.12 paired with the experimentally informed parameter values in Table 3.2. As before, blue and red curves correspond to the upper and lower cavity polaritons in Figure 3.8a, respectively. The gray region indicates the range of experimentally probed temperatures. As expected, both hybridized mode volumes tend towards those of the individual cavities at large positive and negative detuning. The two mode volumes

coalesce at a value of $V_{\pm} \approx 0.95\ \mu\text{m}^3$, more than a factor of 5 less than the mode volume of the isolated ring resonator.

While the nanobeam mode volume V_2 clearly serves as a lower bound for $V_{\pm}$, analysis of Equation 3.12 indicates a maximum near $V_1 + V_2$. V_+ slightly exceeds this value due to constructive interference between the two modes, while V_- peaks at a value below $V_1 + V_2$ due to destructive interference. Both mode volumes display a "turning point" at values of the mixing angle θ such that $\mathbf{f}_1(\mathbf{x})$ and $\mathbf{f}_2(\mathbf{x})$ are equally-weighted in either $\mathbf{f}_+(\mathbf{x})$ or $\mathbf{f}_-(\mathbf{x})$. Between these two points is a full order-of-magnitude of attainable values for both hybridized mode volumes, illustrating the terrific potential of this heterogeneous device for temperature-tunable photonic properties.

In conclusion, we have demonstrated thermally tunable mode-mixing in a heterogeneous photonic molecule consisting of a ring resonator coupled to a photonic crystal cavity. Aided by a theoretical formalism developed to study hybridized cavity states in photonic molecules, we show the capability to extract system parameters, resulting in a predictive effective oscillator model distinct from those typically assumed by coupled mode theory. We leverage this model to predict important properties of the super-modes, such as resonant frequencies, field profiles, and mode volumes, all as a function of temperature. Lastly, we show that this heterogeneous device in principle allows for temperature tunable hybridized mode volumes which span a full order of magnitude, showing the tremendous potential for coupled cavity systems with temperature-tunable, designer properties.

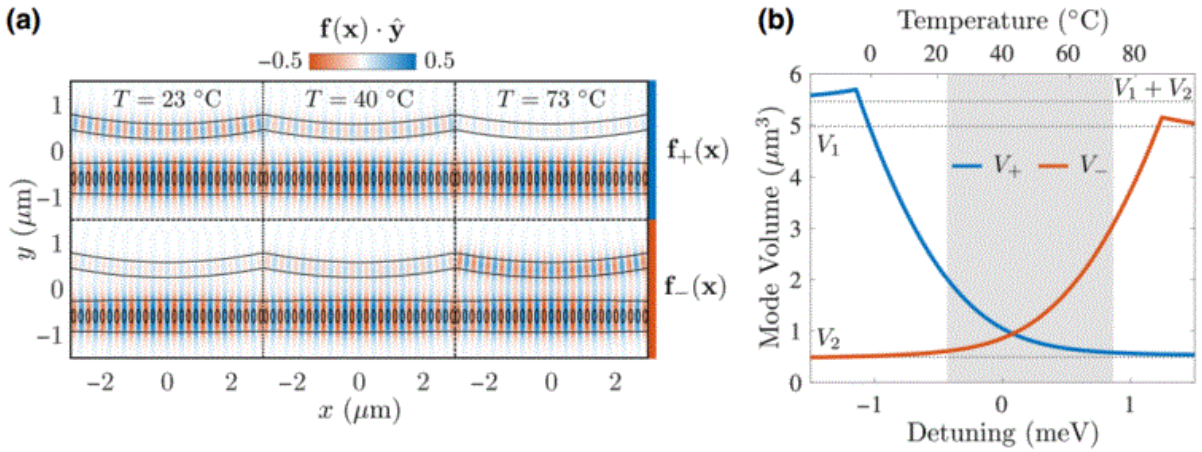

Figure 3.8. Hybrid mode volume. (a) The field profile for the upper- (top) and lower- (bottom) cavity polaritons at various temperatures. Both supermodes are dominated by the nanobeam field at all observed temperatures due to the weighting of $f_1(x)$ and $f_2(x)$ in Eq. (3.11). (b) The hybridized mode volumes V_+ (blue curve) and V_- (red curve) of the upper- and lower-cavity polaritons. The gray region indicates the range of experimentally measured temperatures, while the dotted lines specify V_1, V_2, and $V_1 + V_2$. Due to the predominant localization of both modes in the nanobeam cavity, both V_+ and V_- coalesce at a value less than 5 times the mode volume of the isolated ring-resonator mode.

Chapter 4 Monolayer Exciton-Polariton with SiN metasurface

4.1 Introduction

Monolayer transition metal dichalcogenides (TMDs) have generated active research interest in recent years due to their strong light-matter interaction and unique optoelectronic properties [132]. Thanks to the quantum confinement in the atomic layer, exciton with large binding energy can form in monolayer TMD at room temperature, exhibiting strong excitonic absorption and photoluminescence [34]. The strong excitonic response could be further enhanced by coupling the TMD monolayer to an optical cavity [74]. In the weak coupling regime, low-threshold nano-laser [17,40,133,134] and cavity-enhanced light-emitting diodes [32] have been demonstrated using TMD monolayer. In the strong coupling regime, TMD exciton-polaritons (EPs) have also been observed at room temperature [33,135,136]. EPs, the hybrid light-matter quasi-particles, inherit the low effective mass from their photonic component and large nonlinear interaction strength form their excitonic component, making them a promising platform to study Bose–Einstein condensate [137], with far-reaching impact on quantum simulation with interacting photons [79]. TMD EP also has potential applications in low-power nonlinear optics [138] and polariton laser [139]. Furthermore, the TMD EP inherits the unique spin-valley physics from its exciton part [140], and the optical valley hall effect of the TMD EP could be explored in this hybrid light-matter system [141].

So far, most TMD-based EP devices are based on distributed Bragg reflector (DBR) cavity [33,142,143]. The fabrication process of the DBR-sandwiched TMD platform is non-trivial since the encapsulation of the upper DBR layers often degrade the optical property of the monolayer TMD [144]. Open cavity structures such as fiber-cavity and single DBR structure have

been explored [145,146] to solve the problem of material degradation. However, in such platforms, it is difficult to engineer the mode or dispersion of the cavity, a capability which can have far-reaching impact in the field of exciton-polaritonics. Plasmonic cavity is considered as a promising candidate [147–149], but it suffers from metallic loss. Another promising platform will be sub-wavelength patterned surfaces, also known as dielectric metasurfaces [150]. These metasurfaces can shape the optical wavefront using the sub-wavelength scatterers, also known as meta-atoms, and have recently been used to drastically miniaturize imaging and sensing devices [151–153], as well as to enhance light-matter interaction [154,155]. This nanopatterned, periodic photonic lattice supports a rich cluster of optical Bloch mode and can tightly confine the electromagnetic field [156,157]. Moreover, computational design and dispersion engineering of the meta-atoms allow unprecedented nanophotonic engineering [158–160]. Going beyond passive metasurfaces, researchers are now exploring new materials to create active metasurfaces [161,162]. In fact, nonlinear frequency conversion has been reported with GaSe integrated silicon metasurface [163]. EP has also been demonstrated on a TMD-clad one-dimensional (1D) grating structure [164]. Signature of optical nonlinearity has recently been reported in TMD-coupled 1D bound state in continuum resonator [165]. However, extending the periodicity in two dimensions (2D) is desirable. The extra degrees of freedoms in a 2D metasurface would allow advanced dispersion engineering, providing new opportunity to merge the EP with novel photonic designs, such as topological structures, most of which are demonstrated in two dimensions [166–169]. Subwavelength mode engineering of 2D metasurfaces could also result in localized optical field to further enhance the light-matter interaction [170,171]. Finally, the intrinsic isotropic nature of the periodic 2D structure would favor the study of monolayer valley-polaritons [141,142]. While

coupling between TMD excitons and 2D periodic structure has been explored, to date only the weak-coupling regime is reported [172,173].

In this Chapter, we demonstrated EPs in atomically thin tungsten diselenide (WSe_2) strongly coupled to the guided mode resonances (GMR) in a silicon nitride (SiN) metasurface. The GMR simultaneously achieves strong confinement of photons inside the metasurface and efficient coupling with the radiation continuum. By performing energy-momentum spectroscopy on the WSe_2-SiN metasurface, we measured the anti-crossing of the polariton dispersion both in the cavity reflection and photoluminescence. The EP dispersion measured in the experiment is also reproduced by our numerical simulation. Moreover, we showed that the Rabi splitting, the polariton dispersion and the far-field emission pattern could be tailored by subwavelength-scale engineering of the meta-atoms. Our platform opens the door for the future development of novel EP devices by advanced meta-optical engineering.

4.2 Guided mode resonances in silicon nitride metasurface

Figure 4.1a shows the schematic of our platform. The metasurface is made of SiN with square lattice of holes. The whole structure sits on a silicon dioxide substrate. A WSe_2 monolayer is transferred directly on top of the metasurface for evanescent coupling. Such periodic 2D photonic lattice supports many optical Bloch modes propagating inside the slab. These modes can be classified into two classes [36]: in-plane guided modes and guided mode resonance (GMR). The GMRs couple with the radiation continuum and in the meantime, confine part of their electromagnetic power inside the slab. When a light beam shines on the metasurface, the interference between the slab mode and the GMR modes result in a Fano lineshape in the reflection

spectrum. These Fano resonances have been used in the past for dispersion engineering [174], spectral filtering [175], and enhancing the light-matter interaction [163,176].

We simulated the reflection spectrum of the GMR in the SiN metasurface through Rigorous coupled-wave analysis (RCWA) [177,178]. We use the S4 simulation package developed by Stanford University. For the SiN metasurface, a unit cell is simulated. The square lattice has a period of 459nm and a hole diameter of 120nm. The metasurface has a thickness of 130nm and it sits on a 1μm thermal oxide layer grown on 500 μm silicon substrate. The sub-wavelength thickness guarantees more electrical field on the meta-atom's surface leading to a larger light-matter interaction since the WSe_2 monolayer would be evanescently coupled to the GMR via the surface field. The SiN slab is set with a refractive index of 2. The silicon oxide is set with a refractive index of 1.5. The index of silicon is set with a refractive index of 3.76 + 0.01i. A plane wave light source with p polarization incidents from the top of the unit cell, while the incident angle is adjusted for each value. The conversion between the angel and the k_x follows: $k_x = \frac{2\pi}{\lambda}\sin(\theta)$. Here λ is the wavelength and θ is the angle of the incident beam. The reflection amplitude is normalized to the source amplitude.

Figure 4.1b (left panel) shows the angle-dependent reflection spectrum along the k_x direction for p-polarized incident light. There are two GMRs: M1 has a linear dispersion and M2 has a parabolic shape. M1 starts at higher energy and goes to lower energy with higher momentum, whereas M2 starts at lower energy and goes to higher energy. Two modes come close at $k_x = 0.6\ \mu m^{-1}$, and anti-cross due to the coupling between them. The electric field distribution of two modes at $k_x = 0$ is shown in Figure 4.1c. Two modes have different symmetry in terms of the field distribution, but both are well confined inside the metasurface. We note that our metasurface acts as a cavity that

stores photons and achieves field enhancement inside the slab in the vertical direction, although it does not have confinement along the in-plane directions.

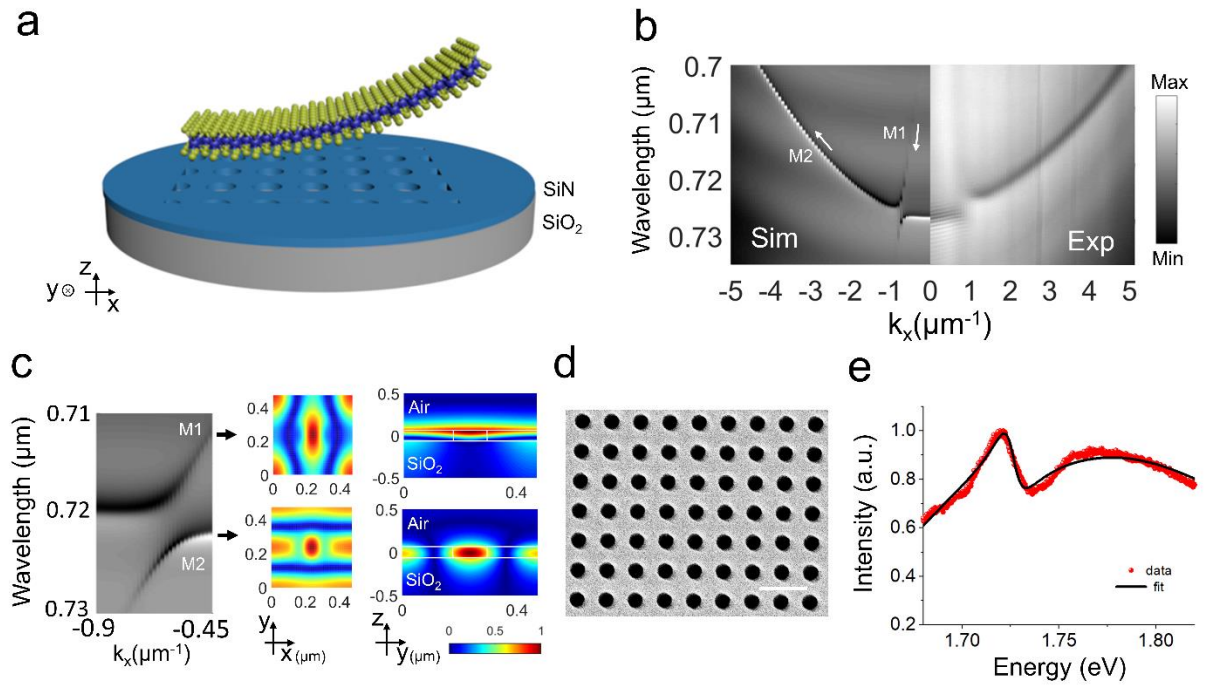

Figure 4.1. SiN metasurface supporting guided mode resonances. (a) The metasurface is made of SiN meta-atoms with holes arranged in a square lattice. The whole structure sits on a silicon dioxide substrate. A WSe_2 monolayer could be transferred directly on top of the metasurface for evanescent coupling. (b) Simulated vs Experimentally measured angle-dependent reflection spectrum. There are two modes (M1 and M2) in the spectrum. M1 has a linear dispersion and starts at higher energy and rapidly goes to lower energy when it comes to high momentum. M2 has a parabolic shape and it starts at lower energy and goes to the higher energy. The two modes come close to each other at $k_x = 0.6\ \mu m^{-1}$: an anti-crossing appears due to the coupling between the two photonics modes. (c) Zoom-in of the anti-crossing and the mode profiles of M1 and M2. Two modes have different symmetry in terms of the field distribution, but they are both well confined inside the metasurface. (d) The SEM of the SiN metasurface (scale bar: 1 μm) (e) Example spectrum and fitting at $k_x = 2.2\ \mu m^{-1}$. A Fano-lineshape is observed with a Q factor ~143 and asymmetry factor -1.4.

We then fabricated the metasurface and performed energy-momentum spectroscopy at room temperature to measure the angle-dependent reflectivity spectrum. The SEM of the fabricated device is shown in the Figure 4.1d. As shown in Figure 4.1b, the experiment result matches well with the simulation at the left side, with the mode-splitting observed at k_x = 0.6 μm^{-1}. The mismatch between the theory and simulation of the dispersion at high momentum can be attributed to the spherical aberration of the lenses in the optical setup. The fact that a clear photonic dispersion is measured in the momentum space clearly confirmed that we are measuring the radiative GMR mode instead of the scattering light from in-plane guided mode, since the scattering light from the in-plane guided mode would only have a random intensity distribution in the momentum space.

We then fit the reflection spectrum $R(\omega)$ at each k_x value through a functional form [164]:

$$R(\omega) = R_{Fano} + R_{FP} + R_b, \text{ (4.1)}$$

Here, R_{Fano} is the Fano lineshape resulting from the interference of the GMR and the SiN slab mode:

$$R_{Fano} = I_0\left(1 - \frac{(x+q)^2}{x^2+1}\right), \text{ (4.2)}$$

$$x = \frac{E-E_0}{\Delta\omega/2}, \text{ (4.3)}$$

Here, I_0 is the amplitude coefficient of the Fano resonance, q is the asymmetry factor, $E = \hbar\omega$ is the photon energy at angular frequency of ω, and $E_0 = \hbar\omega_o$ is the photon energy at the cavity resonance frequency ω_o, $\Delta\omega$ is the Full width at half maximum (FWHM). Since both E_0 and $\Delta\omega$ are in units of eV, x becomes a unitless quantity. R_{FP} is a broad Fabry-Perot (FP) interference background resulting from the reflection between the SiN/SiO_2 interface and the SiO_2/Si interface. We calculate R_{FP} through the transfer matrix method [164] for the multiple thin film structure (SiN/SiO_2/Si). R_b represents an ambient background in the fit. Figure 1e shows an example fit for

the reflection spectrum at k_x = 2.2 μm^{-1}. Through the fit, the resonance energy E_0 is extracted as 1.726 eV, the resonance Q factor as ~143 ($\Delta\omega$ = 12 meV) and q = -1.3.

4.3 Exciton-polaritons in hybrid WSe_2-metasurface structure

4.3.1 Simulation and theory

For the WSe_2-SiN metasurface, we added a monolayer of WSe_2 (thickness = 0.7nm) on top of the SiN meta-atom to simulate the reflection/absorption spectrum of our WSe_2-metasurface structure in RCWA simulation. The dielectric function of the monolayer of WSe_2 is described by a Lorentz model:

$$\varepsilon(E) = \varepsilon_B + \frac{f}{{E_x}^2 - E^2 - i\Gamma E}, \quad (4.4)$$

The ε_B is the background dielectric constant, f is the oscillator strength, Γ is the linewidth of the exciton, and E (E_x) represents the photon (exciton resonance) energy. For WSe_2, the value of ε_B is 25 and f is 0.7 eV^2 [164], and we use the value of E_x and Γ from our fitting data of the monolayer (E_x = 1.728 eV and Γ = 2 × γ_{exc} = 12.2 meV). The simulation results are shown in the left panels of Figure 4.3b and Figure 4.3f.

The radiation-matter coupling of the ultra-thin semiconductor layer coupled to the guided resonances of the SiN metasurface can also be theoretically calculated by treating the photonic nanostructure as a two-dimensional periodic slab and the active material as a quantum well characterized by an oscillator strength per unit surface. In this respect, the theoretical framework is the one thoroughly discussed in Ref. [179], where a quantum theory of exciton-photon coupling is formulated in terms of the guided mode expansion reported in Ref. [180]. The latter has been

successfully applied to different context and material platforms involving coupling of strongly radiation coupled layered media to patterned metasufaces, see, e.g., Refs. [155,181]. Here we also apply this theory to the coupling of a 2D TMD with a GMR, showing its intrinsic versatility and generality.

Briefly, at each Bloch wave vector of the periodic lattice established from the patterned metasurface we calculate the exciton-photon coupling matrix element as [180]

$$g_k = \hbar\sqrt{\frac{\pi e^2}{m_0}\frac{f}{S}}\int dx\, dy\, E_k(x, y, z_{QW})F(x, y), \quad (4.5)$$

where f/S is the oscillator strength per unit surface of the allowed excitonic dipole transition (which from the value f_x=0.7 eV^2 the WSe_2 monolayer can be estimated as $7 \times 10^{13}\ cm^{-2}$), and it is the only input parameter of our calculation, together with the exciton resonance and linewidth (E_{exc} and $G_{exc}=2g_{exc}$, respectively). In the expression above, $E(x,y)$ is the normalized in-plane component of the electric field calculated at the vertical position corresponding to the 2D TMD, z_{QW}, and at the wave vector k, while $F(x,y)$ is the 2D exciton envelope [179]. This coupling matrix element is then used to formulate a Hopfield matrix, which can be numerically diagonalized at each k-vector to give the full polariton dispersion. In Fig. 4.2 we report the calculated dispersion of the dressed modes when the nominal metasurface slab parameters are assumed (as given in the caption for completeness), and the 2D TMD layer is placed exactly at the upper surface of the SiN film. The result shows remarkly good agreement with the RCWA simulation. The exciton photon coupling is calculated to be g~11.5 meV, which corresponds to a Rabi splitting of $\hbar\Omega_{Rabi}$~2g~23 meV. The values would be used to compared to the experimental data extracted in the following section.

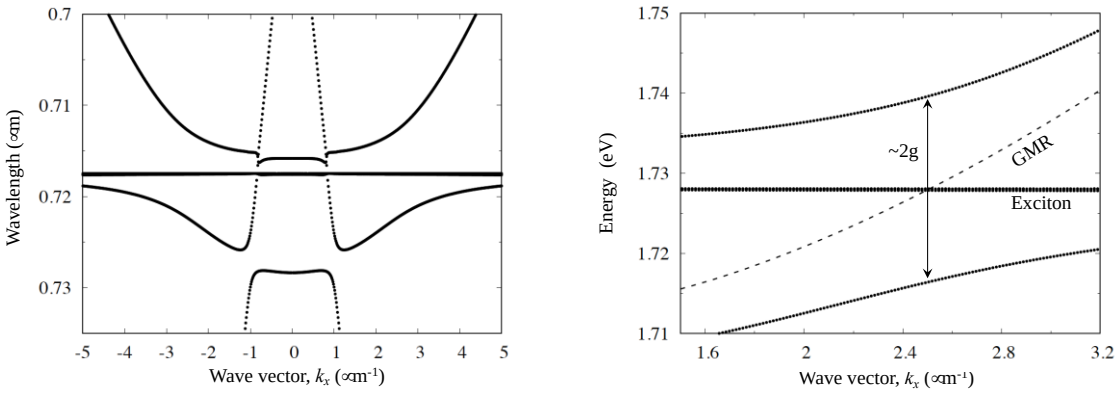

Figure 4.2. Calculated polariton dispersion, i.e. wavelength (left panel) and energy (right panel) as a function of horizontal wavevector, as obtained from the diagonalization of the Hopfield matrix. The guided-mode solutions are obtained for the following parameters of the SiN metasurface slab: a=459 nm, r=60 nm, d=130 nm, e_{SiN}=4.25, e_{ox}=2.11. The 2D TMD is placed exactly on top of the patterned slab, with an exciton resonance at E_{exc}=1.728 eV, linewidth G_{exc}=12 meV, and an oscillator strength per unit surface $f/S = 7 \times 10^{13}\text{cm}^{-2}$. Loss rates of GMR are calculated in guided-mode expansion through perturbative coupling with radiative modes of the SiN slab with an effective refractive index taking into account hole patterning.

4.3.2 Experiment

We transferred a hBN encapsulated WSe_2 monolayer on top following usual dry transfer process [70]. The hBN encapsulation improves the surface smoothness of the WSe_2 and preserves the intrinsic narrow linewidth of the WSe_2 [182]. We then performed the energy-momentum spectroscopy on the WSe_2-SiN metasurface structure at 22K. As shown in Figure 4.3b, the GMR dispersion changed dramatically when coupled with WSe_2 at the exciton wavelength (~715nm). A clear anti-crossing is observed in the range from k_x = 1.5 μm^{-1} to k_x = 3 μm^{-1}. We fit the dispersion spectrum at each k_x value with the Fano-lineshape function to extract the resonance wavelengths of the upper and lower polaritons. An example fit spectrum at k_x = 2.4 μm^{-1} is shown in Figure 4.2c, where two Fano lineshapes appear, corresponding to the upper polariton (UP) and

lower polariton (LP). We note that, this spectrum is dramatically different from Figure 1e where only one Fano resonance is measured as the cavity resonance. For the spectrum shown in Figure 4.2c (at k_x = 2.4 μm^{-1}), the resonance energy for the UP and LP is found as 1.718 eV and 1.74 eV, respectively from the fitting parameters.

Once the spectrum for each k-vector is fit and the wavelengths of the UPs and LPs are extracted, we estimate the loss and the interaction strength of the coupled system. We use a dispersive coupled-oscillator model to fit the wavelength of the LPB and UPB [137].

$$\begin{pmatrix} E_{exc} + i\gamma_{exc} & g \\ g & E_{cav} + i\gamma_{cav} \end{pmatrix} \begin{pmatrix} \alpha \\ \beta \end{pmatrix} = E_p \begin{pmatrix} \alpha \\ \beta \end{pmatrix}, \quad (4.6)$$

Here E_{exc} is the energy of the bare exciton and γ_{exc} is its decay rate. E_{cavity} is the energy of the bare cavity and γ_{cav} is the cavity decay rate, g is the coupling strength between the exciton and the cavity, E_p represents the eigenvalues corresponding to the energies of the polariton modes, and it could be found as:

$$E_{LP,UP} = \frac{1}{2}\left[E_{exc} + E_{cav} + i(\gamma_{cav} + \gamma_{exc})\right] \pm \sqrt{g^2 + \frac{1}{4}\left[E_{exc} - E_{cav} + i(\gamma_{exc} - \gamma_{cav})\right]^2}, \quad (4.7)$$

α and β construct the eigenvectors and represent the weighting coefficients of the cavity photon and exciton for each polariton state, where $|\alpha|^2 + |\beta|^2 = 1$. The Hopfield coefficients which indicate the exciton and photon fraction in each LP and UP are given by the amplitude squared of the coefficients of eigenvectors ($|\alpha|^2$ and $|\beta|^2$).

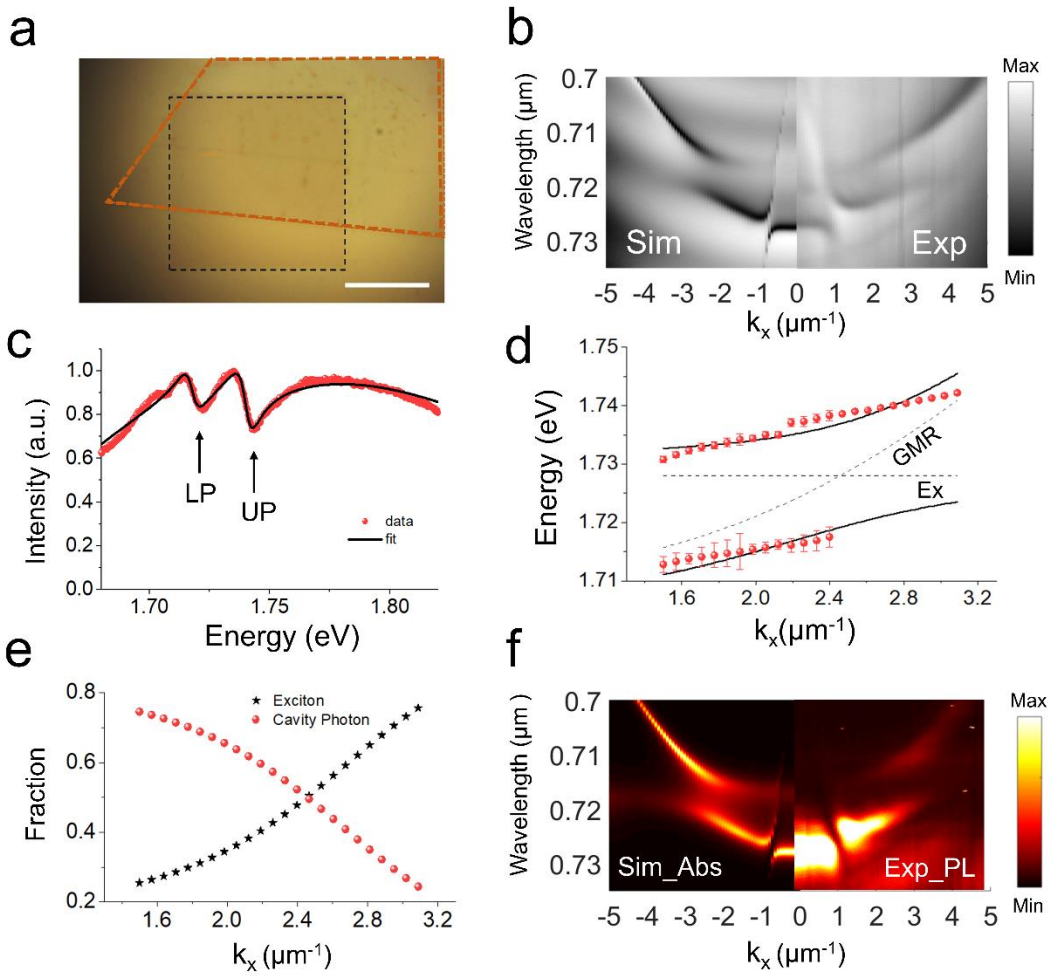

Figure 4.3. Monolayer exciton-polariton. (a) The optical microscope image of the SiN metasurface with hBN-capped WSe_2 transferred (scale bar: 20 μm). The black lines outline the metasurface and the orange lines outline the monolayer WSe_2. The hBN is hardly observed under the microscope due to poor optical interference. (b) Simulated vs experimentally measured angle-dependent reflection spectrum. Anti-crossing is observed at $k_x \sim 2.4\ \mu m^{-1}$. (c) Example of a fit reflection spectrum at $k_x = 2.4\ \mu m^{-1}$, the Fano-resonance of the lower polariton (LP) and upper polariton (UP) are observed. (d) Fitting for the anti-crossing: a Rabi splitting value of the 18 meV is extracted. (e) Hopfield coefficients of the LP branch, which show the exciton and photon fraction in the polariton. (f) PL emission also shows the anti-crossing: LPB emission is brighter than UPB due to the thermal equilibrium condition.

Since we measured E_{cavity} before the transfer of WSe_2 and $E_{LP,UP}$ after the transfer, the independent parameters in our fit are γ_{exc}, E_{exc} , g and γ_{cav}. During fitting, we shifted the cavity resonance (E_{cavity}) to account for the effect of the hBN and temperature-dependence of the cavity resonance. Through the fitting, we extracted $E_{exc} = 1.728eV$, $\gamma_{exc} = 6.1\, meV$, γ_{cav} = $8.3\, meV$ and g $= 9.1\, meV$. We also calculated the Rabi splitting $\hbar\Omega_{Rabi}$ = $2\sqrt{g^2 - \frac{1}{4}(\gamma_{exc} - \gamma_{cav})^2}$ = $18\, meV$. This value is of the similar magnitude of the values reported using one-dimensional photonic lattice [164,165]. The value is also in remarkably good agreement with the theoretical calculation shown in the above section.

We then compared the dissipation rate with the interaction strength to confirm that we are indeed in the strong-coupling regime. The conditions to reach strong coupling are:

$$g > |\gamma_{exc} - \gamma_{cav}|/2 \text{ and } g > \sqrt{(\gamma_{exc}^2 + \gamma_{cav}^2)/2}, \quad (4.8)$$

Clearly, the extracted parameters ($\gamma_{exc} = 6.1\ meV$, γ_{cav} = $8.3\, meV$ and g $= 9.1\, meV$) satisfy above two criteria. We also measured photoluminescence (PL) and observed the anti-crossing in PL (Figure 4.3b). The PL is brighter at LPB than UPB as expected from the thermal equilibrium condition [183]. We then calculated the angle-dependent Hopfield coefficient (α and β) from the coupled-oscillator model (Equation 4.6). Figure 4.3e shows the Hopfield coefficients of the LPB. The LPB is more photon-like for $k_x < 2.4\ \mu m^{-1}$ and more excitonic-like for $k_x > 2.4\ \mu m^{-1}$.

The nano-patterned subwavelength structure can also produce a directional polariton emission in the far-field. Here we focus on the emission from the lower polariton since it is significantly brighter than the upper polariton. A 720 nm long-pass filter is placed at the collection path to block the signal from the pumping beam and the upper polariton. Figure 4.4a shows the back focal plane image of the spatial distribution of the collected signal. Different from the emission pattern of an

in-plane exciton on an unpatterned substrate [184], the polariton emission shows a unique pattern: The metasurface diffracts the PL signal directionally along k_x and k_y axis. We also simulate the diffraction pattern in FDTD simulation (Figure 4.4b). The circumference of each figure represents the numerical aperture of the objective lens in the momentum space (NA = 0.6). We observe qualitative agreement between the experiment and simulation. We notice that the intensity of the diffraction pattern around the circumference is weaker than the experiment. This discrepancy comes from the fact that in simulation we are averaging the diffraction pattern for each wavelength inside the emission range assuming all wavelengths have identical intensity. However, in experiment, the monolayer PL emission intensity at different wavelengths is different. Interestingly, if we change the lattice into a hexagonal one, the simulated far-field emission pattern dramatically changes into a star-shape (Figure 4.4c). Such ability to tailor the far-field emission pattern could be useful for polariton light-emitting devices.

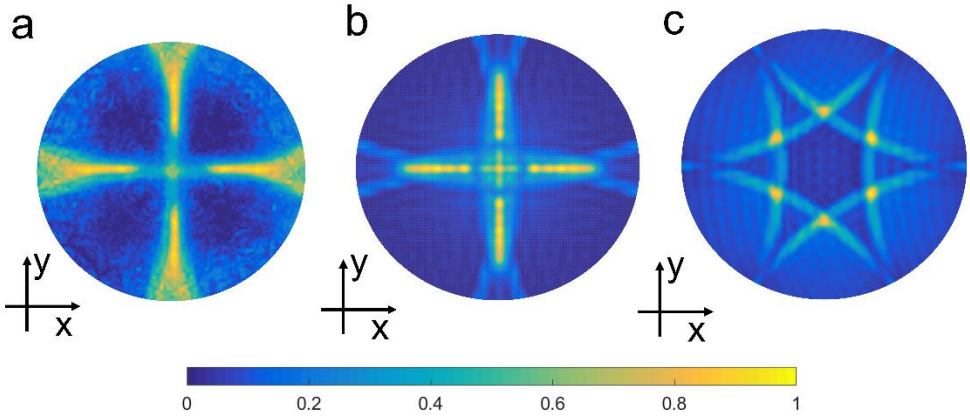

Figure 4.4. Far-field emission pattern. (a) Back focal plane (BFP) image of the far-field emission. Different from the excitonic emission of a monolayer on a unpattern substrate, the polariton emission shows a unique pattern due to the diffraction effect of the nanophotonic structures. (b) FDTD-simulated BFP image from the same metasurface structure. (c) FDTD-simulated BFP image from a hexagonal photonic lattice.

4.4 Meta-optical engineering of the exciton-polariton

A unique property of our metasurface-based EP is the ability to engineer the Rabi splitting, the polariton dispersion and the far-field emission pattern by exploiting the large number of degrees of freedom offered by the nanopatterned photonic structures. Here, we systematically study how the properties of the EP can be tailored by engineering the optical meta-atoms.

We first study the effect of the metasurface thickness to the light-matter interaction strength. Different from the traditional DBR-sandwiched monolayer platform, the WSe_2 is evanescently coupled with the metasurface. The light-matter coupling strength (g) is proportional to the electrical field at the surface of the meta-atoms. This effect could be quantified by normalizing the electrical field on each meta-atom to its vacuum energy as [185,186]:

$$\int_{meta-atom} \varepsilon \, \psi^2 dV = \hbar\omega, \quad (4.9)$$

Here, ε is the dielectric function of the meta-atom and the ψ is the electric field. $\hbar\omega$ represents the vacuum energy of the GMR supported by the meta-atom. This equation indicates that a well-confined mode leads to a large normalized electric field amplitude. However, the surface field also suffers from a stronger exponential decay in the out-of-plane direction as the confinement becomes stronger. Here we define 'surface field' as the electric field at the surface of the meta-atom with which the WSe_2 monolayer would interact:

$$\psi_{avg} = \frac{1}{a^2} \int_{Surface} |\psi| \, dS, \quad (4.10)$$

where a is the period of the meta-atom.

As a result, there is a trade-off between the amplitude of the normalized electric field and the amount of surface field. We simulated the eigenmodes in the meta-atom with different thickness

using COMSOL Multiphysics and normalized the electric field according to the Equation 4.9, and then calculate the surface field via Equation 4.10.

The results are shown in the Figure 4.5a, the surface field amplitude slightly increases as the thickness increases from 65nm to 100nm, and then decreases with the further increase of the slab thickness. The results indicate a slab thickness ~100nm would be the optimal thickness for enhancing light-matter coupling in our platform. To further validate our result, we simulated the Rabi splitting of the WSe_2 coupled with the meta-atom with various thicknesses via RCWA simulation. The period of the meta-atom is adjusted while the thickness is changed to match the photonic resonance to the WSe_2 exciton wavelength (715nm). The trend of the Rabi splitting qualitatively matches with the trend of the normalized surface electric field (Figure 4.5a).

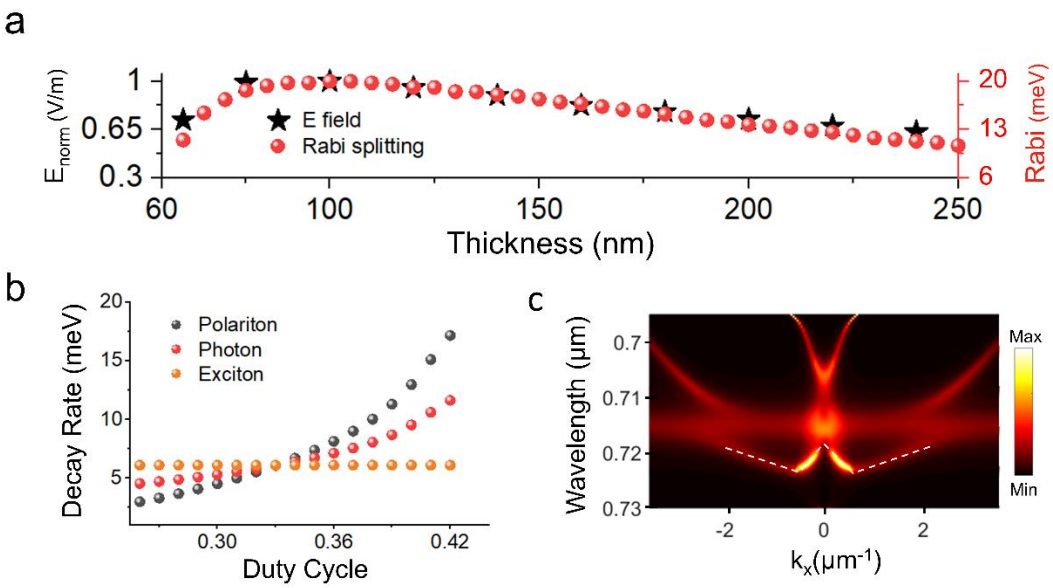

Figure 4.5. Meta-optical engineering of the exciton-polariton. (a) Slab thickness-dependent Rabi splitting and normalized E field. The results indicate a slab thickness ~100nm would be the optimal thickness for enhancing the light-matter coupling strength in our platform. (b) The effect of the duty cycle of the hole in the meta-atom to the polariton decay rate. A small duty ratio would

effectively suppress the polariton decay rate into the free space. (c) A unique W-shape polariton dispersion in our platform (The white dash line).

We then explored the effect of the duty cycles of the hole (defined as the ratio of the hole diameter to the lattice periodicity) to the polariton decay rate. We simulated the photon decay rate as a function of the duty cycle with a fixed period and found the decay rate increases when the hole size becomes larger (Figure 4.5b). Using the photon decay and experimentally extracted exciton decay rate, we calculate he polariton decay rate and find that the decay rate is suppressed with a small duty cycle. More advanced subwavelength engineering of the meta-atom could further dramatically suppress the polariton decay [187].

We then analyzed the effect of the polarization and the periodicity in the EP system. Different from 1D photonic lattice, the s and p polarizations are degenerate at normal incident ($k_x = 0$) due to the intrinsic symmetry of our metasurface. This degeneracy is lifted with gradually increasing k value. Such degeneracy would allow the study of valley-polariton [142]. A rich cluster of dispersion behavior, including linear, parabolic and W-shape dispersion, is supported in the momentum-space of the EP system. The various slopes of dispersion favor future study of our EP platform both in the high and slow group-velocity regime, with application in ballistic propagation of polaritons [188] and Bose−Einstein condensation[61]. Figure 4.5c showed the simulated absorption spectrum of another WSe2-metasurface structure (thickness of 130 nm, period of 463 nm, duty ratio of 0.5) where the coherent coupling of the exciton to a ‘W-shaped’ dispersion is observed (the white dash line), with applications in the future study of momentum-space Josephson effect[62] and micro-optical parametric oscillation[63].

In conclusion, we demonstrated EPs in atomically thin WSe_2 strongly coupled to the GMR in a SiN metasurface. The strong coupling regime is probed via energy-momentum spectroscopy on the WSe_2-metasurface sample, and a coherent light-matter interaction strength of ~18meV is measured. Finally, we showed that the Rabi splitting, the polariton dispersion and the far-field emission pattern could be tailored by subwavelength-scale engineering of the meta-atoms in the metasurface. Our platform opens the door for the future development of novel EP devices by advanced meta-optical engineering.

Chapter 5 Conclusion and future direction

In conclusion, we study the light-matter interaction on the hybrid SiN photonics platform with two emerging materials: colloidal QDs and monolayer TMD. We couple the quantum-confined excitons in these materials with integrated SiN photonic cavities to enhance the light-matter interaction, for future applications in cavity-enhanced light sources [189], ultra-low power nonlinear optics [23], and quantum many-body simulations with interacting photons [80]. For colloidal QDs, we demonstrate a deterministic positioning mechanism on SiN photonic crystal nanobeam cavity and observe the Purcell enhancement and saturable photoluminescence. For monolayer TMD, we demonstrate the strong coupling between the excitons with a SiN metasurface. A Rabi splitting of 18 meV is observed which matched well the numerical simulation. Apart from the light-matter interaction, we also explore tunable SiN integrated cavities and demonstrate the large thermal tuning of a polymer embedded SiN nanobeam cavity, together with the active tuning of a heterogenous photonic molecule.

Following are some of the future directions inspired by this thesis:

- Deterministic Positioning of a Single Quantum Dot: In Chapter 2, we deterministically positioned an ensemble of QDs on the SiN cavities. To further explore the quantum-emitter nature of the colloidal QDs, the deterministic positioning of a few/single QD is appealing. For example, by making the windows smaller (~50 nm) and synthesizing giant QDs (~50 nm diameter) [78], the number of QDs landing inside the windows could be effectively reduced. Recently, deterministic positioning of a single colloidal QD on an integrated photonics waveguide has also been demonstrated [165]. The fabrication processes are similar to our work in Chapter 2, with an additional lift-off process to clean the residual

QDs landing outside the targeted site. This lift-off process allows for iterative polymer resist patterning, which provides a viable method to position single emitters at predefined positions in a photonic integrated circuit with a yield that approaches unity. Moving forward, more advanced deposition methods such as Langmuir−Blodgett deposition [67] could be applied to precisely control the layer number and the uniformity of a QD thin film, leading to a higher yield and better reproducibility. Novel nanophotonic design could also improve control over the coupling to QDs [191]. For example, a nano-pocket design inside the nanobeam cavity has been recently demonstrated, where a low mode volume and high coupling efficiency are simultaneously achieved. Together with the above-mentioned active tuning mechanisms of the integrated photonic devices, deterministically positioned colloidal QD systems are promising for future scalable cavity quantum electrodynamic platforms.

- Nonlinear Polaritonic Metasurface for Quantum Simulation: The idea of quantum simulation as proposed by Feynman is to simulate a complex quantum system with another quantum system that is more readily controlled. A critical need for such quantum simulation is to create a lattice of quantum nodes [192]. The interplay of nonlinear interaction between light at each node and coherent coupling between each node is at the heart of many quantum simulation methods. The above configuration could be realized by an array of coupled InGaAs/GaAs micropillars-based EPs with on-site excitonic nonlinearity [193,194]. However, InGaAs/GaAs EPs only work under cryogenic temperature due to the small exciton binding energy. The monolayer EPs discussed in Chapter 4 provide opportunities for room temperature operation. The on-site excitonic nonlinearity of DBR-based monolayer EPs has been actively studied [195,196], yet few

experiments have been performed with the metasurface-based EPs. Together with the under-explored nonlinearity, the ability to sculpt the polaritonic dispersion and polariton lifetime on the metasurface platform provides extra opportunities to study exotic physics, such as flat-bands [197] and momentum-space Josephson effects [198]. Recent demonstrations of topological polaritons in a two-dimensional metasurface platform also provide the opportunity to merge topological physics with nonlinear EPs in the future [199,200].

BIBLIOGRAPHY

1. X. Qiang, X. Zhou, J. Wang, C. M. Wilkes, T. Loke, S. O'Gara, L. Kling, G. D. Marshall, R. Santagati, T. C. Ralph, J. B. Wang, J. L. O'Brien, M. G. Thompson, and J. C. F. Matthews, "Large-scale silicon quantum photonics implementing arbitrary two-qubit processing," Nature Photonics 12, 534 (2018).
2. J. M. Arrazola, V. Bergholm, K. Brádler, T. R. Bromley, M. J. Collins, I. Dhand, A. Fumagalli, T. Gerrits, A. Goussev, L. G. Helt, J. Hundal, T. Isacsson, R. B. Israel, J. Izaac, S. Jahangiri, R. Janik, N. Killoran, S. P. Kumar, J. Lavoie, A. E. Lita, D. H. Mahler, M. Menotti, B. Morrison, S. W. Nam, L. Neuhaus, H. Y. Qi, N. Quesada, A. Repingon, K. K. Sabapathy, M. Schuld, D. Su, J. Swinarton, A. Száva, K. Tan, P. Tan, V. D. Vaidya, Z. Vernon, Z. Zabaneh, and Y. Zhang, "Quantum circuits with many photons on a programmable nanophotonic chip," Nature 591, 54–60 (2021).
3. C. Rogers, A. Y. Piggott, D. J. Thomson, R. F. Wiser, I. E. Opris, S. A. Fortune, A. J. Compston, A. Gondarenko, F. Meng, X. Chen, G. T. Reed, and R. Nicolaescu, "A universal 3D imaging sensor on a silicon photonics platform," Nature 590, 256–261 (2021).
4. J. F. Bauters, M. J. R. Heck, D. John, D. Dai, M.-C. Tien, J. S. Barton, A. Leinse, R. G. Heideman, D. J. Blumenthal, and J. E. Bowers, "Ultra-low-loss high-aspect-ratio Si3N4 waveguides," Opt. Express, OE 19, 3163–3174 (2011).
5. A. Gondarenko, J. S. Levy, and M. Lipson, "High confinement micron-scale silicon nitride high Q ring resonator," Opt. Express, OE 17, 11366–11370 (2009).
6. E. S. Hosseini, S. Yegnanarayanan, A. H. Atabaki, M. Soltani, and A. Adibi, "High Quality Planar Silicon Nitride Microdisk Resonators for Integrated Photonics in the VisibleWavelength Range," Opt. Express, OE 17, 14543–14551 (2009).
7. C. V. Poulton, M. J. Byrd, M. Raval, Z. Su, N. Li, E. Timurdogan, D. Coolbaugh, D. Vermeulen, and M. R. Watts, "Large-scale silicon nitride nanophotonic phased arrays at infrared and visible wavelengths," Opt. Lett., OL 42, 21–24 (2017).
8. B. Momeni, E. S. Hosseini, and A. Adibi, "Planar photonic crystal microspectrometers in silicon-nitride for the visible range," Opt. Express, OE 17, 17060–17069 (2009).
9. C. Taballione, C. Taballione, T. A. W. Wolterink, J. Lugani, A. Eckstein, B. A. Bell, R. Grootjans, I. Visscher, D. Geskus, C. G. H. Roeloffzen, J. J. Renema, J. J. Renema, J. J. Renema, I. A. Walmsley, P. W. H. Pinkse, and K.-J. Boller, "8×8 reconfigurable quantum photonic processor based on silicon nitride waveguides," Opt. Express, OE 27, 26842–26857 (2019).
10. N. A. Tyler, D. Fowler, S. Malhouitre, S. Garcia, P. Grosse, W. Rabaud, and B. Szelag, "SiN integrated optical phased arrays for two-dimensional beam steering at a single near-infrared wavelength," Opt. Express, OE 27, 5851–5858 (2019).
11. H. Park, C. Zhang, M. A. Tran, and T. Komljenovic, "Heterogeneous silicon nitride photonics," Optica, OPTICA 7, 336–337 (2020).
12. M. Churaev, S. Honl, R. N. Wang, C. Mohl, T. Liu, J. C. Skehan, J. Riemensberger, D. Caimi, J. Liu, P. Seidler, and T. J. Kippenberg, "Hybrid Si3N4-LiNbO3 integrated platform for electro-optic conversion," in Conference on Lasers and Electro-Optics (2020), Paper STh1F.3 (Optical Society of America, 2020), p. STh1F.3.
13. Y. Shirasaki, G. J. Supran, M. G. Bawendi, and V. Bulović, "Emergence of colloidal quantum-dot light-emitting technologies," Nature Photon 7, 13–23 (2013).

14. X. Zhou, X. Hu, J. Yu, S. Liu, Z. Shu, Q. Zhang, H. Li, Y. Ma, H. Xu, and T. Zhai, "2D Layered Material-Based van der Waals Heterostructures for Optoelectronics," Advanced Functional Materials 28, 1706587 (2018).
15. J. Pu and T. Takenobu, "Monolayer Transition Metal Dichalcogenides as Light Sources," Advanced Materials 30, 1707627 (2018).
16. J. S. Ross, P. Klement, A. M. Jones, N. J. Ghimire, J. Yan, D. G. Mandrus, T. Taniguchi, K. Watanabe, K. Kitamura, W. Yao, D. H. Cobden, and X. Xu, "Electrically tunable excitonic light-emitting diodes based on monolayer WSe 2 p–n junctions," Nature Nanotech 9, 268–272 (2014).
17. S. Wu, S. Buckley, J. R. Schaibley, L. Feng, J. Yan, D. G. Mandrus, F. Hatami, W. Yao, J. Vučković, A. Majumdar, and X. Xu, "Monolayer semiconductor nanocavity lasers with ultralow thresholds," Nature 520, 69–72 (2015).
18. Y.-M. He, G. Clark, J. R. Schaibley, Y. He, M.-C. Chen, Y.-J. Wei, X. Ding, Q. Zhang, W. Yao, X. Xu, C.-Y. Lu, and J.-W. Pan, "Single quantum emitters in monolayer semiconductors," Nature Nanotechnology 10, 497–502 (2015).
19. W. Xie, T. Stöferle, G. Rainò, T. Aubert, S. Bisschop, Y. Zhu, R. F. Mahrt, P. Geiregat, E. Brainis, Z. Hens, and D. V. Thourhout, "On-Chip Integrated Quantum-Dot–Silicon-Nitride Microdisk Lasers," Advanced Materials 29, 1604866 (2017).
20. K. J. Vahala, "Optical microcavities," Nature 424, 839–846 (2003).
21. M. Lončar, T. Yoshie, A. Scherer, P. Gogna, and Y. Qiu, "Low-threshold photonic crystal laser," Appl. Phys. Lett. 81, 2680–2682 (2002).
22. M. Li, J. Ling, Y. He, U. A. Javid, S. Xue, and Q. Lin, "Lithium niobate photonic-crystal electro-optic modulator," Nat Commun 11, 4123 (2020).
23. S. Sun, H. Kim, Z. Luo, G. S. Solomon, and E. Waks, "A single-photon switch and transistor enabled by a solid-state quantum memory," Science 361, 57–60 (2018).
24. X. Lin, X. Dai, C. Pu, Y. Deng, Y. Niu, L. Tong, W. Fang, Y. Jin, and X. Peng, "Electrically-driven single-photon sources based on colloidal quantum dots with near-optimal antibunching at room temperature," Nature Communications 8, 1132 (2017).
25. T. Huang, P. Han, X. Wang, S. Feng, W. Sun, J. Ye, and Y. Zhang, "Phonon induced pure dephasing process of excitonic state in colloidal semiconductor quantum dots," Superlattices and Microstructures 92, 52–59 (2016).
26. A. V. Kuhlmann, J. Houel, A. Ludwig, L. Greuter, D. Reuter, A. D. Wieck, M. Poggio, and R. J. Warburton, "Charge noise and spin noise in a semiconductor quantum device," Nature Physics 9, 570–575 (2013).
27. F. W. Sun and C. W. Wong, "Indistinguishability of independent single photons," Physical Review A - Atomic, Molecular, and Optical Physics 79, 013824 (2009).
28. H. Utzat, W. Sun, A. E. K. Kaplan, F. Krieg, M. Ginterseder, B. Spokoyny, N. D. Klein, K. E. Shulenberger, C. F. Perkinson, M. V. Kovalenko, and M. G. Bawendi, "Coherent single-photon emission from colloidal lead halide perovskite quantum dots," Science 363, 1068–1072 (2019).
29. M. O. Scully, M. S. Zubairy, and I. A. Walmsley, " Quantum Optics ," American Journal of Physics 67, 648–648 (1999).
30. B. Guzelturk, Y. Kelestemur, K. Gungor, A. Yeltik, M. Z. Akgul, Y. Wang, R. Chen, C. Dang, H. Sun, and H. V. Demir, "Stable and Low-Threshold Optical Gain in CdSe/CdS Quantum Dots: An All-Colloidal Frequency Up-Converted Laser," Advanced Materials 27, 2741–2746 (n.d.).

31. Y. Chen, A. Ryou, M. R. Friedfeld, T. Fryett, J. Whitehead, B. M. Cossairt, and A. Majumdar, "Deterministic Positioning of Colloidal Quantum Dots on Silicon Nitride Nanobeam Cavities," Nano Lett. 18, 6404–6410 (2018).
32. C.-H. Liu, G. Clark, T. Fryett, S. Wu, J. Zheng, F. Hatami, X. Xu, and A. Majumdar, "Nanocavity Integrated van der Waals Heterostructure Light-Emitting Tunneling Diode," Nano Lett. 17, 200–205 (2017).
33. X. Liu, T. Galfsky, Z. Sun, F. Xia, E. Lin, Y.-H. Lee, S. Kéna-Cohen, and V. M. Menon, "Strong light–matter coupling in two-dimensional atomic crystals," Nature Photonics 9, 30–34 (2015).
34. G. Wang, A. Chernikov, M. M. Glazov, T. F. Heinz, X. Marie, T. Amand, and B. Urbaszek, "Colloquium: Excitons in atomically thin transition metal dichalcogenides," Rev. Mod. Phys. 90, 021001 (2018).
35. Q. Quan, P. B. Deotare, and M. Loncar, "Photonic crystal nanobeam cavity strongly coupled to the feeding waveguide," Appl. Phys. Lett. 96, 203102 (2010).
36. S. Fan and J. D. Joannopoulos, "Analysis of guided resonances in photonic crystal slabs," Phys. Rev. B 65, 235112 (2002).
37. Y. Chen, S. Miao, T. Wang, D. Zhong, A. Saxena, C. Chow, J. Whitehead, D. Gerace, X. Xu, S.-F. Shi, and A. Majumdar, "Metasurface Integrated Monolayer Exciton Polariton," Nano Lett. 20, 5292–5300 (2020).
38. B. Ellis, M. A. Mayer, G. Shambat, T. Sarmiento, J. Harris, E. E. Haller, and J. Vučković, "Ultralow-threshold electrically pumped quantum-dot photonic-crystal nanocavity laser," Nature Photonics 5, 297–300 (2011).
39. D. Dai, A. Fang, and J. E. Bowers, "Hybrid silicon lasers for optical interconnects," New J. Phys. 11, 125016 (2009).
40. Y. Li, J. Zhang, D. Huang, H. Sun, F. Fan, J. Feng, Z. Wang, and C. Z. Ning, "Room-temperature continuous-wave lasing from monolayer molybdenum ditelluride integrated with a silicon nanobeam cavity," Nature Nanotechnology 12, 987–992 (2017).
41. S. T. Jagsch, N. V. Triviño, F. Lohof, G. Callsen, S. Kalinowski, I. M. Rousseau, R. Barzel, J.-F. Carlin, F. Jahnke, R. Butté, C. Gies, A. Hoffmann, N. Grandjean, and S. Reitzenstein, "A quantum optical study of thresholdless lasing features in high- β nitride nanobeam cavities," Nature Communications 9, 564 (2018).
42. S. Buckley, K. Rivoire, and J. Vučković, "Engineered quantum dot single-photon sources," Rep. Prog. Phys. 75, 126503 (2012).
43. D. Englund, A. Majumdar, A. Faraon, M. Toishi, N. Stoltz, P. Petroff, and J. Vučković, "Resonant Excitation of a Quantum Dot Strongly Coupled to a Photonic Crystal Nanocavity," Phys. Rev. Lett. 104, 073904 (2010).
44. A. Reinhard, T. Volz, M. Winger, A. Badolato, K. J. Hennessy, E. L. Hu, and A. Imamoğlu, "Strongly correlated photons on a chip," Nature Photonics 6, 93–96 (2012).
45. D. Liang, X. Huang, G. Kurczveil, M. Fiorentino, and R. G. Beausoleil, "Integrated finely tunable microring laser on silicon," Nature Photonics 10, 719–722 (2016).
46. M. J. R. Heck, J. F. Bauters, M. L. Davenport, J. K. Doylend, S. Jain, G. Kurczveil, S. Srinivasan, Y. Tang, and J. E. Bowers, "Hybrid Silicon Photonic Integrated Circuit Technology," IEEE Journal of Selected Topics in Quantum Electronics 19, 6100117–6100117 (2013).
47. I. M. Georgescu, S. Ashhab, and F. Nori, "Quantum simulation," Rev. Mod. Phys. 86, 153–185 (2014).

48. A. Aspuru-Guzik and P. Walther, "Photonic quantum simulators," Nature Physics 8, 285–291 (2012).
49. C. Schneider, M. Strauß, T. Sünner, A. Huggenberger, D. Wiener, S. Reitzenstein, M. Kamp, S. Höfling, and A. Forchel, "Lithographic alignment to site-controlled quantum dots for device integration," Appl. Phys. Lett. 92, 183101 (2008).
50. G. Wei, D. A. Czaplewski, E. J. Lenferink, T. K. Stanev, I. W. Jung, and N. P. Stern, "Size-tunable Lateral Confinement in Monolayer Semiconductors," Scientific Reports 7, 3324 (2017).
51. A. Ryou, D. Rosser, A. Saxena, T. Fryett, and A. Majumdar, "Strong photon antibunching in weakly nonlinear two-dimensional exciton-polaritons," Phys. Rev. B 97, 235307 (2018).
52. C. Palacios-Berraquero, D. M. Kara, A. R.-P. Montblanch, M. Barbone, P. Latawiec, D. Yoon, A. K. Ott, M. Loncar, A. C. Ferrari, and M. Atatüre, "Large-scale quantum-emitter arrays in atomically thin semiconductors," Nature Communications 8, 15093 (2017).
53. A. P. Alivisatos, "Semiconductor Clusters, Nanocrystals, and Quantum Dots," Science 271, 933–937 (1996).
54. L. Qu and X. Peng, "Control of Photoluminescence Properties of CdSe Nanocrystals in Growth," J. Am. Chem. Soc. 124, 2049–2055 (2002).
55. P. O. Anikeeva, J. E. Halpert, M. G. Bawendi, and V. Bulović, "Quantum Dot Light-Emitting Devices with Electroluminescence Tunable over the Entire Visible Spectrum," Nano Lett. 9, 2532–2536 (2009).
56. V. Chandrasekaran, M. D. Tessier, D. Dupont, P. Geiregat, Z. Hens, and E. Brainis, "Nearly Blinking-Free, High-Purity Single-Photon Emission by Colloidal InP/ZnSe Quantum Dots," Nano Lett. 17, 6104–6109 (2017).
57. B. le Feber, F. Prins, E. De Leo, F. T. Rabouw, and D. J. Norris, "Colloidal-Quantum-Dot Ring Lasers with Active Color Control," Nano Lett. 18, 1028–1034 (2018).
58. W. Xie, T. Stöferle, G. Rainò, T. Aubert, S. Bisschop, Y. Zhu, R. F. Mahrt, P. Geiregat, E. Brainis, Z. Hens, and D. V. Thourhout, "On-Chip Integrated Quantum-Dot–Silicon-Nitride Microdisk Lasers," Advanced Materials 29, 1604866 (2017).
59. W. Xie, Y. Zhu, S. Bisschop, T. Aubert, Z. Hens, D. van Thourhout, and P. Geiregat, "Colloidal Quantum Dots Enabling Coherent Light Sources for Integrated Silicon-Nitride Photonics," IEEE Journal of Selected Topics in Quantum Electronics 23, 1–13 (2017).
60. W. Xie, Y. Zhu, T. Aubert, Z. Hens, E. Brainis, and D. V. Thourhout, "Fabrication and characterization of on-chip silicon nitride microdisk integrated with colloidal quantum dots," Opt. Express, OE 24, A114–A122 (2016).
61. F. Fan, O. Voznyy, R. P. Sabatini, K. T. Bicanic, M. M. Adachi, J. R. McBride, K. R. Reid, Y.-S. Park, X. Li, A. Jain, R. Quintero-Bermudez, M. Saravanapavanantham, M. Liu, M. Korkusinski, P. Hawrylak, V. I. Klimov, S. J. Rosenthal, S. Hoogland, and E. H. Sargent, "Continuous-wave lasing in colloidal quantum dot solids enabled by facet-selective epitaxy," Nature 544, 75–79 (2017).
62. X. Lin, X. Dai, C. Pu, Y. Deng, Y. Niu, L. Tong, W. Fang, Y. Jin, and X. Peng, "Electrically-driven single-photon sources based on colloidal quantum dots with near-optimal antibunching at room temperature," Nature Communications 8, 1132 (2017).
63. S. Gupta and E. Waks, "Spontaneous emission enhancement and saturable absorption of colloidal quantum dots coupled to photonic crystal cavity," Opt. Express, OE 21, 29612–29619 (2013).

64. A. Faraon, I. Fushman, D. Englund, N. Stoltz, P. Petroff, and J. Vučković, "Coherent generation of non-classical light on a chip via photon-induced tunnelling and blockade," Nature Physics 4, 859–863 (2008).
65. Z. Yang, M. Pelton, I. Fedin, D. V. Talapin, and E. Waks, "A room temperature continuous-wave nanolaser using colloidal quantum wells," Nature Communications 8, 143 (2017).
66. V. R. Manfrinato, D. D. Wanger, D. B. Strasfeld, H.-S. Han, F. Marsili, J. P. Arrieta, T. S. Mentzel, M. G. Bawendi, and K. K. Berggren, "Controlled placement of colloidal quantum dots in sub-15 nm clusters," Nanotechnology 24, 125302 (2013).
67. W. Xie, R. Gomes, T. Aubert, S. Bisschop, Y. Zhu, Z. Hens, E. Brainis, and D. Van Thourhout, "Nanoscale and Single-Dot Patterning of Colloidal Quantum Dots," Nano Lett. 15, 7481–7487 (2015).
68. M. Khan, T. Babinec, M. W. McCutcheon, P. Deotare, and M. Lončar, "Fabrication and characterization of high-quality-factor silicon nitride nanobeam cavities," Opt. Lett., OL 36, 421–423 (2011).
69. W. H. P. Pernice, C. Xiong, C. Schuck, and H. X. Tang, "High-Q aluminum nitride photonic crystal nanobeam cavities," Appl. Phys. Lett. 100, 091105 (2012).
70. T. K. Fryett, Y. Chen, J. Whitehead, Z. M. Peycke, X. Xu, and A. Majumdar, "Encapsulated Silicon Nitride Nanobeam Cavity for Hybrid Nanophotonics," ACS Photonics (2018).
71. R. Bose, D. Sridharan, G. S. Solomon, and E. Waks, "Observation of strong coupling through transmission modification of a cavity-coupled photonic crystal waveguide," Opt. Express, OE 19, 5398–5409 (2011).
72. V. Prasad, D. Semwogerere, and E. R. Weeks, "Confocal microscopy of colloids," J. Phys.: Condens. Matter 19, 113102 (2007).
73. A. F. van Driel, I. S. Nikolaev, P. Vergeer, P. Lodahl, D. Vanmaekelbergh, and W. L. Vos, "Statistical analysis of time-resolved emission from ensembles of semiconductor quantum dots: Interpretation of exponential decay models," Phys. Rev. B 75, 035329 (2007).
74. M. O. Scully and M. S. Zubairy, "Quantum Optics by Marlan O. Scully," /core/books/quantum-optics/08DC53888452CBC6CDC0FD8A1A1A4DD7.
75. J. D. Ryckman and S. M. Weiss, "Low mode volume slotted photonic crystal single nanobeam cavity," Appl. Phys. Lett. 101, 071104 (2012).
76. H. Choi, M. Heuck, and D. Englund, "Self-Similar Nanocavity Design with Ultrasmall Mode Volume for Single-Photon Nonlinearities," Phys. Rev. Lett. 118, 223605 (2017).
77. Y. Chen, J. Vela, H. Htoon, J. L. Casson, D. J. Werder, D. A. Bussian, V. I. Klimov, and J. A. Hollingsworth, "“Giant” Multishell CdSe Nanocrystal Quantum Dots with Suppressed Blinking," J. Am. Chem. Soc. 130, 5026–5027 (2008).
78. J. Kundu, Y. Ghosh, A. M. Dennis, H. Htoon, and J. A. Hollingsworth, "Giant Nanocrystal Quantum Dots: Stable Down-Conversion Phosphors that Exploit a Large Stokes Shift and Efficient Shell-to-Core Energy Relaxation," Nano Lett. 12, 3031–3037 (2012).
79. I. Carusotto and C. Ciuti, "Quantum fluids of light," Rev. Mod. Phys. 85, 299–366 (2013).
80. A. Majumdar, A. Rundquist, M. Bajcsy, and J. Vučković, "Cavity quantum electrodynamics with a single quantum dot coupled to a photonic molecule," Phys. Rev. B 86, 045315 (2012).
81. T. Grujic, S. R. Clark, D. Jaksch, and D. G. Angelakis, "Non-equilibrium many-body effects in driven nonlinear resonator arrays," New J. Phys. 14, 103025 (2012).

82. H. Flayac and V. Savona, "Unconventional photon blockade," Phys. Rev. A 96, 053810 (2017).
83. P. B. Deotare, M. W. McCutcheon, I. W. Frank, M. Khan, and M. Lončar, "Coupled photonic crystal nanobeam cavities," Appl. Phys. Lett. 95, 031102 (2009).
84. M. Cirillo, T. Aubert, R. Gomes, R. Van Deun, P. Emplit, A. Biermann, H. Lange, C. Thomsen, E. Brainis, and Z. Hens, "“Flash” Synthesis of CdSe/CdS Core–Shell Quantum Dots," Chem. Mater. 26, 1154–1160 (2014).
85. A. Nag, M. V. Kovalenko, J.-S. Lee, W. Liu, B. Spokoyny, and D. V. Talapin, "Metal-free Inorganic Ligands for Colloidal Nanocrystals: S2–, HS–, Se2–, HSe–, Te2–, HTe–, TeS32–, OH–, and NH2– as Surface Ligands," J. Am. Chem. Soc. 133, 10612–10620 (2011).
86. V. A. Vlaskin, C. J. Barrows, C. S. Erickson, and D. R. Gamelin, "Nanocrystal Diffusion Doping," J. Am. Chem. Soc. 135, 14380–14389 (2013).
87. M. A. Green, A. Ho-Baillie, and H. J. Snaith, "The emergence of perovskite solar cells," Nature Photonics 8, 506–514 (2014).
88. B. R. Sutherland and E. H. Sargent, "Perovskite photonic sources," Nature Photonics 10, 295–302 (2016).
89. R. E. Brandt, V. Stevanović, D. S. Ginley, and T. Buonassisi, "Identifying defect-tolerant semiconductors with high minority-carrier lifetimes: beyond hybrid lead halide perovskites," MRS Communications 5, 265–275 (2015).
90. G. Xing, N. Mathews, S. S. Lim, N. Yantara, X. Liu, D. Sabba, M. Grätzel, S. Mhaisalkar, and T. C. Sum, "Low-temperature solution-processed wavelength-tunable perovskites for lasing," Nature Materials 13, 476–480 (2014).
91. Y. Wang, X. Li, J. Song, L. Xiao, H. Zeng, and H. Sun, "All-Inorganic Colloidal Perovskite Quantum Dots: A New Class of Lasing Materials with Favorable Characteristics," Advanced Materials 27, 7101–7108 (2015).
92. K. Wang, S. Wang, S. Xiao, and Q. Song, "Recent Advances in Perovskite Micro- and Nanolasers," Advanced Optical Materials 6, 1800278 (2018).
93. "Nanocrystals of Cesium Lead Halide Perovskites (CsPbX3, X = Cl, Br, and I): Novel Optoelectronic Materials Showing Bright Emission with Wide Color Gamut | Nano Letters," https://pubs.acs.org/doi/10.1021/nl5048779.
94. M. A. Becker, R. Vaxenburg, G. Nedelcu, P. C. Sercel, A. Shabaev, M. J. Mehl, J. G. Michopoulos, S. G. Lambrakos, N. Bernstein, J. L. Lyons, T. Stöferle, R. F. Mahrt, M. V. Kovalenko, D. J. Norris, G. Rainò, and A. L. Efros, "Bright triplet excitons in caesium lead halide perovskites," Nature 553, 189–193 (2018).
95. M. P. van Exter, G. Nienhuis, and J. P. Woerdman, "Two simple expressions for the spontaneous emission factor B," Phys. Rev. B 54, 6 (1996).
96. Z. Zhang and N. Keil, "Thermo-optic devices on polymer platform," Optics Communications 362, 101–114 (2016).
97. Y. Zhang and Y. Shi, "Temperature insensitive lower-index-mode photonic crystal nanobeam cavity," Opt. Lett., OL 40, 264–267 (2015).
98. Y. Zhang, P. Liu, S. Zhang, W. Liu, J. Chen, and Y. Shi, "High sensitivity temperature sensor based on cascaded silicon photonic crystal nanobeam cavities," Opt. Express, OE 24, 23037–23043 (2016).

99. M. T. Do, T. T. N. Nguyen, Q. Li, H. Benisty, I. Ledoux-Rak, and N. D. Lai, "Submicrometer 3D structures fabrication enabled by one-photon absorption direct laser writing," Opt. Express, OE 21, 20964–20973 (2013).
100. Z. Zhang, D. Liu, D. de Felipe, A. Liu, N. Keil, and N. Grote, "Polymer embedded silicon nitride thermally tunable Bragg grating filters," Appl. Phys. Lett. 102, 181105 (2013).
101. R. Miura, S. Imamura, R. Ohta, A. Ishii, X. Liu, T. Shimada, S. Iwamoto, Y. Arakawa, and Y. K. Kato, "Ultralow mode-volume photonic crystal nanobeam cavities for high-efficiency coupling to individual carbon nanotube emitters," Nature Communications 5, 5580 (2014).
102. Q. Quan and M. Loncar, "Deterministic design of wavelength scale, ultra-high Q photonic crystal nanobeam cavities," Opt. Express, OE 19, 18529–18542 (2011).
103. D. Yang, H. Tian, and Y. Ji, "High-Q and high-sensitivity width-modulated photonic crystal single nanobeam air-mode cavity for refractive index sensing," Appl. Opt., AO 54, 1–5 (2015).
104. B.-H. Ahn, J.-H. Kang, M.-K. Kim, J.-H. Song, B. Min, K.-S. Kim, and Y.-H. Lee, "One-dimensional parabolic-beam photonic crystal laser," Opt. Express, OE 18, 5654–5660 (2010).
105. S. G. Johnson and J. D. Joannopoulos, "Block-iterative frequency-domain methods for Maxwell's equations in a planewave basis," Opt. Express, OE 8, 173–190 (2001).
106. A. Gondarenko, J. S. Levy, and M. Lipson, "High confinement micron-scale silicon nitride high Q ring resonator," Opt. Express, OE 17, 11366–11370 (2009).
107. E. S. Hosseini, S. Yegnanarayanan, A. H. Atabaki, M. Soltani, and A. Adibi, "High Quality Planar Silicon Nitride Microdisk Resonators for Integrated Photonics in the VisibleWavelength Range," Opt. Express, OE 17, 14543–14551 (2009).
108. A. Arbabi and L. L. Goddard, "Measurements of the refractive indices and thermo-optic coefficients of Si3N4 and SiOx using microring resonances," Opt. Lett., OL 38, 3878–3881 (2013).
109. H. Lin, Y. Song, Y. Huang, D. Kita, S. Deckoff-Jones, K. Wang, L. Li, J. Li, H. Zheng, Z. Luo, H. Wang, S. Novak, A. Yadav, C.-C. Huang, R.-J. Shiue, D. Englund, T. Gu, D. Hewak, K. Richardson, J. Kong, and J. Hu, "Chalcogenide glass-on-graphene photonics," Nature Photonics 11, 798 (2017).
110. G. Coppola, L. Sirleto, I. Rendina, and M. Iodice, "Advance in thermo-optical switches: principles, materials, design, and device structure," OE 50, 071112 (2011).
111. X. Xue, Y. Xuan, C. Wang, P.-H. Wang, Y. Liu, B. Niu, D. E. Leaird, M. Qi, and A. M. Weiner, "Thermal tuning of Kerr frequency combs in silicon nitride microring resonators," Opt. Express, OE 24, 687–698 (2016).
112. "[1805.11663] A Reconfigurable Nanophotonics Platform for Sub-Millisecond, Deep Brain Neural Stimulation," https://arxiv.org/abs/1805.11663.
113. A. Nakagawa, S. Ishii, and T. Baba, "Photonic molecule laser composed of GaInAsP microdisks," Appl. Phys. Lett. 86, 041112 (2005).
114. X. Jiang, Q. Lin, J. Rosenberg, K. Vahala, and O. Painter, "High-Q double-disk microcavities for cavity optomechanics," Opt. Express, OE 17, 20911–20919 (2009).
115. T. C. H. Liew and V. Savona, "Single Photons from Coupled Quantum Modes," Phys. Rev. Lett. 104, 183601 (2010).
116. A. Majumdar, A. Rundquist, M. Bajcsy, V. D. Dasika, S. R. Bank, and J. Vučković, "Design and analysis of photonic crystal coupled cavity arrays for quantum simulation," Phys. Rev. B 86, 195312 (2012).

117. S. V. Boriskina, "Spectrally engineered photonic molecules as optical sensors with enhanced sensitivity: a proposal and numerical analysis," J. Opt. Soc. Am. B, JOSAB 23, 1565–1573 (2006).
118. M. Zhang, C. Wang, Y. Hu, A. Shams-Ansari, T. Ren, S. Fan, and M. Lončar, "Electronically programmable photonic molecule," Nature Photon 13, 36–40 (2019).
119. B. Peng, Ş. K. Özdemir, F. Lei, F. Monifi, M. Gianfreda, G. L. Long, S. Fan, F. Nori, C. M. Bender, and L. Yang, "Parity–time-symmetric whispering-gallery microcavities," Nature Phys 10, 394–398 (2014).
120. A. Saxena, Y. Chen, A. Ryou, C. G. Sevilla, P. Xu, and A. Majumdar, "Improving Indistinguishability of Single Photons from Colloidal Quantum Dots Using Nanocavities," ACS Photonics 6, 3166–3173 (2019).
121. R. J. Glauber and M. Lewenstein, "Quantum optics of dielectric media," Phys. Rev. A 43, 467–491 (1991).
122. B. J. Dalton, E. S. Guerra, and P. L. Knight, "Field quantization in dielectric media and the generalized multipolar Hamiltonian," Phys. Rev. A 54, 2292–2313 (1996).
123. K. C. Smith, Y. Chen, A. Majumdar, and D. J. Masiello, "Active Tuning of Hybridized Modes in a Heterogeneous Photonic Molecule," Phys. Rev. Applied 13, 044041 (2020).
124. S. G. Johnson, M. Ibanescu, M. A. Skorobogatiy, O. Weisberg, J. D. Joannopoulos, and Y. Fink, "Perturbation theory for Maxwell's equations with shifting material boundaries," Phys. Rev. E 65, 066611 (2002).
125. G. Fisicaro, L. Genovese, O. Andreussi, N. Marzari, and S. Goedecker, "A generalized Poisson and Poisson-Boltzmann solver for electrostatic environments," J. Chem. Phys. 144, 014103 (2016).
126. Q. Li, T. Wang, Y. Su, M. Yan, and M. Qiu, "Coupled mode theory analysis of mode-splitting in coupled cavity system," Opt. Express, OE 18, 8367–8382 (2010).
127. M. A. Popović, C. Manolatou, and M. R. Watts, "Coupling-induced resonance frequency shifts in coupled dielectric multi-cavity filters," Opt. Express, OE 14, 1208–1222 (2006).
128. A. Yariv, Y. Xu, R. K. Lee, and A. Scherer, "Coupled-resonator optical waveguide:?a proposal and analysis," Opt. Lett., OL 24, 711–713 (1999).
129. M. Bayindir, B. Temelkuran, and E. Ozbay, "Tight-Binding Description of the Coupled Defect Modes in Three-Dimensional Photonic Crystals," Phys. Rev. Lett. 84, 2140–2143 (2000).
130. M. J. Collett and C. W. Gardiner, "Squeezing of intracavity and traveling-wave light fields produced in parametric amplification," Phys. Rev. A 30, 1386–1391 (1984).
131. H. A. Haus, Waves and Fields in Optoelectronics (Prentice-Hall, 1984).
132. S. Manzeli, D. Ovchinnikov, D. Pasquier, O. V. Yazyev, and A. Kis, "2D transition metal dichalcogenides," Nature Reviews Materials 2, 1–15 (2017).
133. Y. Ye, Z. J. Wong, X. Lu, X. Ni, H. Zhu, X. Chen, Y. Wang, and X. Zhang, "Monolayer excitonic laser," Nature Photonics 9, 733–737 (2015).
134. X. Ge, M. Minkov, S. Fan, X. Li, and W. Zhou, "Laterally confined photonic crystal surface emitting laser incorporating monolayer tungsten disulfide," npj 2D Materials and Applications 3, 1–5 (2019).
135. S. Dufferwiel, S. Schwarz, F. Withers, A. a. P. Trichet, F. Li, M. Sich, O. Del Pozo-Zamudio, C. Clark, A. Nalitov, D. D. Solnyshkov, G. Malpuech, K. S. Novoselov, J. M. Smith, M. S. Skolnick, D. N. Krizhanovskii, and A. I. Tartakovskii, "Exciton–polaritons in

van der Waals heterostructures embedded in tunable microcavities," Nature Communications 6, 1–7 (2015).
136. L. C. Flatten, Z. He, D. M. Coles, A. a. P. Trichet, A. W. Powell, R. A. Taylor, J. H. Warner, and J. M. Smith, "Room-temperature exciton-polaritons with two-dimensional WS 2," Scientific Reports 6, 1–7 (2016).
137. H. Deng, H. Haug, and Y. Yamamoto, "Exciton-polariton Bose-Einstein condensation," Rev. Mod. Phys. 82, 1489–1537 (2010).
138. "[1912.12544] Enhanced nonlinear interaction of polaritons via excitonic Rydberg states in monolayer WSe2," https://arxiv.org/abs/1912.12544.
139. S. Kim, B. Zhang, Z. Wang, J. Fischer, S. Brodbeck, M. Kamp, C. Schneider, S. Höfling, and H. Deng, "Coherent Polariton Laser," Phys. Rev. X 6, 011026 (2016).
140. Z. Sun, J. Gu, A. Ghazaryan, Z. Shotan, C. R. Considine, M. Dollar, B. Chakraborty, X. Liu, P. Ghaemi, S. Kéna-Cohen, and V. M. Menon, "Optical control of room-temperature valley polaritons," Nature Photonics 11, 491–496 (2017).
141. N. Lundt, Ł. Dusanowski, E. Sedov, P. Stepanov, M. M. Glazov, S. Klembt, M. Klaas, J. Beierlein, Y. Qin, S. Tongay, M. Richard, A. V. Kavokin, S. Höfling, and C. Schneider, "Optical valley Hall effect for highly valley-coherent exciton-polaritons in an atomically thin semiconductor," Nature Nanotechnology 14, 770–775 (2019).
142. Y.-J. Chen, J. D. Cain, T. K. Stanev, V. P. Dravid, and N. P. Stern, "Valley-polarized exciton–polaritons in a monolayer semiconductor," Nature Photonics 11, 431–435 (2017).
143. S. Dufferwiel, T. P. Lyons, D. D. Solnyshkov, A. a. P. Trichet, F. Withers, S. Schwarz, G. Malpuech, J. M. Smith, K. S. Novoselov, M. S. Skolnick, D. N. Krizhanovskii, and A. I. Tartakovskii, "Valley-addressable polaritons in atomically thin semiconductors," Nature Photonics 11, 497–501 (2017).
144. D. Sercombe, S. Schwarz, O. D. Pozo-Zamudio, F. Liu, B. J. Robinson, E. A. Chekhovich, I. I. Tartakovskii, O. Kolosov, and A. I. Tartakovskii, "Optical investigation of the natural electron doping in thin MoS 2 films deposited on dielectric substrates," Scientific Reports 3, 1–6 (2013).
145. M. Sidler, P. Back, O. Cotlet, A. Srivastava, T. Fink, M. Kroner, E. Demler, and A. Imamoglu, "Fermi polaron-polaritons in charge-tunable atomically thin semiconductors," Nature Physics 13, 255–261 (2017).
146. F. Barachati, A. Fieramosca, S. Hafezian, J. Gu, B. Chakraborty, D. Ballarini, L. Martinu, V. Menon, D. Sanvitto, and S. Kéna-Cohen, "Interacting polariton fluids in a monolayer of tungsten disulfide," Nature Nanotechnology 13, 906–909 (2018).
147. B. Lee, W. Liu, C. H. Naylor, J. Park, S. C. Malek, J. S. Berger, A. T. C. Johnson, and R. Agarwal, "Electrical Tuning of Exciton–Plasmon Polariton Coupling in Monolayer MoS2 Integrated with Plasmonic Nanoantenna Lattice," Nano Lett. 17, 4541–4547 (2017).
148. W. Liu, B. Lee, C. H. Naylor, H.-S. Ee, J. Park, A. T. C. Johnson, and R. Agarwal, "Strong Exciton–Plasmon Coupling in MoS2 Coupled with Plasmonic Lattice," Nano Lett. 16, 1262–1269 (2016).
149. S. Wang, S. Li, T. Chervy, A. Shalabney, S. Azzini, E. Orgiu, J. A. Hutchison, C. Genet, P. Samorì, and T. W. Ebbesen, "Coherent Coupling of WS2 Monolayers with Metallic Photonic Nanostructures at Room Temperature," Nano Lett. 16, 4368–4374 (2016).
150. S. M. Kamali, E. Arbabi, A. Arbabi, and A. Faraon, "A review of dielectric optical metasurfaces for wavefront control," Nanophotonics 7, 1041–1068 (2018).

151. A. Zhan, S. Colburn, C. M. Dodson, and A. Majumdar, "Metasurface Freeform Nanophotonics," Scientific Reports 7, 1–9 (2017).
152. T. Phan, D. Sell, E. W. Wang, S. Doshay, K. Edee, J. Yang, and J. A. Fan, "High-efficiency, large-area, topology-optimized metasurfaces," Light: Science & Applications 8, 1–9 (2019).
153. A. Arbabi, E. Arbabi, S. M. Kamali, Y. Horie, S. Han, and A. Faraon, "Miniature optical planar camera based on a wide-angle metasurface doublet corrected for monochromatic aberrations," Nature Communications 7, 1–9 (2016).
154. Y. Kivshar, "All-dielectric meta-optics and non-linear nanophotonics," Natl Sci Rev 5, 144–158 (2018).
155. N. H. M. Dang, D. Gerace, E. Drouard, G. Trippé-Allard, F. Lédée, R. Mazurczyk, E. Deleporte, C. Seassal, and H. S. Nguyen, "Tailoring Dispersion of Room-Temperature Exciton-Polaritons with Perovskite-Based Subwavelength Metasurfaces," Nano Lett. (2020).
156. M. Semmlinger, M. L. Tseng, J. Yang, M. Zhang, C. Zhang, W.-Y. Tsai, D. P. Tsai, P. Nordlander, and N. J. Halas, "Vacuum Ultraviolet Light-Generating Metasurface," Nano Lett. 18, 5738–5743 (2018).
157. M. Semmlinger, M. Zhang, M. L. Tseng, T.-T. Huang, J. Yang, D. P. Tsai, P. Nordlander, and N. J. Halas, "Generating Third Harmonic Vacuum Ultraviolet Light with a TiO2 Metasurface," Nano Lett. 19, 8972–8978 (2019).
158. E. Arbabi, A. Arbabi, S. M. Kamali, Y. Horie, and A. Faraon, "Controlling the sign of chromatic dispersion in diffractive optics with dielectric metasurfaces," Optica, OPTICA 4, 625–632 (2017).
159. A. Zhan, R. Gibson, J. Whitehead, E. Smith, J. R. Hendrickson, and A. Majumdar, "Controlling three-dimensional optical fields via inverse Mie scattering," Science Advances 5, eaax4769 (2019).
160. D. Sell, J. Yang, S. Doshay, R. Yang, and J. A. Fan, "Large-Angle, Multifunctional Metagratings Based on Freeform Multimode Geometries," Nano Lett. 17, 3752–3757 (2017).
161. C. H. Chu, M. L. Tseng, J. Chen, P. C. Wu, Y.-H. Chen, H.-C. Wang, T.-Y. Chen, W. T. Hsieh, H. J. Wu, G. Sun, and D. P. Tsai, "Active dielectric metasurface based on phase-change medium," Laser & Photonics Reviews 10, 986–994 (2016).
162. V. V. Zubyuk, P. P. Vabishchevich, M. R. Shcherbakov, A. S. Shorokhov, A. N. Fedotova, S. Liu, G. Keeler, T. V. Dolgova, I. Staude, I. Brener, and A. A. Fedyanin, "Low-Power Absorption Saturation in Semiconductor Metasurfaces," ACS Photonics 6, 2797–2806 (2019).
163. Q. Yuan, L. Fang, H. Fang, J. Li, T. Wang, W. Jie, J. Zhao, and X. Gan, "Second Harmonic and Sum-Frequency Generations from a Silicon Metasurface Integrated with a Two-Dimensional Material," ACS Photonics 6, 2252–2259 (2019).
164. L. Zhang, R. Gogna, W. Burg, E. Tutuc, and H. Deng, "Photonic-crystal exciton-polaritons in monolayer semiconductors," Nature Communications 9, 713 (2018).
165. V. Kravtsov, E. Khestanova, F. A. Benimetskiy, T. Ivanova, A. K. Samusev, I. S. Sinev, D. Pidgayko, A. M. Mozharov, I. S. Mukhin, M. S. Lozhkin, Y. V. Kapitonov, A. S. Brichkin, V. D. Kulakovskii, I. A. Shelykh, A. I. Tartakovskii, P. M. Walker, M. S. Skolnick, D. N. Krizhanovskii, and I. V. Iorsh, "Nonlinear polaritons in a monolayer semiconductor

coupled to optical bound states in the continuum," Light: Science & Applications 9, 1–8 (2020).
166. W. Liu, M. Hwang, Z. Ji, Y. Wang, G. Modi, and R. Agarwal, "Z2 Photonic Topological Insulators in the Visible Wavelength Range for Robust Nanoscale Photonics," Nano Lett. 20, 1329–1335 (2020).
167. B. Zhen, C. W. Hsu, L. Lu, A. D. Stone, and M. Soljačić, "Topological Nature of Optical Bound States in the Continuum," Phys. Rev. Lett. 113, 257401 (2014).
168. L.-H. Wu and X. Hu, "Scheme for Achieving a Topological Photonic Crystal by Using Dielectric Material," Phys. Rev. Lett. 114, 223901 (2015).
169. J. Jin, X. Yin, L. Ni, M. Soljačić, B. Zhen, and C. Peng, "Topologically enabled ultrahigh-Q guided resonances robust to out-of-plane scattering," Nature 574, 501–504 (2019).
170. S. Hu, M. Khater, R. Salas-Montiel, E. Kratschmer, S. Engelmann, W. M. J. Green, and S. M. Weiss, "Experimental realization of deep-subwavelength confinement in dielectric optical resonators," Science Advances 4, eaat2355 (2018).
171. S. Hu and S. M. Weiss, "Design of Photonic Crystal Cavities for Extreme Light Concentration," ACS Photonics 3, 1647–1653 (2016).
172. X. Zhang, S. Choi, D. Wang, C. H. Naylor, A. T. C. Johnson, and E. Cubukcu, "Unidirectional Doubly Enhanced MoS2 Emission via Photonic Fano Resonances," Nano Lett. 17, 6715–6720 (2017).
173. W. Huang, C. De-Eknamkul, X. Zhang, E. Leewong, M.-Q. Zhao, A. T. C. Johnson, and E. Cubukcu, "Monolayer Excitonic Emission for Imaging Spatial Dispersion of Photonic Crystals," ACS Photonics 6, 2312–2319 (2019).
174. Z. Shi, M. Khorasaninejad, Y.-W. Huang, C. Roques-Carmes, A. Y. Zhu, W. T. Chen, V. Sanjeev, Z.-W. Ding, M. Tamagnone, K. Chaudhary, R. C. Devlin, C.-W. Qiu, and F. Capasso, "Single-Layer Metasurface with Controllable Multiwavelength Functions," Nano Lett. 18, 2420–2427 (2018).
175. S. S. Wang and R. Magnusson, "Theory and applications of guided-mode resonance filters," Appl. Opt., AO 32, 2606–2613 (1993).
176. J. R. Piper and S. Fan, "Total Absorption in a Graphene Monolayer in the Optical Regime by Critical Coupling with a Photonic Crystal Guided Resonance," ACS Photonics 1, 347–353 (2014).
177. V. Liu and S. Fan, "S4 : A free electromagnetic solver for layered periodic structures," Computer Physics Communications 183, 2233–2244 (2012).
178. A. Zhan, S. Colburn, R. Trivedi, T. K. Fryett, C. M. Dodson, and A. Majumdar, "Low-Contrast Dielectric Metasurface Optics," ACS Photonics 3, 209–214 (2016).
179. D. Gerace and L. C. Andreani, "Quantum theory of exciton-photon coupling in photonic crystal slabs with embedded quantum wells," Phys. Rev. B 75, 235325 (2007).
180. L. C. Andreani and D. Gerace, "Photonic-crystal slabs with a triangular lattice of triangular holes investigated using a guided-mode expansion method," Phys. Rev. B 73, 235114 (2006).
181. D. Bajoni, D. Gerace, M. Galli, J. Bloch, R. Braive, I. Sagnes, A. Miard, A. Lemaître, M. Patrini, and L. C. Andreani, "Exciton polaritons in two-dimensional photonic crystals," Phys. Rev. B 80, 201308 (2009).
182. F. Cadiz, E. Courtade, C. Robert, G. Wang, Y. Shen, H. Cai, T. Taniguchi, K. Watanabe, H. Carrere, D. Lagarde, M. Manca, T. Amand, P. Renucci, S. Tongay, X. Marie, and B. Urbaszek, "Excitonic Linewidth Approaching the Homogeneous Limit in

${\mathrm{MoS}}_{2}$-Based van der Waals Heterostructures," Phys. Rev. X 7, 021026 (2017).
183. J. Wang, R. Su, J. Xing, D. Bao, C. Diederichs, S. Liu, T. C. H. Liew, Z. Chen, and Q. Xiong, "Room Temperature Coherently Coupled Exciton–Polaritons in Two-Dimensional Organic–Inorganic Perovskite," ACS Nano 12, 8382–8389 (2018).
184. J. A. Schuller, S. Karaveli, T. Schiros, K. He, S. Yang, I. Kymissis, J. Shan, and R. Zia, "Orientation of luminescent excitons in layered nanomaterials," Nature Nanotechnology 8, 271–276 (2013).
185. R. Gogna, L. Zhang, Z. Wang, H. Deng, and H. Deng, "Photonic crystals for controlling strong coupling in van der Waals materials," Opt. Express, OE 27, 22700–22707 (2019).
186. Z. Wang, R. Gogna, and H. Deng, "What is the best planar cavity for maximizing coherent exciton-photon coupling," Appl. Phys. Lett. 111, 061102 (2017).
187. K. L. Koshelev, S. K. Sychev, Z. F. Sadrieva, A. A. Bogdanov, and I. V. Iorsh, "Strong coupling between excitons in transition metal dichalcogenides and optical bound states in the continuum," Phys. Rev. B 98, 161113 (2018).
188. H. Franke, C. Sturm, R. Schmidt-Grund, G. Wagner, and M. Grundmann, "Ballistic propagation of exciton–polariton condensates in a ZnO-based microcavity," New J. Phys. 14, 013037 (2012).
189. F. Liu, A. J. Brash, J. O'Hara, L. M. P. P. Martins, C. L. Phillips, R. J. Coles, B. Royall, E. Clarke, C. Bentham, N. Prtljaga, I. E. Itskevich, L. R. Wilson, M. S. Skolnick, and A. M. Fox, "High Purcell factor generation of indistinguishable on-chip single photons," Nature Nanotech 13, 835–840 (2018).
190. A. Eich, T. C. Spiekermann, H. Gehring, L. Sommer, J. R. Bankwitz, P. P. J. Schrinner, J. A. Preuß, S. M. de Vasconcellos, R. Bratschitsch, W. H. P. Pernice, and C. Schuck, "Single photon emission from individual nanophotonic-integrated colloidal quantum dots," arXiv:2104.11830 [physics, physics:quant-ph] (2021).
191. J. E. Fröch, S. Kim, C. Stewart, X. Xu, Z. Du, M. Lockrey, M. Toth, and I. Aharonovich, "Photonic Nanobeam Cavities with Nanopockets for Efficient Integration of Fluorescent Nanoparticles," Nano Lett. 20, 2784–2790 (2020).
192. I. M. Georgescu, S. Ashhab, and F. Nori, "Quantum simulation," Rev. Mod. Phys. 86, 153–185 (2014).
193. T. Boulier, M. J. Jacquet, A. Maître, G. Lerario, F. Claude, S. Pigeon, Q. Glorieux, A. Amo, J. Bloch, A. Bramati, and E. Giacobino, "Microcavity Polaritons for Quantum Simulation," Advanced Quantum Technologies 3, 2000052 (2020).
194. V. Goblot, B. Rauer, F. Vicentini, A. Le Boité, E. Galopin, A. Lemaître, L. Le Gratiet, A. Harouri, I. Sagnes, S. Ravets, C. Ciuti, A. Amo, and J. Bloch, "Nonlinear Polariton Fluids in a Flatband Reveal Discrete Gap Solitons," Phys. Rev. Lett. 123, 113901 (2019).
195. J. Gu, V. Walther, L. Waldecker, D. Rhodes, A. Raja, J. C. Hone, T. F. Heinz, S. Kéna-Cohen, T. Pohl, and V. M. Menon, "Enhanced nonlinear interaction of polaritons via excitonic Rydberg states in monolayer WSe 2," Nat Commun 12, 2269 (2021).
196. R. P. A. Emmanuele, M. Sich, O. Kyriienko, V. Shahnazaryan, F. Withers, A. Catanzaro, P. M. Walker, F. A. Benimetskiy, M. S. Skolnick, A. I. Tartakovskii, I. A. Shelykh, and D. N. Krizhanovskii, "Highly nonlinear trion-polaritons in a monolayer semiconductor," Nat Commun 11, 3589 (2020).
197. Y. He, R. Mao, H. Cai, J.-X. Zhang, Y. Li, L. Yuan, S.-Y. Zhu, and D.-W. Wang, "Flat-Band Localization in Creutz Superradiance Lattices," Phys. Rev. Lett. 126, 103601 (2021).

198. N. H. M. Dang, D. Gerace, E. Drouard, G. Trippé-Allard, F. Lédeé, R. Mazurczyk, E. Deleporte, C. Seassal, and H. S. Nguyen, "Tailoring Dispersion of Room-Temperature Exciton-Polaritons with Perovskite-Based Subwavelength Metasurfaces," Nano Letters 20, 2113–2119 (2020).
199. W. Liu, Z. Ji, Y. Wang, G. Modi, M. Hwang, B. Zheng, V. J. Sorger, A. Pan, and R. Agarwal, "Generation of helical topological exciton-polaritons," Science 370, 600–604 (2020).
200. D. R. Gulevich, D. Yudin, D. V. Skryabin, I. V. Iorsh, and I. A. Shelykh, "Exploring nonlinear topological states of matter with exciton-polaritons: Edge solitons in kagome lattice," Sci Rep 7, 1780 (2017).